

DESIGN OF A PLANAR BIAXIAL MECHANICAL TESTING DEVICE FOR SOFT

BIOLOGICAL TISSUES

AN ABSTRACT

SUBMITTED ON THE FIFTEENTH DAY OF APRIL 2017

TO THE DEPARTMENT OF BIOMEDICAL ENGINEERING

IN PARTIAL FULFILLMENT OF THE REQUIREMENTS

OF THE SCHOOL OF SCIENCE AND ENGINEERING

OF TULANE UNIVERSITY

FOR THE DEGREES


OF

MASTER OF SCIENCE

AND

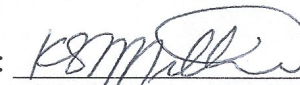
BACHELOR OF SCIENCE IN ENGINEERING

BY



TAYLOR MCCRADY

APPROVED:



KRISTIN S. MILLER, Ph.D.
DIRECTOR


CAROLYN BAYER, Ph.D.
ANNE-MARIE JOB, Ph. D.

ABSTRACT

The application of continuum mechanics principles to biological tissues is paramount to understanding (patho)physiological changes in tissue structure and function. Experimental and mathematical approaches can be utilized to quantify tissue mechanical behavior. In particular, planar biaxial mechanical testing of soft tissues (i.e. applying loads or deformation along two axes in the same plane) has proven to mimic physiologically relevant conditions for most soft tissues. Constitutive relations can then be formulated based on biaxial data to describe and predict soft tissue mechanical behavior. These mathematical tools could aid in delineating underlying mechanisms of and evaluating treatments for various clinically relevant issues. Therefore, the overall objective of this thesis is to build a custom planar biaxial mechanical testing device to characterize the mechanical properties of soft biological tissues to identify appropriate constitutive relations. A custom planar biaxial mechanical testing device was successfully built and validated. A LabVIEW program was written to interface with the stepper motors and load cells of the device to control their movements. A mechanical testing protocol was developed and incorporated to enable the characterization of a variety of soft tissue structure-function relationships. Foundations were laid for studies using the planar biaxial device for research in a tissue-engineered nipple-areolar complex (NAC), pelvic floor disorders, and age-specific tendinopathy. The planar biaxial device has the potential to impact many areas of clinical research.

DESIGN OF A PLANAR BIAXIAL MECHANICAL TESTING DEVICE FOR SOFT
BIOLOGICAL TISSUES

A THESIS

SUBMITTED ON THE FIFTEENTH DAY OF APRIL 2017
TO THE DEPARTMENT OF BIOMEDICAL ENGINEERING
IN PARTIAL FULFILLMENT OF THE REQUIREMENTS
OF THE SCHOOL OF SCIENCE AND ENGINEERING

OF TULANE UNIVERSITY

FOR THE DEGREES

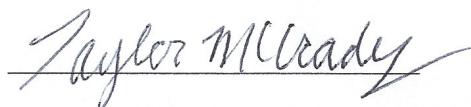
OF

MASTER OF SCIENCE

AND

BACHELOR OF SCIENCE IN ENGINEERING

BY

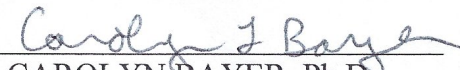


TAYLOR MCCRADY

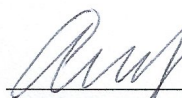
APPROVED:



KRISTIN S. MILLER, Ph.D.
DIRECTOR



CAROLYN BAYER, Ph.D.



ANNE-MARIE JOB, Ph. D.

ACKNOWLEDGEMENTS

First, I would like to thank Dr. Kristin Miller for her mentorship and guidance throughout the duration of my project and my time at Tulane. I would also like to thank the other members of my thesis committee, Dr. Carolyn Bayer and Dr. Anne-Marie Job, for the time they dedicated to my project. Next, I would like to thank the Tulane Biomedical Engineering department, the Center for Engaged Learning and Teaching (CELT), Newcomb Tulane College, and Center for Biomedical Research Excellence (COBRE, NIH P20GM103629) for their funding towards this project.

I am very grateful for the past and present members of the Biomechanics of Growth and Remodeling Lab for their support and friendship. Specific members of the lab I would like to acknowledge are Jonathan Nguyen, Cody O’Cain, and Benjamin O’Donnell. I would like to thank my good friend and colleague Jonathan Nguyen, for helping me construct the planar biaxial device from day one and for creating a customized MATLAB program for strain analysis of images of the tested biological tissues. I would like to acknowledge Cody O’Cain, who helped create many Solidworks files for the planar biaxial device, and spent countless hours helping to fabricate our custom-made parts. I would also like to recognize Benjamin O’Donnell, who was instrumental in laying down the foundations of the patellar tendon project.

Additionally, I would like to thank David Simon, a colleague of Dr. Miller’s, who provided invaluable advice and assistance during device construction and in LabVIEW software creation and troubleshooting.

None of this would be possible without my incredible family. My first and biggest thank you goes to my parents, Kim and Carey, who taught me confidence, determination, and perseverance. Thank you for always believing in me and for your endless love and support. My next thank you goes to my sister, Abigail, for her lifelong friendship and witty sense of humor. I am extremely grateful for my grandparents, Jalene, Terry and Diane, who are my biggest cheerleaders and give me some of my fondest childhood memories. I would like to thank my fiancé Derek for his unconditional love, his constant encouragement, and his ability to always make me laugh. I am grateful to his wonderful family, who took me in and treated me like family for countless weekends and holidays I could not spend with my own.

Finally, I'd like to dedicate my thesis to my great-uncle Roy. When you passed away ten years ago, I never would have imagined that a decade later, I would be graduating from a school of such high prestige with both my Master's and Bachelor's degrees in a field I love. Thank you for instilling a lifelong passion for learning in me from such a young age. I hope my life and accomplishments – past, present, and future – make you proud.

TABLE OF CONTENTS

List of Tables	viii
List of Figures	ix
Chapter 1: INTRODUCTION	1
I. INTRODUCTION	1
II. BACKGROUND.....	3
II.1 General Characteristics of Soft Tissues	3
II.1.1 Composition and Microstructure.....	3
II.1.2 Mechanical Response.....	3
II.1.3 Pathology and Motivation for Mechanics in Health and Disease	5
II.2 Constitutive Modeling.....	5
II.2.1 Growth and Remodeling	6
III. CHAPTER OVERVIEWS	6
Chapter 2: CONSTRUCTION OF THE PLANAR BIAxIAL MECHANICAL TESTING DEVICE	8
I. INTRODUCTION	8
II. BACKGROUND	9
II.1 Uniaxial versus Biaxial Mechanical Testing.....	9
II.2 History of the Planar Biaxial Device.....	9
III. DESIGN, CONSTRUCTION, AND PROGRAMMING OF THE PLANAR BIAxIAL DEVICE	11
III.1 Design Criteria	11
III.2 Hardware Research	12
III.2.1 Stepper Motors	12
III.2.2 Linear Screws and Motor Mounts.....	13
III.2.3 Load Cells	13
III.2.4 Camera and Accessories	15
III.2.5 Custom Parts	15
III.3 LabVIEW Programming	16
III.3.1 Motion Control	17

III.3.2 Data Acquisition (DAQ)	18
III.3.3 Image Acquisition (IMAQ)	18
III.3.4 Incorporation of Mechanical Testing Protocols.....	18
IV. DISCUSSION	19
V.1 Planar Biaxial Device Clinical Impact.....	20
IV.1.1. Abdominal Aortic Aneurysms.....	21
IV.1.2. Pelvic Organ Prolapse.....	21
IV.1.3. Tendinopathy and Sex Differences in Connective Tissues	21
V. CONCLUSION.....	22
Chapter 3: VALIDATION OF THE PLANAR BIAxIAL MECHANICAL TESTING DEVICE.....	23
I. INTRODUCTION	23
II. BACKGROUND.....	23
II.1 Skin Function, Composition, and Microstructure	23
II.2 Skin Mechanical Response and Research Motivation	25
III. OBJECTIVE	25
IV. METHODS	26
IV.1 Validation of Individual Systems of the Planar Biaxial Device	26
IV.4.1 Motion Control	26
IV.4.2 Data Acquisition (DAQ)	26
IV.4.3 Image Acquisition (IMAQ)	26
IV.2 Murine Skin Pilot Study	27
IV.4.1 Sample Preparation	27
IV.4.2 Biomechanical Testing	27
V. RESULTS	28
V.1 Individual Systems Validation.....	28
V.1.1 Validation of Motion Control	29
V.1.2 Validation of Data Acquisition (DAQ)	30
V.1.3 Validation of Image Acquisition (IMAQ)	30
V.2 Murine Skin Pilot Study Results	30
VI. DISCUSSION.....	31
VII. CONCLUSION	33

Chapter 4: FUTURE DIRECTIONS	34
I. Characterization of a Tissue-Engineered Nipple-Areolar Complex via Planar Biaxial Mechanical Testing.....	34
I.1 Introduction	34
I.2 Background.....	35
I.2.1 Function, Composition and Microstructure of Native Nipple-Areolar Complex.....	35
I.2.2 Clinical Motivation - Biocompatible Nipple-Areolar Complex Graft via Decellularization	35
I.2 Objective.....	37
I.3 Protocol Development	37
I.3.1 Sample Preparation.....	37
I.3.2 Biomechanical Testing	38
I.4 Discussion and Conclusion.....	39
II. Towards an Investigation of the Mechanical Properties of Pelvic Organs and Supporting Structures in Relation to Pelvic Organ Prolapse.....	39
II.1 Introduction	40
II.2 Background	40
II.2.1 Anatomy and Physiology of the Vagina	41
II.2.1.1 Composition and Microstructure of the Vaginal Wall	41
II.2.2 Anatomy, Physiology, Composition and Microstructure of the Uterosacral Ligament.....	41
II.2.3 Pelvic Floor Disorders.....	42
II.2.4 Previous Investigations of Uterosacral Ligament and Vaginal Mechanical Behavior in Relation to Pelvic Organ Prolapse.....	44
II.4 Experimental and Protocol Development	45
I.4.1 Experimental Design	45
I.4.2 Sample Preparation.....	45
I.4.3 Biomechanical Testing	46
I.4.4 Histology	47
II.5 Discussion	47
III. Examination of the Mechanical Properties of the Uterus and Cervix in Relation to Preterm Birth.....	48
IV. Foundational Developments for an Analysis of Age-Related Tendinopathy and Healing in the Murine Patellar Tendon	49
IV.1 Introduction.....	50
IV.2 Background.....	50
IV.2.1 Anatomy and Physiology of the Knee	50
IV.2.2 Tendon Composition and Microstructure.....	51
IV.2.3 Age-Specific Patellar Tendinopathy.....	52
IV.4 Experimental and Protocol Development.....	52

IV.4.1 Experimental Design	52
IV.4.2 Patellar Tendon Biopsy Punch.....	53
IV.4.3 Patellar Tendon Dissection.....	54
IV.4.4 Biomechanical Testing	54
IV.4.1.1 Patellar Tendon Grip Research and Design.....	55
IV.4.1.2 Biomechanical Testing Protocol.....	56
IV.4.5 Histomorphologic and Biochemical Analysis	57
IV.4.6 RNA Sequencing Analysis	57
IV.5 Discussion.....	57
V. Analysis of Sex Differences in Rotator Cuff Tendons Via Biaxial Mechanical Testing.....	59
Chapter 5: OVERALL CONCLUSIONS.....	61
I. Successful Design, Construction, and Programming of a Custom Planar Biaxial Mechanical Testing Device.....	61
II. Validation of the Planar Biaxial Mechanical Testing Device via Pilot Study in Murine Skin	62
APPENDIX	63
REFERENCES	131
BIBLIOGRAPHY	142

LIST OF TABLES

Table 1: Representative Sample of Pictures Taken During Motion Control Validation ..	28
Table 2: Comparison of Young's Modulus Experimental Values vs. Literature Value ...	31
Table 3: Overview of Uterosacral Ligament and Vagina Mechanical Testing In Relation to Pelvic Organ Prolapse Experimental Course.....	45
Table 4: Overview of Age-Specific Murine Patellar Tendinopathy Experimental Course	53

LIST OF FIGURES

Figure 1: General Stress-Strain Curve for Collagenous Tissues	3
Figure 2: Loading and Unloading Curves for Elastic and Inelastic Materials	4
Figure 3: General Concept of Uniaxial and Biaxial Mechanical Testing.....	9
Figure 4: Schematic of an Assembled Planar Biaxial Device	12
Figure 5: Flow of Communication between the Stepper Motors and Computer	12
Figure 6: Flow of Communication between the Load Cells and Computer	14
Figure 7: Optical Strain Tracking Limitation	14
Figure 7: Screenshots of LabVIEW Output During IMAQ Verification	20
Figure 8: The Layers of the Skin	24
Figure 9: Representative Load Cell Calibration Graph	29
Figure 10: Screenshots of LabVIEW Output During IMAQ Verification	30
Figure 11: Representative Load Displacement Data from Murine Skin Pilot Study Superimposed over Groves et. al. Data.....	30
Figure 12: Representative Stress Strain Data from Murine Skin Pilot Study.....	31
Figure 13: Schematic of the Decellularization and Engraftment Process of the Nipple- Areolar Complex.....	36
Figure 14: Three-Dimensional Model of a Cruciform Tissue Sample Gripped in the Planar Biaxial Device.....	37
Figure 15: Diagram of the Pelvic Floor	40
Figure 16: Example of Pelvic Organ Prolapse Progression, Courtesy of Web MD	43
Figure 17: Vaginal and USL Samples Stamped into a Cruciform Shape for Biomechanical Testing.....	46

Figure 18: Histologic Images of Murine Vaginal Tissue Before and After Enzymatic Digestion of Elastin.....	47
Figure 19: Patellar Tendon Anatomy.....	50
Figure 20: Tendon Hierarchical Structure	51
Figure 21: Graphical Representation of the Patellar Tendon Biomechanical Testing Protocol.....	56
Figure 22: Hypothesis Regarding Age-Specific Patellar Tendinopathy.....	58

Chapter 1: INTRODUCTION

I. INTRODUCTION

“Biomechanics can be defined as the development, extension, and application of mechanics to answer questions of importance in biology and medicine.” [1]. While biomechanics is a relatively new field and covers a wide variety of topics, motivation for biomechanics research can be explained by a simple simile. Trying to understand biology and medicine without biomechanics is like trying to understand how an airplane works without aerodynamics. Aerodynamics helps engineers to comprehend an airplane’s normal function, create designs, and predict its performance. Biomechanics helps us understand an organisms normal function, predict its performance, and create artificial interventions such as prosthetics, implants, and catheters [2].

One important area of study in biomechanics is the mechanical properties of soft tissues. Mechanical properties of soft tissues are elicited experimentally and can be predicted via constitutive relationships. The overall goal of a constitutive relationship is to “predict the mechanical behavior of a material under a generalized loading state” [13]. Constitutive relations are determined via theory, specifically designed experiments, or educated guesses. One specifically designed experiment used to determine constitutive relations is mechanical testing. Particularly, planar biaxial mechanical testing of soft tissues, or testing a soft tissue sample in two directions in the same plane, has proven to mimic physiologically relevant conditions for most soft tissues.

Therefore, the overall aim of this thesis is to elucidate structure-function relationships of soft biological tissues. The overall objective of this thesis was to build a custom planar biaxial mechanical testing device to characterize the mechanical properties of soft biological tissues in order to identify appropriate constitutive relations. The specific aims of this study are as follows.

1. ***Specific Aim 1: To design, build, and validate a custom planar biaxial mechanical testing device.*** Construction of this device will allow for studies in various soft biological tissues. The device will be validated by performing a small pilot study in murine skin. Information from these studies will further our knowledge of tissue mechanical behavior, pathology, and aid in the creation of clinical treatment and prevention plans.
2. ***Specific Aim 2: To develop customized protocols to permit assessment of additional soft tissues of interest.*** Experimental study design and protocol developments for a study for a tissue-engineered nipple areolar complex (NAC) and two aging studies – one in human vaginal and uterosacral ligament in relation to pelvic organ prolapse (POP) and another in the murine patellar tendon injuries – will be described. Specifically, biaxial mechanical testing will be used to elucidate mechanical properties of the NAC and women's reproductive tissues and uniaxial testing will be used for murine patellar tendon. These mechanical testing protocols were chosen to best mimic the physiological conditions of each tissue.

II. BACKGROUND

II.1 General Characteristics of Soft Tissues

II.1.1 Composition and Microstructure

Generally, soft tissue structure is dependent upon the function(s) it may perform.

Most soft tissues' extracellular matrix is comprised of the following four structural constituents: collagen, elastin, glycosaminoglycans/proteoglycans, and smooth muscle cells. Healthy soft tissues regulate the balance of production, removal, and organization of these structural constituents based on the loading states of the soft tissue [3].

II.1.2 Mechanical Response

Soft tissues share general characteristics that can describe their mechanical behavior, despite their countless differences. The first of these characteristics is the nonlinearity of soft tissue's stress-strain behavior. In general, soft tissues demonstrate a compliant response at low levels of stress and strain, but exhibit increased stiffness as more stress and strain is applied to the material

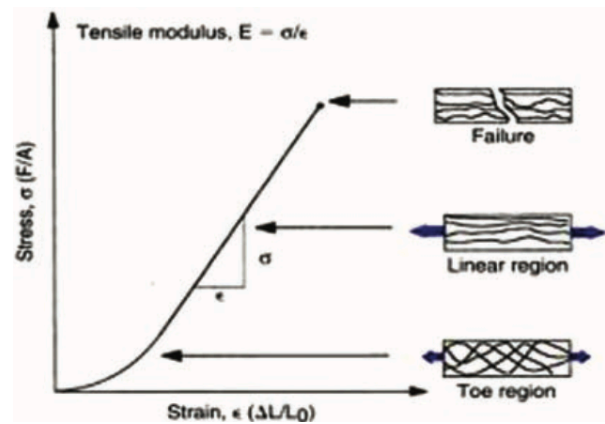


Figure 1: General Stress-Strain Curve for Collagenous Tissues In the toe region, the fibers of the soft tissue are in a “crimped” state. The linear region is when the fibers are experiencing more stress and strain than the toe region, but the fibers of the soft tissue are not experiencing microtrauma. Just before the soft tissue has reached its ultimate tensile stress, the soft tissue begins to experience micro-failures in its fibers. Eventually, the soft tissue reaches catastrophic failure and breaks. Figure from [4].

[1]. In Figure 1, a general stress-strain curve of collagenous tissues is given to illustrate this phenomenon.

Anisotropy is the second characteristic common to soft tissues. Anisotropy is a directionally dependent mechanical response of a soft tissue due to differences in microstructural/compositional organization. An example of a tissue that is anisotropic is

tendon. Fibers of type I collagen, the main structural constituent of tendons, orient themselves in axes of the maximum force to allow for increased deformations without overstretching the tissue [1].

Elasticity is a material property where the material does not lose its shape after deformation, and the material loads and unloads on the same curve as shown in Figure 2. Not all materials, however, are elastic. Materials that are inelastic load and unload on different curves. Figure 2 also demonstrates this phenomenon.

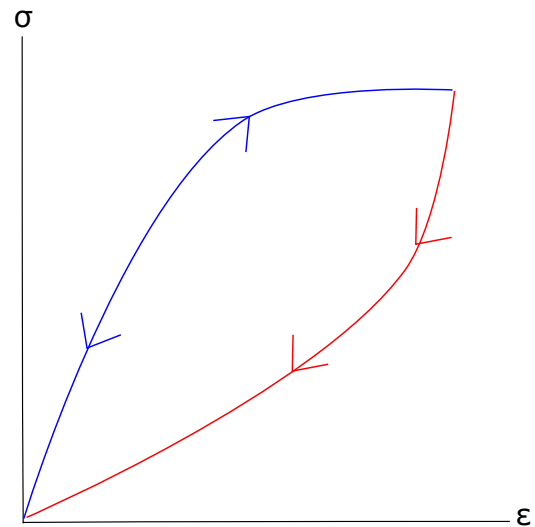


Figure 2: Loading and Unloading Curves for Elastic and Inelastic Materials. The blue curve represents elastic materials, which load and unload on the same stress strain curve. Inelastic materials, however, load and unload on different stress strain curves. Inelastic materials will load on the blue curve, but unload on the red curve.

Soft biological tissues, however, tend to exhibit both elastic and inelastic properties. When a stress is initially applied, soft tissues

behave like an inelastic material. As stress is continually applied, soft tissues begin to behave more like elastic materials and after a certain period, almost converge to the same loading and unloading curves. Materials that behave in this manner, specifically soft biological materials, are said to be pseudoelastic. The time-dependent process of converging to identical, or almost identical, loading and unloading curves is called hysteresis. During mechanical testing, soft tissue samples must be as elastic as possible to mimic *in vivo* loading conditions because stresses are continually applied to soft tissues in the human body. Therefore, preconditioning of the soft tissue samples is necessary prior to mechanical testing to acquire the most accurate data as possible.

II.1.3 Pathology and Motivation for Mechanics in Health and Disease

Biomechanics has played a vital role in numerous developments in modern biology and medicine. Advancements in inventions for cardiovascular health, such as prosthetic heart valves, heart assist devices, and hemodialysis machines, can be attributed to biomechanics. Orthopaedics has particularly benefitted from biomechanics research due to the high incidence of musculoskeletal injuries in our society. The most important long term contribution of biomechanics to modern biology and medicine, however, is increased understanding of physiology. Current and future prevention and treatment plans will be improved as our knowledge of the mechanics of the human body deepens. They will better mimic the structure and function of the tissue or organ they are meant to help or replace [2].

II.2 Constitutive Modeling

Constitutive modeling is considered valid when the boundary conditions, and other conditions of interest such as physiologically relevant range of deformations, for which it was created are emulated. For example, Young's modulus for a metal that was mechanically tested uniaxially should only be considered valid when the metal sees a similar uniaxial loading state and design environment to the mechanical testing environment [1]. Thorough constitutive models are most useful when they can apply to a variety of boundary conditions. Accurate constitutive models should be able to predict the tissue's behavior, in addition to describing it [1]. Therefore, multiaxial testing (e.g. biaxial) allows for the application of various loading states on the same tissue sample and provides information to predict the tissue's behavior [1]. Once a constitutive model can accurately predict a tissue's behavior, it may be extended in order to impact clinical practice through the creation of patient-specific treatment and prevention plans.

II.2.1 Growth and Remodeling Model

While mechanical properties of soft tissues are important to consider, it is also important to examine other characteristics of soft tissues. One characteristic that makes soft tissues unique is their ability to maintain homeostasis by adapting to their evolving mechanical environment. Soft tissues respond to disease, injury, and fluctuations to their mechanical environment via growth (change in mass) and remodeling (change in structure) [3]. The Growth and Remodeling (G&R) Models, which consist of three specific constitutive relations, have recently been formulated to better predict soft tissue mechanical behavior during physiological processes such as aging, aneurysm formation, and elevated blood pressure [5-8]. These soft-tissue specific G&R models all share the same fundamental hypothesis that cells seek to establish, maintain, or restore a preferred biomechanical state of stress.

III. CHAPTER OVERVIEWS

This thesis consists of five chapters. Chapter one is an introduction and provides background information and foundational research motivation for the subsequent chapters. The contents of chapter two address, in part, specific aim one. It describes the design and construction a planar biaxial device, as well as a corresponding LabVIEW program to control the movements of the device, to mechanically test soft biological tissue samples. Design criteria, details about parts purchased and fabricated, and the clinical impact of the planar biaxial device are discussed. Chapter three addresses the rest of specific aim 1 and presents the work done to validate the planar biaxial device via the mechanical characterization of murine skin. Skin was chosen to validate the planar biaxial device because it is an anisotropic soft tissue.

Chapter four describes the future directions of this thesis and addresses specific aim 2. Those future directions include a mechanical evaluation of a tissue-engineered nipple-areolar complex, characterization of the mechanical properties of pelvic floor organs in relation to pelvic organ prolapse, and an analysis of age-specific murine patellar tendinopathy. For each study, extensive literature searches and protocol developments were done to lay down the foundations for these studies to take place in the future. Lastly, chapter five will discuss the overall conclusions of this thesis.

Chapter 2: CONSTRUCTION OF THE PLANAR BIAXIAL MECHANICAL TESTING DEVICE

I. INTRODUCTION

Mechanical testing of soft tissues is required for the development and validation of constitutive relationships, which are valuable for many physiological, surgical, and medical device applications for soft biological tissues [13]. Generally, there are two kinds of planar mechanical testing: uniaxial and biaxial. In the past, mechanical testing of soft tissues was restricted to uniaxial testing. Uniaxial mechanical testing applies load or deformation along one axis, while biaxial mechanical testing utilizes two. Uniaxial mechanical testing cannot account for multiaxial behavior, and therefore cannot be used in three-dimensional constitutive relationships [13]. Biaxial mechanical testing, however, can recreate multiaxial behavior similar to what soft tissues experience *in vivo*. Therefore, there is a need to create mechanical testing devices that can perform biaxial mechanical tests in order to properly inform constitutive models [13].

The objective of this chapter is to describe the design and construction of a custom planar biaxial device, as well as a corresponding LabVIEW program to control the movements of the device. A customized soft tissue planar biaxial mechanical testing device was constructed to determine appropriate constitutive models for soft tissues. A LabVIEW program was created to interface with the stepper motors and load cells of the device to control their movements and incorporated mechanical testing protocols.

II. BACKGROUND

II.1 Uniaxial versus Biaxial Mechanical Testing

The difference between uniaxial and biaxial mechanical testing is demonstrated in Figure 3.

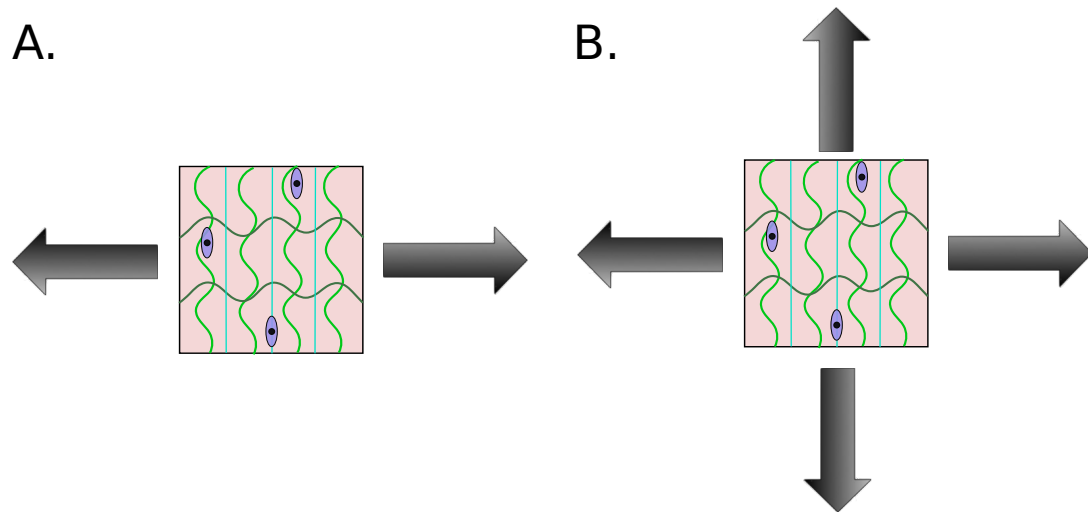


Figure 3: (A) General Concept of Uniaxial Mechanical Testing. Biological tissue sample is pulled in one axis. (B) General Concept of Biaxial Mechanical Testing. Biological tissue sample is pulled in two axes

Given the anisotropic nature of soft tissues, uniaxial testing does not provide sufficient information to quantify the material properties of soft tissue since the tissue is only tested on one axis [13] Biaxial testing, however, permits to quantification of the physiologically-relevant, multiaxial mechanical behavior, as well as to formulate a mathematical model [13].

II.2 History of the Planar Biaxial Device

Biaxial testing of soft tissues was originally developed using methods performed in investigations of rubber elasticity by Rivlin and Saunders, and Treolar [14, 15]. Treolar in 1948 developed techniques to apply two separate variable strains in two perpendicular directions while also measuring stresses in both directions [15]. Axial stretch ratios, however, could not be independently controlled. In 1951, Rivlin and Saunders created an

improved biaxial device that applied biaxial loads to rubber sheets. Rivlin and Saunders's approach and that of others that followed him allowed for further insights into the complex mechanical behavior of rubber.

Lanir and Fung [16, 17] constructed and used the first planar biaxial device to mechanically test rabbit skin in 1974. They tested 3-6cm square skin samples mounted with up to 68 individual attachments, or 17 attachments on each side. Motion control was regulated with a function generator. Strain was measured in the center of the sample with pairs of lines. In 1976, Tong and Fung used data from these experiments to develop a constitutive model, which is still used today to describe and predict the mechanical behavior of soft biological tissues such as skin, pericardium, and visceral pleura [18].

Vito [19] reports the next major developments in the planar biaxial device. Particle tracking, as opposed to tracking strain with pairs of lines, was introduced [19]. This technology permitted computation of the entire in-plane strain tensor, as well as the ability to control the computer in real time. The next technological development, introduced by Khalsa, was the capability to ascertain the tissue sample's material axis [20]. Previously, identification of a tissue specimen's material axis was done by gross observation of the fiber orientation. Some tissue samples, however, were too small to identify fiber orientation. Until Vito's technique, identification of small tissue orientation was not possible. Refer to figure 6 (a) in [13] for an illustration of rotating a material's testing axis is shown.

More recent versions of the planar biaxial device include the capability to test for the effects of in-plane shear, which earlier testing apparatuses lacked. This limitation was mainly due to added costs and complexity to the device design. Khalsa et. al. [20]

introduced a more cost-effective approach in 1997 by rotating the tissue sample's material axes to the test axes by using rotating carriages. The rotating carriages consisted of pulleys (mounted to a rod) attached to a bearing placed equally on each side of the sample. The pulleys were attached the sample with 000 silk sutures looped through four surgical staples [21]. This novel configuration permitted free movement of the rotating carriage and eliminated the extra costs of individual motors and load cells. To see the testing set-up, refer to Figure 6 (b) by Sacks [13]. Inducing in-plane shear strain allowed investigators to model for the first time a tissue's response to in-plane shear. Figure 3 demonstrates the difference between previous biaxial mechanical testing and in-plane shear mechanical testing.

III DESIGN, CONSTRUCTION, AND PROGRAMMING OF THE PLANAR BIAxIAL DEVICE

III.1 Design Criteria

The planar biaxial device must adhere to certain design criteria. The first criterion of the device was the ability to house multiple types of soft tissues. The device must be versatile enough to permit assessment of women's reproductive tissues (i.e. cervical and vaginal) as well as connective tissues (i.e. tendon and ligament), which exhibit significantly different mechanical properties. The next required component of the device is a watertight testing chamber to maintain a 37°C saline bath during tissue testing to mimic an *in vivo* environment in an *in vitro* experiment. The third criterion for the device is the capability to attach to and interface with the load cells and stepper motors. The load cells and stepper motors control and measure the amount of stress and strain placed on the tissue and the movements of the device, respectively. The user of the device must have the capability to control both to run a successful mechanical test. The final requirement for the device is the

ability to switch out the grips that hold the tissue sample in place during mechanical testing. Previous work shows that different gripping methods are used for different tissues [22, 23]. Since the planar biaxial device will be used to test different tissues, the ability to incorporate tissue-specific grips is necessary.

III.2 Hardware Research

A complete list of the parts ordered for this planar biaxial device can be found in Appendix A, and a schematic of a constructed device can be seen in Figure 4. The next few sections will address the main pieces of hardware of the device.

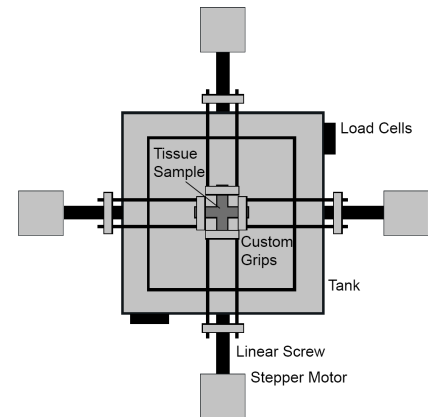


Figure 4: Schematic of an Assembled Planar Biaxial Device. Courtesy of Jonathan Nguyen.

III.2.1 Stepper Motors

A flow chart of the communication lines between the stepper motors and the computer of the planar biaxial device can be shown in Figure 5 below.

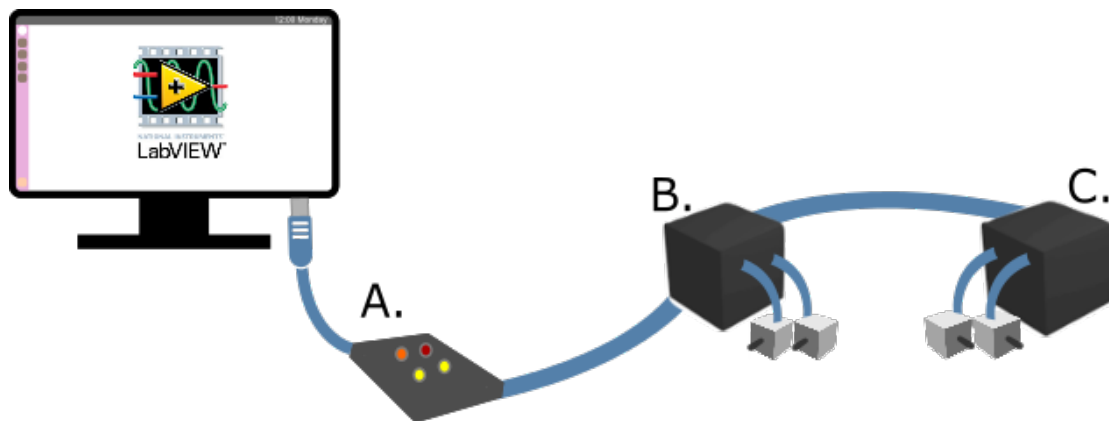


Figure 5: Overview of Motion Control System Hardware and Software Setup And Communication. Two Stepper Motor Controllers (B,C) are daisy chained to communicate to four stepper motors at one time. A USB Indicator (A) provides the connection for the LabVIEW program to send commands to the stepper motors.

There are four NEMA-17 stepper motors for the planar biaxial device from Advanced Micro Systems. A MAX-420 Controller, also from Advanced Micro Systems, controls their movements through a list of commands found in Appendix B1. Two MAX-420 controllers are daisy-chained to allow all four motors to communicate with the computer.

Finally, a SIN-11-USB is a serial converter that connects Advanced Micro Systems components to the user's computer [Advanced Micro Systems, Torrance, CA].

III.2.2 Linear Screws and Motor Mounts

Two 10x2mm lead screws are placed on each side of the bioreactor tank. Both lead screws are attached to NEMA-17 motor mounts. The other side of the screws fit through holes on all sides of the bioreactor tank. This provides a connection for the stepper motors to the tissue sample inside the bioreactor [Thomson BSA, San Jose, CA].

III.2.3 Load Cells

Two low range (50-500 gm) miniature load cells were originally purchased for the planar biaxial device [Honeywell, Morristown, NJ]. The temperature range of the load cells is 15-70°C, which is wide enough to accommodate the temperature of the saline bath during mechanical testing (37°C, body temperature). Additionally, the load cells are submersible. This gives the planar biaxial device the ability to conduct mechanical testing in an incubator, if the user decides an incubator is necessary for their testing environment. Due to unforeseen changes in grip design during pilot studies, it was found that the original load cells did not have the appropriate range for the tissues of interest (orthopaedic and women's reproductive). An extensive literature search was done to ensure that a new set of load cells are appropriate for these tissues. A summary of this literature search can be found in Appendix K. Two 5 lb. (approximately 22.25 N) load cells will be used in place of the original load cells [Honeywell, Morristown, NJ]. The temperature range of the load cells is -53-121°C, which still accommodates the temperature of the saline bath during mechanical testing. The new load cells are also submersible. One advantage to the new load cells over the original set is an overload stop. This will prevent users in the future from accidentally overloading the cell and permanently damaging it. Another advantage is

the scalability of this load cell model. If a load cell with a smaller or higher range is needed, another version of this load cell can be ordered with a different range while the size of the physical load cell is maintained, since this model comes in a wide variety of ranges (1000g – 10 lbs). This will allow for an interchange of load cells from the device as necessary, without having to fabricate different load cell holders each time.

The load cells communicate with a National Instruments 24-bit analog input module (NI 9237) through an RJ-50 cable and a screw terminal adaptor [National Instruments, Austin, TX]. The analog input module communicates with the computer through a compactDAQ Chassis [cDAQ 9171, National Instruments, Austin, TX], equipped with a USB port. A flow chart of the communication lines between the load cells, DAQ hardware, and computer can be seen in Figure 6 below.

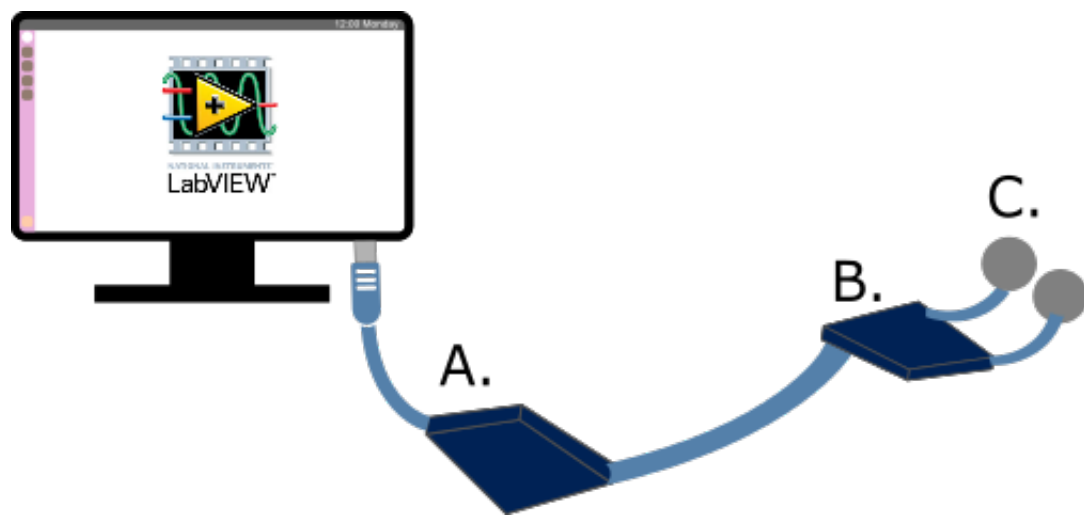


Figure 6: Overview of Data Acquisition System Hardware and Software Setup And Communication. Two Honeywell load cells (C) are wired to a screw terminal adapter (B). Load cell output, in voltage, is sent to a LabVIEW program for processing via a cDAQ 9171 Chassis and 24 bit Analog Input Module (A).

III.2.4 Camera Accessories

A Manta G-419 A” NIR CMOS Camera [Edmund Optics, Barrington, NJ] will be used for strain analysis of the tissue samples. The camera will provide a live feed of the tissue during mechanical testing, take overhead photos of the tissue samples, and be supported through a series of accessories to hold the camera steady during mechanical testing.

III.2.5 Custom Parts

Four parts of the device were custom made, either by 3D printing by Innovative Digital Manufacturing [New Orleans, LA] or fabricated on site. The bioreactor tank, cruciform and load cell holders, and the loading arm to linear screw connectors were originally 3D printed with polycarbonate-ISO (PC-ISO), which is biocompatible and commonly used for medical device applications. Drawings for these parts can be found in Appendix F1, F3, and F6. All three parts, however, have since been modified and fabricated on site.

The size of bioreactor tank was originally 7.5” x 7.5” x 2”. It was scaled up to 12” x 12” x 2” due to changes in grip design that required more room inside the tank using a Tormach CNC mill on site [Tormach, Waunakee, WI]. Due to time constraints and technical difficulties with the CNC mill, an interim tank was made of low density polyethylene and a permanent tank will be made of glass-filled polycarbonate to satisfy previously discussed design criteria. Drawings for both bioreactor tanks can be found in Appendices F1 (7.5” x 7.5” x 2”) and F2 (12” x 12” x 2”).

Since new load cells were purchased after the original cruciform and load cell holders were made, a similar but slightly different design was made on site via digital light processing stereolithography to solidify photosensitive resin to incorporate the new load

cells. The cruciform and load cell holder for the Model 31 (original) load cells can be found in Appendix F3, and the corresponding part for the Model 34 (new) load cells can be found in Appendix F4.

After the device was assembled, it was found that if the original linear screw connectors, shown in Appendix F6, needed to be removed, that the entire device would have to be taken apart and put back together. A new version was made to allow for this part to be taken out without disassembling the rest of the device. It was manufactured by Precision Cutting, LLC [Pineville, LA] and its drawing file can be found in Appendix F7.

Lastly, the camera mounting plate was fabricated with acrylic on site, and its drawing can be found in Appendix F5. Acrylic was used as an economical alternative to polycarbonate.

In addition to the four parts mentioned, grips were designed to more easily secure a sample to the device. Due to the intricacy and small size of the grips, they were outsourced to Precision Cutting, LLC [Pineville, LA] for manufacturing. Drawing files for these grips can be found in Appendix G1.

III.3 LabVIEW Programming

LabVIEW, which is short for Laboratory Virtual Instrument Engineering Workbench, is a visual programming platform that allows users to create custom applications to interface with real world data and signals. Each file in LabVIEW is called a virtual instrument (VI), and can be used in combination with other VI's to run tests, gather measurements, or to control hardware. LabVIEW VIs were constructed to control the movements and acquisition of data from the planar biaxial device. These VIs can be placed in one of three categories: stepper motor interface, data acquisition, and image acquisition.

III.3.1 Motion Control

Motion Control VIs were designed to control the movements of the stepper motors of the planar biaxial device. There are three subcategories these VIs fall into: functional global variables, setting properties, and motion.

Functional global variables (FGVs) are VIs that provide benefits similar to those of a global variable. They are easier to maintain and debug than global variables. They reduce the chance of race conditions, which is when a system attempts to perform two or more operations when the system means to perform these operations in a specific order. FGVs are used for the planar biaxial device to allow the user to select the controller of the stepper motors and to set constants such as the number of steps per revolution of the stepper motor.

Setting motor properties are a group of VIs that communicate with daisy-chained controllers to set important properties of the stepper motors. These properties include the step position, resolution, and velocity of the stepper motor. Communication with the stepper motor is done with a series of controller commands, listed in Appendix B. All of the VIs in this group are able to set these properties to a single motor, a pair of motors (in either the x or y axis), or all four motors of the planar biaxial device.

Motion VIs are used to physically move the stepper motors of the planar biaxial device. This interface is adaptable to different units or locations the user may need the motors to go. The user can move the motors by angular distance (in degrees) and linear distance (in millimeters). Both of these individual VIs convert either angular or linear distance into the number of steps necessary for the motor to move to where the user specified. In addition, this interface allows the user to send the motor(s) back to their origins or to a reference location.

III.3.2 Data Acquisition (DAQ)

An essential component of the LabVIEW software written for the planar biaxial device is the ability to acquire force data from the load cells. Data acquisition (DAQ) in LabVIEW is accomplished using the Measurement and Automation Explorer (MAX). This allows access to the DAQ assistant, which is a graphical user interface that will automatically generate LabVIEW code from user inputs, and NI-DAQmx toolbox, which accommodates for more complex data acquisition applications. Load cells output their data as voltage values, which the generated LabVIEW code then converts to known loads. The data acquired from the load cells can be exported into a Microsoft Excel file to be analyzed in Excel or MATLAB (Mathworks, Natick, MA).

III.3.3 Image Acquisition (IMAQ)

Image acquisition (IMAQ) is a necessary part of the LabVIEW software for the planar biaxial device. IMAQ will be used to save images taken by the camera to be saved for data analysis, conduct real-time optical strain analysis, and trace a boundary to track the particles that will be placed in the tissue samples prior to mechanical testing. Some of the data analysis, specifically strain analysis, will take place in custom-made MATLAB software (Mathworks, Natick, MA).

There are two primary ways to track strain in real-time: grip-to-grip and optical. Grip-to-grip strain is calculated based on the distances between the edges of each grip. Optical strain tracking, however, calculates deformation based on markers placed onto the soft tissue itself. This provides a more accurate calculation of strain because it is tracking deformation of the actual soft tissue, instead of a set distance between the two grips.

III.3.4 Incorporation of Mechanical Testing Protocols

The motion control, data acquisition, and image acquisition VIs will all be used as subVIs within one VI, called “Mechanical Test File.vi”, during any mechanical test. The

VI will have a user-friendly interface so the user can run through a specified mechanical testing protocol, which will partially be dependent upon the type of tissue they are testing. Using one large VI, rather than multiple small VIs, will streamline the mechanical testing process and will reduce human error.

IV. DISCUSSION

The planar biaxial device was designed with versatility and utility in mind. All hardware, if necessary, can be replaced with similar hardware. Hardware was attached to an acrylic base via 8-32 and 1/4-20" screws for stability, as well as the ability to swap out parts. Modifications were made to the device and its software throughout the assembly process to meet the design criteria set before device construction.

The size of the bioreactor tank was augmented to accommodate changes in grip design. Changes in grip design were made to increase repeatability of the user placing the tissue sample inside the bioreactor in the same plane. This is important in running a successful mechanical test for two reasons. The first reason is that if the tissue falls out of plane, then a torque is introduced to the tissue and invalidates mechanical properties elucidated from the test. Secondly, the camera stops tracking the particles properly when the tissue falls out of plane.

New load cells were purchased to allow for other soft tissues to be tested without overloading the smaller range load cells. It was found that other soft tissues, such as murine patellar tendon and uterosacral ligament, have felt loads greater than 50 grams, which was the maximum load of the original load cells [9-12, 70, 71, 75]. The new load cells have a maximum load of 5lbs, which allows for other tissues to be tested without sacrificing accuracy of data output by the load cell.

Software was designed to be user-friendly and reusable across all soft tissues to be tested in the biaxial device. Software was created for motion control, data acquisition, and image acquisition. All three aspects of software can be controlled in one VI during a mechanical test. In addition, this VI allows for a mechanical test to be either load-dependent or strain-dependent. Finally, all data acquired during a mechanical test is sent to an excel file for further analysis.

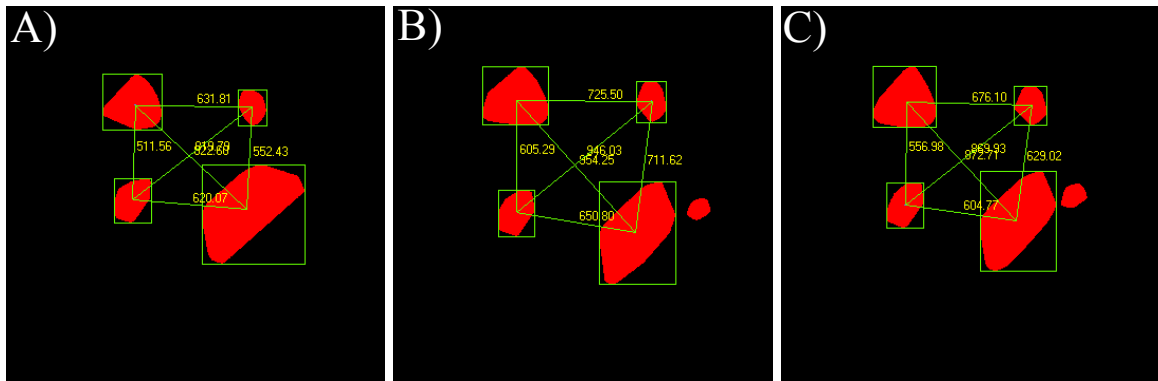


Figure 7: Optical Strain Tracking Limitation. Figure (A) shows the reference position of the particles prior to movement. Figures (B) and (C) show a portion of the original particle splitting away. The LabVIEW code, however, masks out this portion of the particle and continues to track strain.

One limitation with this device is with the real-time optical strain tracking. When the dots, or particles, of activated charcoal are placed onto the soft tissue sample, the sample may not be perfectly flat. When the soft tissue is pulled by the biaxial device, it can cause portions of the dots to break away from the original particle. The LabVIEW code was written, however, to mask out portions of particles that break away from the original. This ensures that the LabVIEW code does not lose the original particle and continues to track strain in real-time.

IV.2 Planar Biaxial Device Clinical Impact

Quantification of soft tissue structure-function relationships will not only strengthen our understanding of their mechanical behaviors, but will also provide necessary

information to treat diseases affected by soft tissue mechanics. A few of these diseases include abdominal aortic aneurysms, pelvic organ prolapse, and tendinopathy.

IV.2.1 Abdominal Aortic Aneurysms

Abdominal Aortic Aneurysms (AAA) are a dilation of the Abdominal Aorta (AA), and was the 13th leading cause of death in 1987 [24]. A study done by Vande Geest [22] used biaxial mechanical testing to quantify the 3D mechanical response of both AA and AAA to compare differences between the two soft tissues. They found that AAA's are caused by an increase in stiffness and a decrease in the extensibility of the tissue's behavior [22]. Using this information, predictions of high-risk AAA patients become more reliable.

IV.2.2 Pelvic Organ Prolapse

Pelvic Organ Prolapse (POP) is the downward descent of pelvic organs due to weakened or over-stretched muscles, which results in the protrusion of the vagina and/or uterus. While there are numerous risk factors for POP [25], structure-function relationships for the pelvic organs have not been entirely identified. Biaxial mechanical testing of pelvic organs, such as the vagina, uterus, or bladder, could help elucidate these structure-function relationships to further our understanding of the mechanical etiology of POP. Ultimately, this information could be used to treat patients with POP and prevent patients from developing severe cases of POP.

IV.2.3 Tendinopathy and Sex Differences in Connective Tissues

As previously discussed, tendinopathy is the over-use of tendons. Rotator cuff injuries are a common location for tendinopathy, just behind the knee and spine [26]. While tendons have predominantly been tested uniaxially [27-30], biaxial testing the tendons of the rotator cuff is important since rotator cuff tendons see multiaxial loads *in vivo* [23]. In addition, the probability of a connective tissue injury occurring in women is higher than in men [31]. The underlying cause of this, however, is unknown. Establishing structure-

function relationships through biaxial mechanical testing of rotator cuff tendons between men and women would not only move forward our knowledge of the mechanical behavior of the tendons of the rotator cuff, but would also deepen our understanding of connective tissue injury differences between men and women.

In a recent biaxial study of the Supraspinatus tendon done by Szczesny and others [23], a relationship was found between collagen fiber organization and the transverse and longitudinal stresses. He formulated a structural model that successfully fit the longitudinal stresses, but could not accurately fit the model to transverse stresses. Further analysis of the model is necessary to determine a model to fit the transverse behavior of the Supraspinatus tendon.

V. CONCLUSION

A planar biaxial mechanical testing device was constructed for small, soft biological tissue samples. Extensive research went into hardware purchasing and design. LabVIEW code was created for motion control, data acquisition, and image acquisition. User-friendly interfaces were designed in LabVIEW to run mechanical testing protocols. Motion control, data acquisition, and image acquisition systems were successfully verified. The planar biaxial device has the potential to impact many areas of clinical research.

Chapter 3: VALIDATION OF THE PLANAR BIAXIAL MECHANICAL TESTING DEVICE

I. INTRODUCTION

Skin is generally accepted to be anisotropic *in vivo* [17, 32], however, *ex situ* biaxial tests performed to characterize mechanical properties of rabbit skin found that skin exhibited orthotropic properties, symmetric with respect to two normal planes [17]. Orthotropic properties of skin greatly facilitate the mechanical characterization of the soft tissue via planar biaxial devices. Skin is an excellent choice for a pilot study to verify the planar biaxial device due to its orthotropy and well characterized mechanical properties [17, 32]. While preliminary verification of the planar biaxial device was successful, a full pilot study needs to be conducted to confirm proper function of all systems prior to the conduction of further studies. Therefore, the objective of this chapter is to characterize the mechanical properties of murine skin to validate the planar biaxial device. Once validated using skin, the constructed planar biaxial device will be capable of characterizing behaviors of other tissues of clinical relevance, such as the nipple-areolar complex.

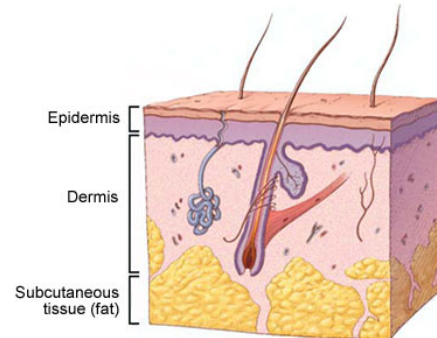
II. BACKGROUND

II.1 Skin Function, Composition, and Microstructure

Skin is the largest organ in the body and functions in many capacities. It serves as a barrier for the body from the external environment, contains the tissues, organs, and fluids of the body, regulates temperature, provides sensation, and creates and stores vitamin D. Mechanical properties of skin, and subsequently the extracellular matrix structure and composition, highly dictate the skin's ability to successfully perform its function.

The skin is comprised of four layers: epidermis, dermis, subcutaneous tissue (superficial fascia), and deep fascia. [33].

The epidermis is the most superficial layer of skin and is made of keratinized, stratified, or layered, epithelium with a tough outer layer consisting of the fibrous protein keratin. This outer layer is continuously shed away and replaced with new cells from the basal layer. The epidermis completely regenerates every 25 to 45



© Mayo Foundation for Medical Education and Research. All rights reserved.

Figure 8: The Layers of Skin. Courtesy of Mayo Clinic.

days, and is avascular. Nourishment of the epidermis arises from subcutaneous vessels in the dermis. There are many afferent nerve endings in the epidermis that provide sensations such as touch, pain, and heat [33].

The dermis, which resides directly under the epidermis, is created from a dense network of collagen and elastic fibers. Strength, toughness, and resilience of skin is determined by the amount of collagen and elastin fibers present. In addition, the primary direction of collagen fibers determines cleavage and wrinkle lines in skin. Structures such as hair follicles, arrector pili muscles, and sebaceous glands are all present in the dermis.

The layer directly underneath the dermis is the subcutaneous tissues, or superficial fascia. This layer contains loose connective tissue and adipose tissue. Structures present in subcutaneous tissue are the deepest parts of sebaceous glands, blood and lymphatic vessels, and cutaneous nerves [33].

Lastly, the deepest layer of skin is the deep fascia. The deep fascia is comprised of dense, organized connective tissue. Individual muscles and neurovascular bundles extend

from the internal side of the deep fascia. The deep fascia divides muscles into groups, and lies between musculoskeletal walls. In addition, deep fascia forms retinacula, which hold tendons in place during movement in joints, and bursae, which are closed sacs that contain fluid to prevent friction and provide free movement of structures over each other [33].

II.2 Skin Mechanical Response and Research Motivation

While there are differences between murine and human skin, the two tissues have comparable mechanical properties [34]. Skin is compliant and exhibits an elastic behavior [35]. It was found that skin swells 3-4 hours after immersion when placed in a saline bath during a study conducted in rabbit skin [17]. As previously mentioned, skin is anisotropic *in vivo*. Lanir and Fung, however, found symmetry in mechanical properties with respect to two normal, or perpendicular, planes during mechanical testing. This means that skin is also orthotropic [17], which makes skin one of the simplest tissues for characterization of mechanical properties. Finally, the stress-strain relationship of skin is time-dependent, since soft tissues are pseudoelastic [17].

The previous chapter of this thesis validated the individual systems of the customized planar biaxial device. A validation of the integration of these systems, however, needs to be conducted via a soft tissue mechanics pilot study. Due to the abundant documentation and symmetry exhibited in skin mechanical properties, skin is an excellent choice of soft tissue for the purposes of this pilot study.

III. OBJECTIVE

The objective of this chapter is to characterize the mechanical properties of murine skin to validate the planar biaxial device.

IV. METHODS

IV.1 Validation of Individual Systems of the Planar Biaxial Device

Capabilities of the individual hardware and software components of the planar biaxial device were validated. Validation was done in three phases: motion controls, data acquisition, and image acquisition.

IV.1.1 Motion Control

Motion control hardware and software was validated by moving individual motors, pairs of motors, and all motors 25.4 mm (1 inch) in out of tank, and then 25.4 mm in into the tank. Calipers with an accuracy of 0.01 mm were used to measure movement. Bird's eye view photos were taken before and after each movement. This verified that the LabVIEW program was sending the correct commands to the stepper motor controllers, and the stepper motors were responding properly to commands from the stepper motor.

IV.1.2 Data Acquisition (DAQ)

Data acquisition hardware and software was validated through a calibration. A detailed calibration protocol can be found in Appendix I. Briefly, the load cells were subjected to increasing and then decreasing weight increments of approximately 0.5 pounds up to approximately 4 pounds and back down to 0 pounds. Voltage data is collected in excel, and an equation is formulated to convert output voltages to known loads.

IV.1.3 Image Acquisition (IMAQ)

A murine skin sample, approximately 5mm x 5mm, was cut into a cruciform shape, gripped, and placed into the device. Prior to gripping and placement, activated charcoal was used to create four dots in the center of the sample. Once the LabVIEW image acquisition code started to run, the lens of the camera and the light source were used to take an image where the four dots, or particles, were the most prevalent aspect of the picture. The image was saved. Then, a threshold was set which only included the pixels that

represented the particles. Once the threshold was set, a live feed appeared showing calculated distances between each particle at each particle's respective center of mass. The skin sample was moved 0.5 mm out of the tank and then 0.5 mm into the tank to verify that the IMAQ code still followed the four particles and updated the distances and center of mass for each particle.

IV.2 Murine Skin Pilot Study

IV.2.1 Sample Preparation

Three murine abdominal skin samples were dissected. Fur was removed from the skin samples with Nair. The bare skin samples were then hydrated with Hank's Balanced Saline Solution (HBSS) and placed in a freezer at -20°C until biomechanical testing. Skin samples were thawed prior to testing, and cut into a cruciform shape using a stamp, with a 5mm x 5mm square center and 5mm x 5mm arms on each side of the center square. This is done to achieve a desirable aspect ratio and reduce the effects of St. Venant's principle. Tabs of sandpaper were glued to the edges of each arm of the cruciform sample using cyanoacrylate. The sample was placed in custom-made grips and into the planar biaxial device. After securing the tissue sample into the device, four dots of activated charcoal were placed in the center square of the sample for strain tracking purposes. The testing chamber was filled with HBSS.

IV.2.2 Biomechanical Testing

A strain-controlled biomechanical testing protocol was used via a combination of optical strain tracking and grip to grip strain tracking. First, a preload of approximately 1 gram was applied to the tissue sample to establish a reference configuration for both axes. The skin sample was then preconditioned with 6 equibiaxial cycles to 5% optical strain at 0.5% per second. After preconditioning, the sample was pulled equibiaxially to



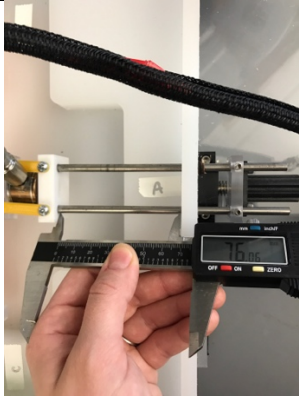
approximately 2-4 mm of displacement, grip to grip at 0.01 mm per second. Load displacement and stress strain curves were then compared to data found in literature [34, 36]. Young's Modulus was quantified from stress strain data and compared to data in literature [36]. A custom MATLAB script was written to approximate the Young's Modulus of data in literature.

V. RESULTS

V.1 Validation of Motion Control

Motion control hardware and software was verified within roughly 1% of the indicated distances. Each individual motor moved 25.4 mm in tension and compression. The motor pairs associated with the x- and y-axis also moved 25.4 mm in tension and compression. Finally, all motors moved 25.4 mm in tension and compression together. A representative sample of bird's eye view pictures taken during the motion control validation can be seen in Table 1. The other pictures can be found in Appendix H.

Table 1: Representative sample of pictures taken during motion control validation (Motor A)

Before	After 25.4 mm Tension	After 25.4 mm Compression
 <p><i>76.04 mm</i></p>	 <p><i>50.85 mm 0.82% error</i></p>	 <p><i>76.06 mm 0.75% error</i></p>

V.2 Validation of Data Acquisition (DAQ)

Data acquisition hardware and software was successfully verified via a calibration.

Voltage outputs are accurately converted to a load in grams. A representative graph of the load cell calibration voltage outputs versus loads can be seen in Figure 9 below.

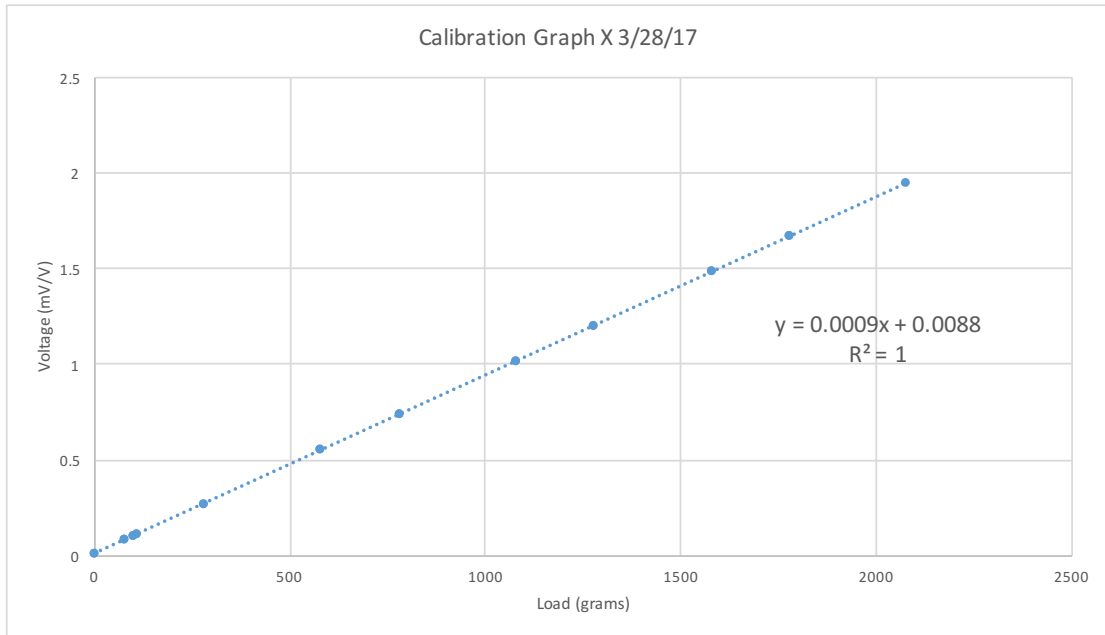


Figure 9: Representative Load Cell Calibration Graph. Known loads are applied to the load cells to generate a voltage output.

V.3 Validation of Image Acquisition (IMAQ)

Image acquisition hardware and software was verified. Screenshots were taken of LabVIEW code before tissue sample was moved, after the tissue sample was moved 0.5 mm in tension, and after the tissue sample was moved 0.5 mm into the tank. The calculated distances over-laid on the thresholded image update in real time. The images taken during this validation are shown in Figure 10 below.

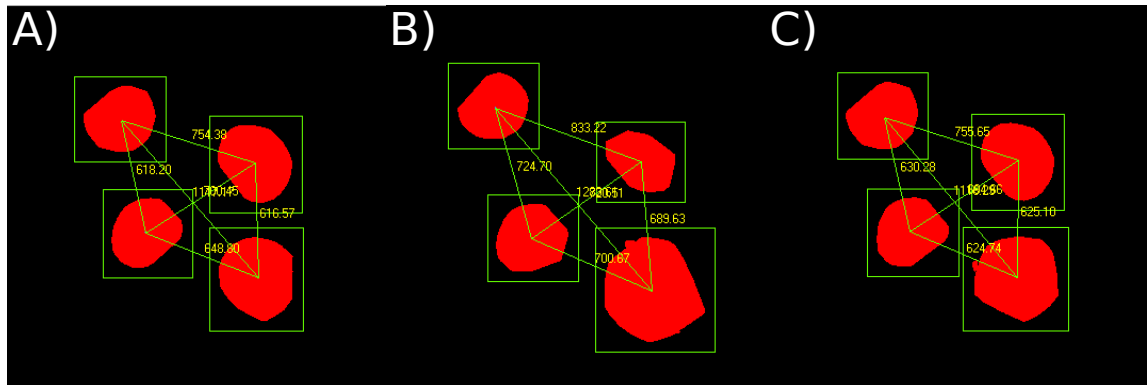


Figure 10: Screenshots of LabVIEW Output During IMAQ Verification. A) Thresholded and Tracked Image Before Movement B) Thresholded and Tracked Image After 0.5 mm Movement in Tension. C) Thresholded and Tracked Image After 0.5 mm Movement in Compression.

V.2 Murine Skin Pilot Study Results

Load displacement curves, when superimposed against load displacement curves created by Groves, et. al [34], show that data from the planar biaxial device falls within the range of their data. Figure 11 shows a representative graph, with black open circles representing data points and the blue, yellow, and red symbols representing data points collected by Groves et. al. taken at 0, 45, and 90 degrees, respectively.

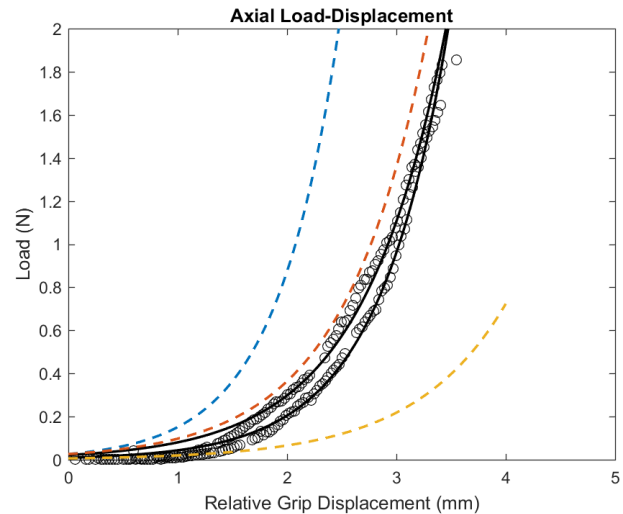


Figure 11: Representative Load Displacement Curve Superimposed Over Data from Groves, et. al. [34]. Black open circles represent experimental data points and line represents exponential curve fit to the data. Blue, yellow, and red symbols/lines represent measurements taken at 0, 45, and 90 degrees, respectively, by Groves, et. al.

Additionally, stress-strain curves of the data were created to calculate Young's Modulus. A representative stress-strain curve is shown in figure 12. Young's Modulus in the axial direction is 8.26 ± 1.58 , and 6.00 ± 2.31 in the circumferential direction.

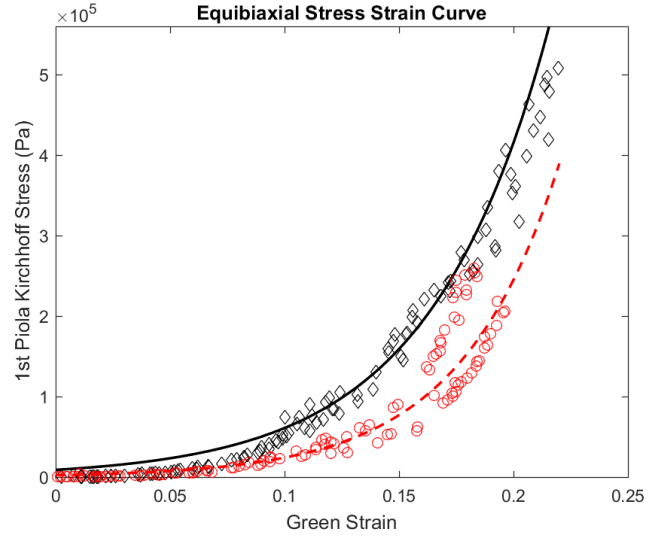


Figure 12: Representative Stress Strain Curve of Murine Skin Equibiaxial Data. The black curves and symbols represent the axial axis, while the red line and symbols represent the circumferential axis.

A table of experimental Young's Modulus values compared to data in literature can be found in Table 2 [36].

Table 2: Comparison of Young's Modulus Experimental Values vs. Literature Value

		Sample 1		Sample 2		Sample 3	
	<i>Munoz, et. al. 2008</i>	Axial	Circumferential	Axial	Circumferential	Axial	Circumferential
Young's Modulus (MPa)	8.10	7.89	5.62	9.99	8.48	6.90	3.90

VI. DISCUSSION

The individual systems of the planar biaxial device were successfully validated. Motion control of the input displacement system and hardware was validated through external measurements of an indicated distance of 25.4 mm (1 inch). All motors moved to the indicated distance within a 1% margin of error. Data acquisition hardware and software for the load cells was validated by the methodology described in Appendix I, which generated a linear equation to convert the voltage outputs of the load cells to a load in

grams. Image acquisition hardware and software was validated through successful tracking of particles during tissue movement. A reference position was established, then a tissue sample was moved 0.5mm in tension to see if the boxes around the particles followed them to their next position. After that, the tissue was returned to the reference position to confirm the boxes follow the particles during compressive movement.

A murine skin pilot study was conducted to validate the integration of all systems of the planar biaxial device. The pilot study showed that data produced by the device fell within literature values. Additionally, the data showed the nonlinear, anisotropic, and pseudoelastic behavior of skin as seen in the stress strain curve in figure 12. Validation was done qualitatively, through an overlay of experimental load displacement data to literature load displacement data, and quantitatively, through estimation and comparison of Young's Modulus. Load displacement curves from this pilot study fall within the range of load displacement curves generated by Groves, et. al. Young's Modulus approximated from Munoz, et. al.'s study [36] falls within the mean and standard deviation of both the axial and circumferential Young's Modulus.

Discrepancies in the data collected from the planar biaxial device can be attributed to a few factors. The first is biological variability between the tissue samples. For example, the third sample tested was more compliant than the first two tested, as shown by the stress strain curves and Young's Moduli. Additionally, the second tissue sample in our study was tearing during testing, and eventually ripped after testing was completed. This could explain the discrepancies within the experimental data set. The next factor that could contribute to discrepancies between data sets is differences in reference configuration. The tissue samples in this pilot study were brought to approximately a 1 gram load prior to

preconditioning, which could cause slight differences from literature data. Lastly, the Groves et. al. and Munoz et. al. studies were uniaxial tests, while data from this study was generated through biaxial tests. This would make the planar biaxial device data stiffer, in general, due to consideration of axial coupling.

VII. CONCLUSION

To summarize, the planar biaxial device was successfully validated through a murine skin pilot study. Results showed that the collected data both quantitatively and qualitatively falls within a reasonable range of values in literature. Now that the planar biaxial device is externally validated, studies in other soft tissues can begin.

Chapter 4: FUTURE DIRECTIONS

The work of this thesis resulted in a custom planar biaxial mechanical testing device that can be used to test a variety of soft biological tissues. The following sections outline extensive research and work done to develop future experiments, which include expanding the current knowledge of a tissue engineered NAC, the role of the uterosacral ligament in pelvic floor disorders, age-specific healing in the murine patellar tendon, and background research on preterm birth and sex differences in rotator cuff tendons.

I. CHARACTERIZATION OF A TISSUE-ENGINEERED NIPPLE-AREOLAR COMPLEX VIA PLANAR BIAXIAL MECHANICAL TESTING

I.1 Introduction

Breast cancer is the most commonly diagnosed cancer among women (excluding skin cancer) with approximately 226,000 new cases every year in the United States [37]. Mastectomies, the process in which breast tissue is removed, are often performed to remove the cancer. During a total mastectomy, the nipple-areolar complex is also removed. Many women opt to have breast reconstruction surgery done after a mastectomy. One important aspect of breast reconstruction surgery is replacement of the nipple-areolar complex (NAC). Current interventions for the NAC are very limited and provide variable results for breast cancer patients undergoing reconstruction surgery. Recently, Pashos et. al. [38] proposed a biocompatible NAC graft from intact decellularized human intact NAC as a viable alternative to available treatment options on the market. The mechanical properties of this tissue-engineered NAC, however, are unknown. Therefore, the objective of this

study will be to characterize the mechanical properties of the tissue-engineered NAC using the planar biaxial device.

I.2 Background

I.2.1 Function, Composition and Microstructure of Native Nipple-Areolar Complex

In women, the NAC's primary function is lactation, which is secretion of milk from mammary glands in the breast to nourish an infant. The NAC is comprised of areolar (sebaceous) glands, mammary glands, sensory nerve endings, smooth muscle, and a lymphatic system called the subareolar plexus [39]. The areolar glands produce oil to lubricate the NAC. Microstructurally, the NAC is primarily composed of collagen, elastin, smooth muscle, and GAGs [38].

I.2.2 Clinical Motivation - Biocompatible Nipple-Areolar Complex Graft via Decellularization

The American Cancer Society estimated about 226,870 new cases of invasive breast cancer in U.S women, and about 39,510 deaths from breast cancer in 2012 [37]. Approximately 36% of women with early stage breast cancer and 60% of women with late stage breast cancer opt for a mastectomy rather than breast-conserving surgery [40]. An important psychological aspect of a mastectomy for patients is replacing the NAC. Current options for NAC replacement, however, are limited to the creation of NAC from existing tissue, secondary grafting, and tattoos [41. 42]. Therefore, there is a need for a reconstruction option of the NAC for breast reconstruction surgeries.

Pashos et. al. [38] recently describes a tissue-engineering approach for NAC reconstruction using rhesus macaque NAC (*Macaca mulatta*). Briefly, the NAC is removed from the patient and undergoes decellularization, which strips a tissue of its cells and leaves the extracellular matrix (ECM) intact. The NAC graft is now considered to be acellular and

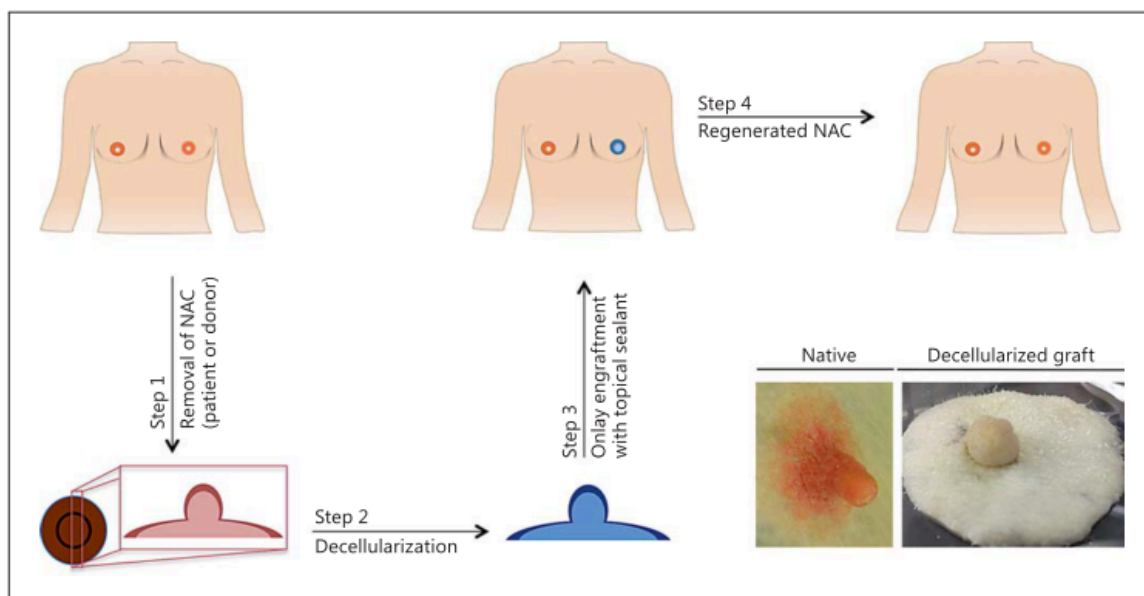


Figure 13: Schematic of the decellularization and engraftment process of the NAC courtesy of [38]. Step 1 depicts the collection of the NAC from either the patient, who will then receive their own regenerated NAC, or a donor. Step 2 represents the decellularization of the NAC graft with detergents, salts, and enzyme. Step 3 depicts the onlay engraftment of the acellular NAC. Step 4 allows for the patient's own cells to migrate into the acellular NAC graft. Representative images of native and decellularized rhesus NAC are also provided. Figure from [40]

is grafted back to the recipient. Finally, the patient's own cells move towards the acellular NAC and regenerate its original cellular structure. Figure 8 shows a schematic of this process (courtesy of Pashos, et. al. 2017 [Pashos]).

Characterization of the decellularization of NAC tissue and comparison to native NACs with respect to structural protein composition, lubrication protein retention, the maintenance of adhesion molecules, and bioactivity when reseeded with cells via histological and quantitative analysis was successful [Pashos]. While this study provided foundational information for this technique, further studies, such as a mechanical evaluation, need to be conducted before this technique reaches clinical trials. One metric

of success for this tissue-engineered NAC is its ability to closely mimic the mechanical properties of the native NAC.

I.3 Protocol Development

I.3.1 Sample Preparation

All animal protocols were approved by the Institutional Animal Care and Use Committee (IACUC) of the Tulane National Primate Research Center (TNPRC). All animal procedures follow the requirements of the Animal Welfare Act. 10 tissue-engineered NACs will be prepared via the techniques described by Pashos [Pashos]. Briefly, NACs will be collected from rhesus macaque (*Macaca mulatta*) males and females from 1-13 years of age. The NACs will be decellularized and frozen until biomechanical testing. NAC samples will be prepared for biomechanical testing in the same manner as skin, previously described in chapter three.

I.3.2 Biomechanical Testing

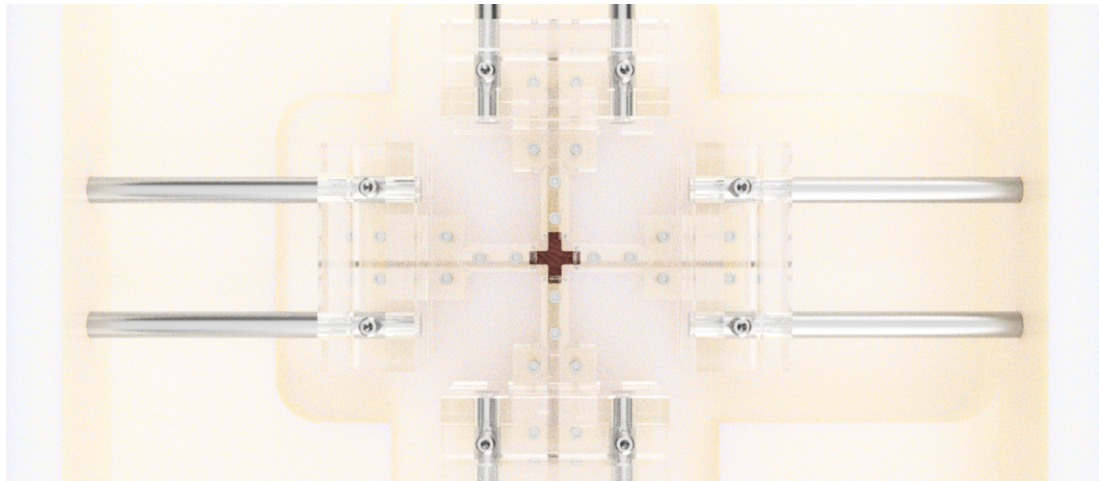


Figure 14: Three-Dimensional Model of a Cruciform Tissue Sample Gripped in the Planar Biaxial Device. Courtesy of Cody O'Cain.

The biomechanical testing protocol to be used in this study is a modified version of a previously described protocol [43]. Briefly, a strain-controlled biomechanical testing

protocol was used via optical strain tracking. Skin samples were preconditioned equibiaxially 5 cycles to 2% strain. A cycle of three protocols were run: Y-direction biaxial stretch, equibiaxial, and X-direction biaxial stretch. Each of these protocols will pull the decellularized NAC tissue to a maximum strain of 10% at a strain rate of 0.5% per second.

I.4 Discussion

Recently, Pashos et. al. [38] developed a tissue engineered NAC via decellularization for potential use as an NAC replacement for breast reconstruction surgery. The mechanical properties of the tissue-engineered NAC, however, has yet to be characterized. Therefore, the planar biaxial device can be utilized to elucidate its mechanical properties. Sample preparation and biomechanical testing protocols developed during the murine skin pilot study will be employed for the characterization of tissue-engineered NAC mechanical properties. Appropriate experimental parameters for the NAC will be determined via pilot studies. Results from this study will provide early insights into the mechanical behavior of the tissue-engineered NAC. Ultimately, this information will be used to determine if the tissue-engineered NAC is a viable treatment option for breast cancer patients undergoing total mastectomies and breast reconstruction surgeries. This tissue-engineered NAC has the potential to impact the lives of many women affected by breast cancer.

II. TOWARDS AN INVESTIGATION OF THE MECHNAICAL PROPERTIES OF PELVIC ORGANS AND SUPPORTING STRUCTURES IN RELATION TO PELVIC ORGAN PROLAPSE

II.1 Introduction

Pelvic floor disorders, such as pelvic organ prolapse (POP), urinary incontinence, and fecal incontinence, have physical and psychological effects on many women [44-49]. It is estimated that 41.1% of all women have some form of pelvic organ prolapse and that 11% of all women require surgery for it [50]. Of those requiring surgery, it is suggested that almost 30% require a repeat operation [51]. Despite this high incidence rate, little is known about the underlying pathology. There is, however, a well-established link between dysfunction in connective tissue metabolism within the vagina and supporting uterosacral ligaments [52, 53]. Multi-parity and aging have been suggested as key risk factors, with an eleven-fold increase in risk for a parity of four or more [54] and by 10% for each decade of life [55]. Additionally, studies have shown that women with prolapse demonstrate an up-regulation of enzymes that degrade collagen and elastin, especially matrix metalloproteinases (MMP) in the vagina [56-58]. Thus, there exists a need to rigorously quantify the dynamic structure-function relationships of the vagina and uterosacral ligament (USL), including the mechanical contribution of the load-bearing constituents (e.g. fibrillar collagen, elastin, smooth muscle, glycosaminoglycans) as a function of age.

Past studies have primarily relied on uniaxial testing of the vagina to elucidate its mechanical properties [58-65]. While there are certain instances when uniaxial testing provides meaningful data, it fails to account for physiological boundary conditions of the vagina. Biaxial testing allows for more accurate quantification of mechanical properties due to proper consideration of physiological boundary conditions. Therefore, the objective of this study will be to characterize the mechanical properties of human vaginal and

uterosacral ligament tissues using planar biaxial mechanical testing. It is our preliminary hypothesis that a decrease in elastin with age will induce maladaptive remodeling in the vagina and its supportive structures, contributing to a decrease in vaginal and support ligament stiffness, leading to an increased prevalence of POP in the elderly population.

II.2 Background

II.2.1 Pelvic Floor Anatomy

The pelvic floor is formed by the pelvic diaphragm, which is a bowl-shaped tissue containing the levator ani and coccygeus muscles and the fascia that cover the superior and inferior surfaces of these muscles. The levator ani muscles, which are comprised of the pubococcygeus and the iliococcygeus muscles, primarily help support

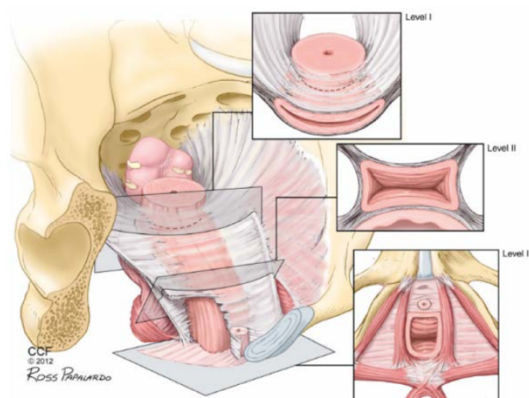


Figure 15: Diagram of the Pelvic Floor, Specifically Denoting the Three Levels of Support. These levels support the organs and connective tissues of the pelvic floor. Figure from [66].

pelvic viscera and resist increases to intra-abdominal pressure. The coccygeus muscle forms a small part of the pelvic diaphragm that supports pelvic viscera and flexes the coccyx [33].

The pelvic floor consists of the antero-inferior wall, two lateral walls, and a posterior wall. The antero-inferior wall is primarily comprised of the bodies and rami of the pubic bones and pubic symphysis, and bears some of the weight of the bladder. The lateral walls are padded by the obturator internus, which laterally rotates the hip joint and assists in holding the head of the femur in the acetabulum. Lastly, the posterior pelvic wall is formed by the sacrum, coccyx, the sacro-iliac joints and their respective ligaments, and

the piriformis muscle, which shares the same functions as the obturator internus but also abducts the hip joint [33].

II.2.1 Anatomy and Physiology of the Vagina

The vagina is a musculomembranous tube that extends from the fornix, which is directly inferior to the cervix and external os of the uterus, to the vestibule, which contains the external vaginal and urethral orifices. The vagina forms the inferior aspect of the birth canal and provides a canal for menstrual fluid. The vagina is regularly collapsed and its anterior and posterior walls are in contact. The vaginal wall is made up of four layers: the epithelium, the subepithelium, the muscularis, and the adventitia [44, 52, 56]. Support for the vaginal wall primarily comes from the subepithelium and the muscularis layers.

II.2.2 Composition and Microstructure of the Vaginal Wall

Collagen is the predominant structural constituent of the vagina (84%), with an intermediate amount of elastin (13%) [44]. Smooth muscle cells are also present [67]. The intermediate presence of elastin gives the vagina resilience, which allows the vagina to passively recoil after large deformations without a significant loss of energy [68]. Proteoglycans are also present in the vaginal wall [69].

II.2.3 Anatomy, Physiology, Composition and Microstructure of the Uterosacral Ligament

The uterosacral ligament (USL) is a supportive structure of the uterus, cervix, and vagina. It is a bilateral ligament that is connected from the superior vagina and cervix to the sacrum and lateral pelvic walls [70].

Connective tissues of the pelvic floor, such as the USL, are comprised mostly of collagens. They also contain small amounts of non-collagenous glycoproteins, elastin, hyaluronan (a GAG), and proteoglycans [44]. Vasculature and nerve fibers have been found in the USL [71]. Tensile strength of the pelvic floor connective tissues primarily

comes from type I collagen [72]. It has been shown that an increase in the presence of collagens type III and V are associated with a decrease in the mechanical integrity of the tissue [73]. Collagens III and V aid in limiting the diameter of the collagen fibrils.

II.2.4 Pelvic Floor Disorders

Compared to fields such as orthopaedics and cardiovascular biomechanics, the field of women's reproductive health is wildly understudied. As previously stated, applying biomechanics to medical research deepens our knowledge of homeostatic tissue function and improves our ability to predict tissue behavior, and design treatments for tissue pathology and injury. The health benefits of rigorous biomechanics research in the women's reproductive field are only recently being acknowledged. One of the most active areas of women's reproductive health biomechanics research is in pelvic floor disorders, specifically pelvic organ prolapse.

Pelvic organ prolapse is a disorder in which the pelvic support structures lose their mechanical integrity and allow for the downward descent of the female pelvic organs (uterus, bladder, small bowel, rectum), that may result in their protrusion through the vagina [25]. As shown in figure 16, the vagina lends mechanical support to the other pelvic organs, meaning it is constantly subjected to intra-abdominal pressures. When the vagina loses the ability to resist those pressures, the other pelvic organs can prolapse. POP is

estimated to affect 41% of all women and can cause a variety of symptoms to manifest, both physiological as well as psychological. These include urinary and bowel complications, sexual dysfunction, pain,

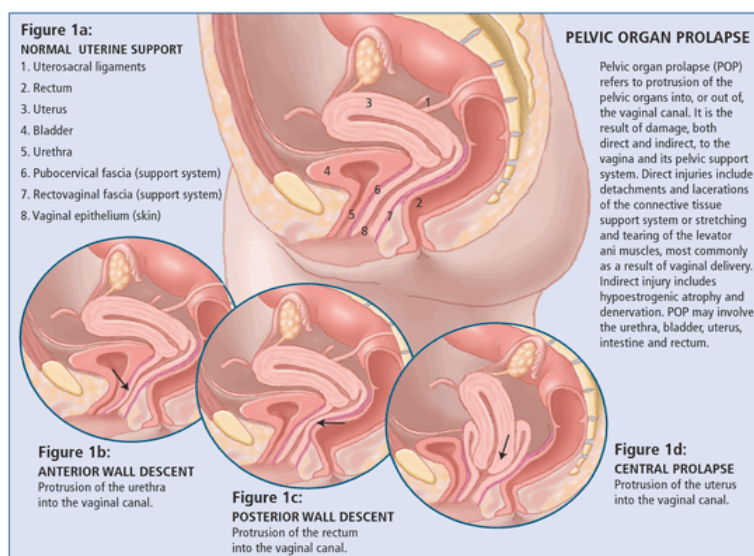


Figure 16: Example of Pelvic Organ Prolapse Progression, Courtesy of Web MD.

discomfort, poor self-image, physical activity limitations, and a reduced quality of life [49]. Approximately 11% of women require corrective surgery, leading to an annual direct cost of over 1 billion dollars [74]. In addition, the number of women seeking care for POP is predicted to double over the next 30 years with the foreseen increase in the elderly and obese population [75]. Current treatment options include non-surgical pelvic floor muscle training and pessary use, or surgical reconstructive or obliterative methods, respectively, and do not sufficiently alleviate the problem [76]. The most popular treatment option, vaginal meshes, may in some cases worsen the condition by further increasing the degeneration of the vaginal wall due to a compliance mismatch between the two materials. This may play a role in the 30% of women that require a repeat operation. Many patients develop POP between the ages of 50-70, meaning that without adequate treatment options many women could potentially be dealing with POP for 30-50% of their life [77]. Thus, with improved treatment and prevention methods lies an opportunity to save over 90,000 women from pelvic floor surgery [77], as well as drastically cut annual healthcare costs.

II.2.5 Previous Investigations of Uterosacral Ligament and Vaginal Mechanical Behavior in Relation to Pelvic Organ Prolapse

Recently, the biaxial mechanical properties of the USL have been investigated [70, 71, 78]. In general, connective tissues of the pelvic floor undergo large strains, are orthotropic, and stiffer in the main physiological loading direction [78]. Compared to the cardinal ligament (CL), another connective tissue that supports the pelvic floor, the USL is stronger than the CL. This is supported by the USL's statistically higher ultimate stress and tangent modulus in the linear region of its stress-strain curve [71]. Additionally, the USL exhibits creep behavior in the *in vivo* loading direction, as well as the direction perpendicular to it [70]. These studies, however, were conducted in pigs. Conducting biaxial mechanical tests with human tissues rather than an animal model can increase our understanding of the mechanical behavior in the human body.

As of 2002, investigations of the mechanical properties of the vagina had not been conducted [59]. Since then, there have been attempts to quantify the mechanical properties of the vagina, but have reported conflicting results [59-61, 79-82]. Differences in results, however, can be attributed to tissue collection at different sites along the vaginal wall. Others have tried to replicate physiologically relevant conditions by using rings [62] or by mechanically testing the entire vagina [63]. One study left the vaginal support structures, including its insertion and attachment points, intact [64]. While this is the most physiologically relevant way to elucidate the mechanical properties of the vagina, it makes identifying the roles of load-bearing constituents more difficult. In addition, each of these studies attempted to quantify mechanical properties via uniaxial testing, which fails to account for the physiologic environment of the vagina.

II.3 Experimental and Protocol Developments

II.3.1 Experimental Design

45 human samples will be collected. The samples will be mechanically tested on a planar biaxial device. Quantitative microstructural analyses will be performed to determine vaginal and uterosacral ligament structure-function relationships. The mechanical contribution of elastin is thought to play a role in POP progression [83-86]. Therefore, the mechanical properties of the samples will also be assessed after enzymatic digestion of elastin. Table 3 below describes the inclusion and exclusion criteria for collected samples, which will be placed in either the control or prolapse group. T-tests will be used to determine statistical differences in the mechanical properties between the control and prolapse groups.

Table 3: Overview of Uterosacral Ligament and Vagina Mechanical Testing in Relation to Pelvic Organ Prolapse Experimental Course

N	Group	Inclusion Criteria	Exclusion Criteria
22-23	Control	Female, ≥ 18 years old, no symptoms or evidence of prolapse, undergoing hysterectomy	Male, cancerous tissue, connective tissue disorder, < 18 years old, symptomatic prolapse at least stage 2 in one compartment, previous surgery for pelvic floor disorder
22-23	Prolapse	Female, ≥ 18 years old, symptomatic prolapse at least stage 2 in one compartment, undergoing hysterectomy	Male, cancerous tissue, connective tissue disorder, < 18 years old, previous surgery for pelvic floor disorder

II.3.2 Sample Collection and Preparation

Vaginal and uterosacral ligament samples, at least 10mm x 10mm, will be acquired via the Ochsner BioBank after routine gynecological procedures. These procedures will be supervised by our Ochsner clinical collaborators, Drs. Leise Knoepp and Laurephile Desrosiers. Samples will be taken from the distal uterosacral ligaments and vagina and

frozen in Hank's Balanced Saline Solution (HBSS) at -80°C . Prior to being frozen, the samples will be oriented and marked.

II.3.3 Biomechanical Testing

Before mechanical testing, the samples will be thawed for approximately 9 hours at room temperature in HBSS solution. The samples will be stamped into a cruciform shape to minimize St. Venant's effect. Excess tissue from the corners will be used as control

samples (before elastase digestion) for histology. The four arms of the cruciform will have sandpaper tabs glued to each side with cyanoacrylate. Four dots of activated charcoal will be placed

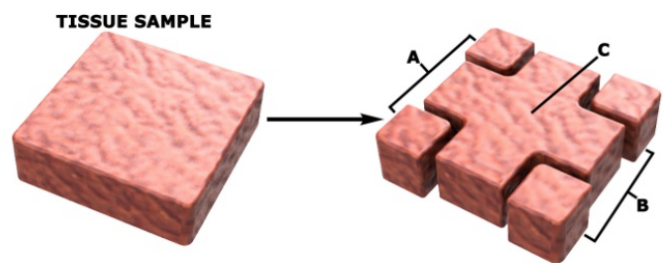


Figure 17: Vaginal and USL samples will be stamped into a cruciform shape for biomechanical testing (C). Excess tissue will be used from control histological (A) and biochemical (B) assays. Courtesy of Cody O'Cain.

on the sample for optical strain tracking. Samples will be subjected to strain-controlled mechanical tests, as previously described in chapter three. The samples will undergo 9 cycles of equibiaxial preconditioning. Then, as previously described in chapter three, a cycle of three protocols will be run: Y-direction biaxial stretch, equibiaxial, and X-direction biaxial stretch. Each protocol will pull the tissue to a set percentage strain and at a strain rate to be determined in pilot studies. After the mechanical test protocols are complete, the sample will undergo enzymatic digestion of elastin via pancreatic elastase. The mechanical assessment will be repeated on the sample after it re-equilibrates in HBSS [87-91].

II.3.4 Histology

Pre- and post-elastase samples will be analyzed using the Tulane Histology Core Facility. Samples will be paraffin embedded and stained with Picrosirius Red, Movat's Pentachrome, and Verhoeff-van Gieson, which will quantify collagen, glycosaminoglycans/smooth muscle, and elastin, respectively. Previous investigations have used image

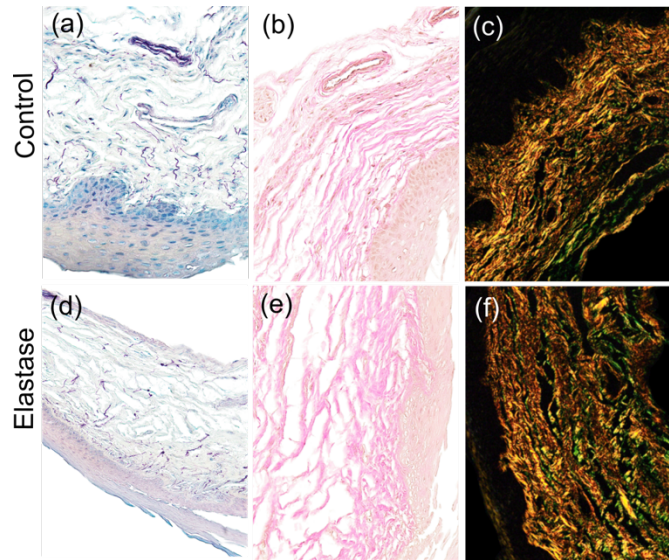


Figure 18: Murine vaginal tissue before and after enzymatic digestion of elastin stained with Movat's Pentachrome (A,D), Verhoeff-van Gieson (B,E), and Picrosirius Red (C,F). Decreased presence of elastin can post-digestion can be observed in (D,E). Courtesy of Jason Schuster.

analysis programs to quantify the area fraction of each constituent [92-94], the organization and undulation of collagen [95, 96], and tortuosity of elastic fibers [97].

II.4 Discussion

This chapter describes experimental and protocol developments for an investigation of the mechanical properties of the uterosacral ligament and vagina and their relation to pelvic organ prolapse. An experimental design was created that included control and prolapse groups and describes the inclusion and exclusion criteria for patients from which samples will be taken. Preparation of the sample was outlined. A preliminary biomechanical testing protocol was described. This protocol has been implemented in previous chapters of this thesis for murine skin. Pilot studies will need to be conducted to determine specifics of this protocol, such as the maximum strain percentage and the strain rate for which the tissue will be pulled. This biomechanical testing protocol will be run on all intact tissue, and then again on the same tissue samples post-subjection to enzymatic

digestion of elastin, which is thought to play a role in the stability of pelvic organs. Lastly, a histology protocol was developed.

It is our hypothesis that uterosacral ligament and vaginal tissues will exhibit more compliance before elastin digestion. In the case that the hypothesis is disproven, other metrics (i.e. histology) will ensure determination of the structure-function relationships of vaginal and uterosacral ligament. Additionally, we posit that an increase in risk factors of POP will correlate with a decrease in elastin. This second hypothesis will be examined via mathematical models and statistical methods, a future direction of the work laid down in this chapter. This study will influence clinical treatment interventions of POP via a better understanding of the relationship between key risk factors and the microstructural constituents that cause structural instability in the pelvic organs.

III. EXAMINATION OF THE MECHANICAL PROPERTIES OF THE UTERUS AND CERVIX IN RELATION TO PRETERM BIRTH

Babies born preterm, which is defined as more than three weeks early, are at a higher risk for numerous problems, such as infant mortality, respiratory complications, infections, extended stays in the neonatal intensive care unit, and delays in development [98-100]. Additionally, long-term they could be at risk for heart-disease and diabetes [101]. Despite advancements in modern medicine, preterm births are rising in the developed world [102]. Furthermore, preterm births cost the healthcare industry approximately \$26.2 billion dollars annually [103]. It is thought that suboptimal remodeling of the uterus and/or the uterine cervix during pregnancy plays a role in the time at which a baby is delivered [104].

Uterocervical adaptations during pregnancy is poorly understood. Therefore, there is a need to identify the mechanisms of uterocervical adaptation to design patient-specific

clinical interventions to prevent maladaptive remodeling and ultimately reduce infant mortality. Therefore, the objective of this study would be to characterize the mechanical properties of uterocervical tissue to identify key mechanisms of uterocervical adaption during different pregnancy time-points. Planar biaxial mechanical testing and histology could be utilized to quantify mechanical properties (planar biaxial testing) as well as the amount and organization of structurally-significant constituents (histology) present at different time points throughout pregnancy.

IV. FOUNDATIONAL DEVELOPMENTS FOR AN ANALYSIS OF AGE-SPECIFIC TENDINOPATHY AND HEALING IN THE MURINE PATELLAR TENDON

IV.1 Introduction

Tendinopathy, or tendon pain in combination with reduced function of the tendon, [105, 106] is a type of injury fundamentally rooted in soft tissue mechanics. Observations of patellar (knee-cap) tendon injury rates suggest the incidence of injury increases in elderly individuals [107, 108]. It is known that patellar tendinopathy is associated with degenerative changes in the extracellular matrix proteins. There is a lack of understanding, however, of how the extracellular matrix proteins are organized and how this dictates the loss of integrity seen throughout the aging process. Hence, there is a need to better understand the relationship between patellar tendon extracellular matrix components and mechanical properties to understand and design treatments to prevent injury due to aging.

Further, tendons possess limited healing capability and there is a lack of understanding as to why the mechanical properties of tendons do not return to pre-injury values. The healing potential of tendon is also thought to decrease with age, limiting mobility in the elderly population. The role of each extracellular matrix protein in tendon healing, and age-dependent lack of healing, is not well understood. Hence, there is a need

to better understand the link between mechanical properties and microstructure during age-specific tendon healing.

This study will evaluate the correlation between proteins and patellar tendon mechanical function during injury and healing at different stages of life of adult female and male mice using the planar biaxial device. The results of this study will enable scientists to better understand the relationship between structure (amount and organization of each protein) and function (mechanical properties) of the patellar tendon to gain valuable insights into tendon healing. It is our hypothesis that age-related tendon changes include loss of elastic fiber integrity, decreased collagen organization, and increased collagen crosslinks. We posit that these changes correlate with reduced mechanical integrity. Additionally, we hypothesize the healing potential of tendons decreases with age. Hence, following injury, the production of collagen decreases with increasing age at the time of injury, consequently resulting in decreased tendon mechanical integrity.

IV.2. BACKGROUND

IV.2.1 Anatomy and Physiology of the Knee

The knee is the joint that connects the femur to the tibia and fibula. The patella, or the knee cap, is a large, triangular sesamoid bone. The anterior surface of the patella is convex, and its thick superior border slopes infero-anteriorly. The lateral and medial borders of the patella merge to form the apex. The posterior surface of the patella, which articulates with the femur, is smooth with a thick layer of articular cartilage. The patellar

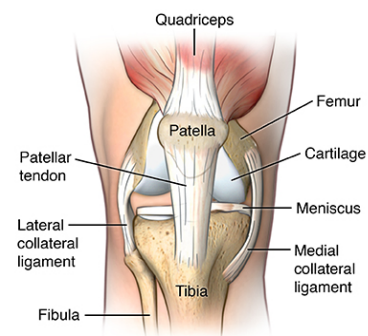


Figure 19: The patellar tendon is the final connection of the extensor mechanisms of the knee. Image courtesy of St Luke's Health System.

tendon extends from the quadriceps tendon from the patella to the tuberosity of the tibia. [33].

The primary muscles (and their respective tendons) involved in the knee are the quadriceps muscles: rectus femoris, vastus lateralis, vastus intermedius, and vastus medialis. Their main function is to extend the knee joint. The primary ligaments of the knee are the anterior cruciate ligament (ACL), the posterior cruciate ligament (PCL), and the fibular/tibial collateral ligaments. They are the ligaments that connect the femur to the fibula (ACL, PCL, and fibular collateral ligament) and to the tibia (tibial collateral ligament) [33, 109].

IV.2.2 Tendon Composition and Microstructure

Tendons are a connective tissue that connects muscle to bone. Their functions include transmitting force from muscle to bone (and vice versa), absorbing impacts and stresses, aiding in smooth joint movement, and preventing large displacements within the body. Tendons provide stability to the musculoskeletal system due to the long half-life of its main structural constituent, collagen (300-500 days).

Connective tissues primarily consist of the following three constituents: solid proteins, cellular components such as axons and fibroblasts, and water (55-70% of wet

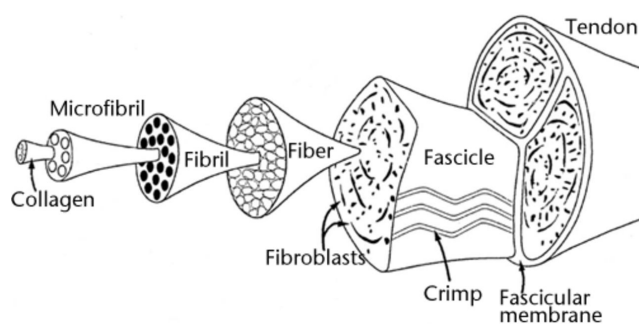


Figure 20: Hierarchical Structure of Tendons. Figure from [110].

weight). The solid proteins that make up tendons are elastin, proteoglycans, and type I fibrillar collagen. Elastin is responsible for the elasticity of the tissue under loading and makes up less than three percent of a tendon's dry weight. Proteoglycans are the next constituent and are responsible for attracting water to the tissue due to their overall negative

charge. Glycosaminoglycan (GAGs) chains are covalently bonded to the core protein of proteoglycans and are the reason for the high polarity of proteoglycans. Finally, collagen is the main structural component of tendon and makes up 60-85% of the dry weight. Collagen has a “crimp” or “waveform” structure that is responsible for the toe region for the stress-strain behavior of collagenous tissues.

IV.2.3 Age-Specific Patellar Tendinopathy

An increase in patellar tendon injury rates can be seen in elderly individuals [107, 108]. 54% of people over the age of 65 and 29% of people over the age of 75 saw an increase in sports-related injuries between the years of 1990 and 1996 [108]. Patellar tendinopathy is correlated with degenerative changes in extracellular matrix proteins, reduced tensile strength, and an affinity towards poor healing [111, 112]. Specifically, an increase of GAGs and type III fibrillar collagen and a decrease in type I collagen was observed [111, 112]. This suggests that altered matrix metabolism and mechanical loading are factors of age-related patellar tendinopathy [111]. Hence, there is a need for the identification of important mechanical and biological mechanisms of tendon healing to better understand the increased incidence of injuries among the elderly population.

IV.3 Experimental and Protocol Developments

IV.3.1 Experimental Design and Course

C57/BL/6 male mice will be purchased from Jackson Laboratories at 105, 255, and 525 days and randomly allocated to the experimental groups (control, 3 weeks, and 6 weeks). Following acclimation, randomly selected animals will undergo survival surgery (patellar tendon biopsy punch) at 120, 270, and 540 days old (age groups named Mature, Aging, and Aged, respectively) to simulate injury. Control animals will not undergo the patellar tendon biopsy punch surgery. Animals will then be euthanized 3 and 6 weeks

following injury within each age group. Control samples within each age group will be euthanized at 4.5 weeks following the injury time point (150, 300, 570 days old) to split the difference between injury groups, thus minimizing unnecessary animal euthanasia. Following euthanasia, a right or left hindlimb will be randomly allocated for biomechanical testing (10 biological replicates needed, hence with safety factor requesting 11 animals). The contralateral limb will be used for biochemical/histologic analysis (5 biological replicates each) following removal. Concurrently with the male mice experimental course, C57/BL/6 female mice will be requested per control group for a new assay, RNA sequencing, and biochemical analysis (5 biological replicates per age group). Similar to the male mice control group, they will not undergo the patellar tendon biopsy punch surgery.

Table 4: Overview of Age-Specific Murine Patellar Tendinopathy Experimental Course

Group		Acquired at age	Age at Injury	3wk post-injury	Control euthanasia	6wk post-injury
Mature ~120d	Age (days)	105	120	140	150	160
	Control	Male N=11 Female N=5				
	Injury	Male N=11				Male N=11
Aging ~270d	Age (days)	255	270	290	300	310
	Control	Male N=11 Female N=5				
	Injury	Male N=11				Male N=11
Aged ~540d	Age (days)	525	540	560	570	580
	Control	Male N=11 Female N=5				
	Injury	Male N=11				Male N=11

IV.3.2 Patellar Tendon Biopsy Punch

Except for control animals and the small cohort of female mice, the mice will first undergo a patellar tendon biopsy punch surgery. The purpose of this surgery is to simulate an injury to the patellar tendon. A protocol for the patellar tendon biopsy punch surgery was established. The mice will be anesthetized and their hind limbs shaved. With the knee in a flexed position, an incision in the skin medial to the knee will be made. It will be

moved aside to expose the patellar tendon. Two cuts parallel to the patellar tendon will be made. A plastic blade will be placed underneath the tendon to serve as a support for a 0.75 mm diameter biopsy punch. This will create a full thickness partial transection. The skin will be closed with a 4-0 prolene suture. This process will be conducted on the left and right leg. A full description of this protocol can be found in Appendix N [113].

IV.3.3 Patellar Tendon Dissection

After the animals in the experimental groups recover and heal for either 3 or 6 weeks post-surgery, they will be euthanized. Control animals will be euthanized at 4.5 weeks after the injury time point to minimize unnecessary animal euthanasia. Next, both the right and left hindlimbs will be dissected and allocated for biomechanical testing and biochemical/histologic analysis. A dissection protocol for the murine patellar tendon was practiced, refined, and established. The hind leg is first skinned from the ankle to pass the hip. Follow the quadriceps to cut away the hind leg. This will remove the femoral head from its socket. Begin to cut away muscle, beginning at the Achilles tendon, from the posterior side of the shank and the femur. Next, cut away muscle on the sides of the femur. Position the leg anteriorly and cut the quadriceps away from the femur until the femoral condyles are exposed. Use the scalpel to cut away the femur. Identify the patella and the patellar tendon, and cut away the quadriceps. Carefully remove tissue around the patellar tendon and its insertion into the tibia. Lastly, cut the tibia at the tibial tuberosity. A full description and list of materials for this protocol can be found in Appendix L.

IV.3.4 Biomechanical Testing

Characterization of the mechanical properties of the normal and previously injured murine patellar tendon at different time points throughout the murine lifespan via biomechanical testing will take place. Two important developments for this component of

the experimental design are selection of an appropriate gripping method for the tendon during testing and the biomechanical testing protocol.

IV.3.4.1 Patellar Tendon Grip Research and Design

In the literature, four different gripping methods are described. One way requires careful removal of the surrounding tissues and to detach the tendon as close to its insertion site as possible. The tendon fibers at the very end of the tendon are fanned out and gripped between two pieces of metal [114]. Not only is this method time consuming, but it also does not grip the tendon well. The second method is a modification of the first. Instead of cutting the tendon at the insertion site, the cut is made so that the tendon-bone complex is intact. The bone is then covered in a bone-glue composite and crushed together within sand paper [114, 115]. This creates a flat area to grip between two pieces of metal. The local mechanical properties, however, are changed using this method of gripping. The third method, like the second, leaves the tendon-bone complex intact. Instead of crushing the bone, however, the bone is placed in a pot of polymethylmethacrylate (PMMA) [10-12, 116-119]. This is the best-case scenario for local mechanics, since they are not changed. The bone is left intact, rather than being crushed like it is in the second method. Keeping it the bone intact preserves as much of the local, *in vivo* mechanics of the patellar tendon as possible in an *ex vivo* testing environment. It is difficult, however, to keep the tendon in the same plane. If the tendon is not in the same plane, torsion is introduced to the sample. Finally, the fourth method involves a conical funnel that allows the tendon to pass through, but not the bone [10-12, 114, 116, 118, 119]. This holds the bone steady without changing the local properties of the tissue.

Since the planar biaxial device is custom made and grips were already designed and manufactured, patellar tendon grip design was somewhat restricted. After careful

consideration, a decision was made to combine aspects of the third and fourth methods. Modifications to the load cell holders are currently in progress to incorporate the PMMA pot for the bone. The conical method previously mentioned was incorporated into the current grip design to be manufactured by Precision Cutting, LLC [Pineville, LA]. Modifications were made based on averages of measurements taken on dissected murine patellar tendon-bone complexes. Details on the calculation of these measurements, as well as a drawing of the modified grip for the patellar tendon, can be found in Appendix G2.

IV.3.4.2 Biomechanical Testing Protocol

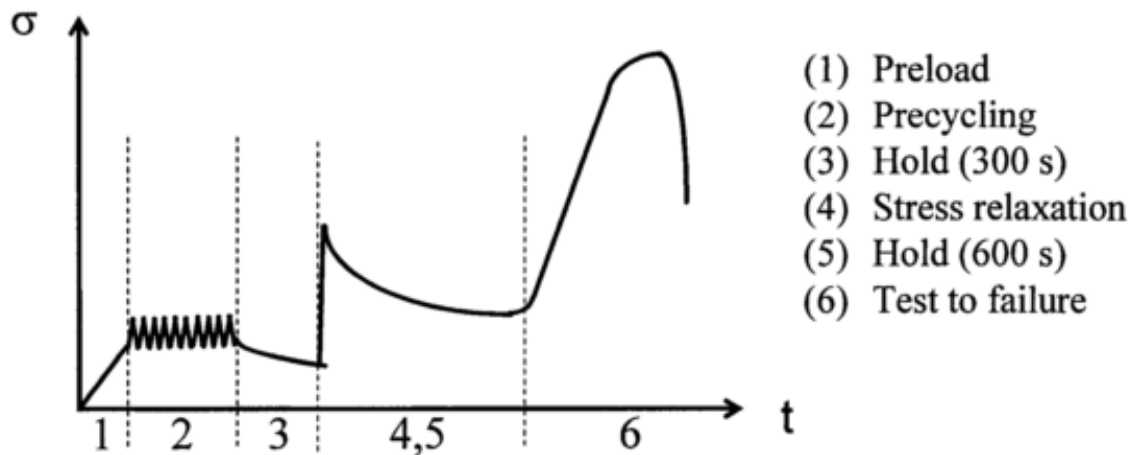


Figure 21: Graphical Representation of the Patellar Tendon Biomechanical Testing Protocol. Figure from [119].

The mechanical testing protocol described by [10] from which mechanical data was acquired in female mice from prior studies [9-12], will be employed. Following euthanasia, the patella-tendon-tibia complex will be explanted, gripped, and placed in a custom mechanical tests apparatus.

Patella-patellar tendon-tibia complexes will undergo a small tare-load, followed by preconditioning, a stress relaxation test, and a quasi-static ramp-to-failure. Specimens will be speckle coated to allow for optical strain tracking via a digital camera throughout the duration of the mechanical test. Following mechanical testing, material parameters of each

tendon will be analyzed via a nonlinear regression scheme and linearized stiffness of the estimated in vivo value of axial deformation will be calculated.

IV.3.5 Histomorphologic and Biochemical Analysis

Histologic samples will be immediately fixed in formalin, treated with Immunocal, paraffin embedded, and sectioned in 7 μ m sections. Sections will be stained with Hematoxylin and Eosin (H&E), Picrosirius Red, and Movat's Pentachrome. H&E images will be evaluated by three blinded graders for cellularity and cell shape. A custom MATLAB (Mathworks, Natick, MA) will be used to quantify the mass fraction of each matrix component from Picrosirius Red and Movat's images. Biochemical samples will be immediately flash frozen in liquid nitrogen and protein content will be assessed via manufacturer's instructions (Biocolor: collagen, GAG, elastin).

IV.3.6 RNA Sequencing Analysis

Samples denoted for RNA-sequencing will be immediately flash frozen upon excision and transferred to the COBRE Genomics and Biostatistics Core for RNA analysis and sequencing isolation.

IV.4 Discussion

The foundations of a study in age-related patellar tendon healing were laid down. A protocol for a patellar tendon biopsy punch surgery was confirmed. The biopsy punch surgery will be used to simulate a patellar tendon injury. A post-surgery and post-euthanasia patellar tendon dissection protocol was practiced, refined, and established. The extracted tendons were used for measurements and grip design. They will also be used for pilot studies to validate the biomechanical testing protocol.

A biomechanical testing protocol was selected. This study was previously completed in female mice by [9-12], for mechanical and histologic data. We are repeating the study in a cohort of male mice. A small cohort of female mice will be used to run

biochemical and RNA sequencing assays. Methods to grip the patellar tendon for mechanical testing to researched, carefully considered, and decided upon for the planar biaxial device. Future improvements to the grips include modifying the current grips of the planar biaxial device to allow for a PMMA pot for the tibia. This will improve gripping methods since the local mechanics of the tibia will remain intact. Lastly, a histologic, biochemical, and RNA sequencing assay were described.

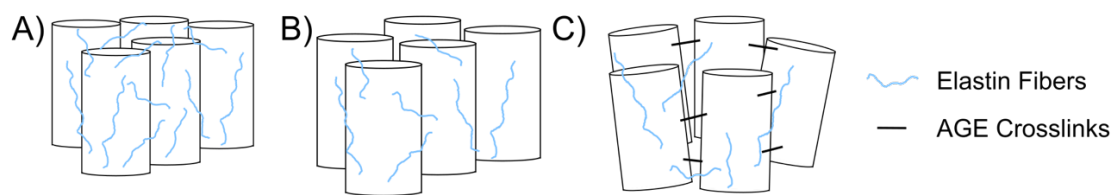


Figure 22: *It is our hypothesis that with age, the tendons experience a progressive loss of elastin bridges between collagen fibers (A-C) and altered collagen deposition, including compensatory increase productive of Advanced Glycation End products (AGE)-crosslinks*

We hypothesize that with age, the tendon will experience a reduction of mechanical integrity, which could be attributed to a loss of elastic fiber integrity, decreased collagen organization, and increased collagen crosslinks. Additionally, we posit that the possibility for the tendon to heal will decline with age. The design of this study allows for the examination of alternate hypotheses in the case that the current hypothesis is refuted. The results of this study will characterize the mechanical properties of the murine patellar tendon at different time points to advance our knowledge of age-related tendon healing.

The results from this study will ultimately inform a constitutive model of the murine patellar tendon. Specifically, a growth and remodeling model will be developed to evaluate important features of tendon adaptation before and after injury. The data from this study, in conjunction with the data acquired from [9-12], will be used to iteratively refine the G&R equations controlling the production, removal, and organization of each load-bearing

constituent. This study will provide the basis for the assessment of patellar tendon healing throughout the aging process as well treatments for age-related tendon injury.

V. ANALYSIS OF SEX DIFFERENCES IN ROTATOR CUFF TENDONS VIA BIAXIAL MECHANICAL TESTING

The probability of sustaining a connective tissue e (e.g., tendon) injury is higher in women than men [31]. Specifically, rotator cuff tendon injuries are the third-leading cause of pain of the musculoskeletal system, following the knee and spine [26]. It is hypothesized that these injuries may have a mechanical etiology. The underlying mechanisms for gender differences in connective tissue injuries, however, are poorly understood. Estrogen has been suggested to contribute to sex-differences in tendon. Estrogen, the primary female sex hormone, inhibited the growth of fibrillar collagen, the primary structural constituent of tendon, by inhibiting the action of the protein that allows skeletal muscles to recover from injury [120]. Further, the fluctuations of steroid hormones during the menstrual cycle have been suggested to contribute to tendon injuries. Data remains inconclusive, however [121].

Additionally, uniaxial testing of tendons has been predominantly performed [27-30]. Mounting evidence suggests that tendons within the rotator cuff complex experience multi-axial loads [122, 123] and demonstrate anisotropic behavior [23]. Specifically, biaxial testing of the Supraspinatus tendon more accurately characterizes its behavior. Biaxial testing allows for more physiologically relevant boundary conditions [23]. Herein, biaxial testing may provide a better understanding of the *in vivo* loading conditions and tissue anisotropy.

Identifying tendon structure-function relationships will improve our ability to better understand, explain, and predict the sex-specific behavior of the tendon. In order to ascertain patient specific risk factors for tendon injuries and improved tissue engineering

strategies, comprehensive mathematical models are necessary to predict soft tissue mechanical behavior and guide the design of clinical interventions. This can be accomplished through soft tissue mechanical testing.

Chapter 5: CONCLUSIONS AND FUTURE DIRECTIONS

I. OVERALL CONCLUSIONS

This chapter will summarize findings and major conclusions from previous chapters. The overall aim of this thesis was to elucidate structure-function relationships of soft biological tissues. Structure-function relationships of soft tissues provide information towards clinical treatment and prevention plans for many diseases and etiologies. These relationships can be elucidated via mechanical testing. Specifically, planar biaxial mechanical testing has been shown to simulate physiologically relevant conditions for soft tissues [13]. In this thesis, a planar biaxial mechanical testing device was built, programmed, and validated (Chapters 2 and 3).

I.1 Successful Design, Construction, and Programing of a Custom Planar Biaxial Mechanical Testing Device

Chapter two described the design, construction, and programming of a custom planar biaxial mechanical testing device. Constitutive models are necessary for numerous physiological, surgical, and medical device applications for soft biological tissues [13]. Due to the complex mechanical behavior of soft tissues, constitutive models can be difficult to develop. Biaxial mechanical testing of soft tissues provides two and three-dimensional strain information for constitutive models. Therefore, there is a need to build biaxial mechanical testing devices to properly inform constitutive models. The objective of this chapter was to design, construct, and validate a custom planar biaxial mechanical testing device.

Extensive research was done prior to purchasing and fabrication of hardware components. Modifications were made to many of our custom-made components as different issues arose. A LabVIEW code was written for motion control, data acquisition, and image acquisition. Mechanical testing protocols were also incorporated into the LabVIEW code. Furthermore, user-friendly interfaces were created to run these mechanical testing protocols. The planar biaxial device has the potential to impact many clinical fields of study, such as cardiothoracic, orthopaedic, and women's reproductive health.

I.2 Validation of the Planar Biaxial Mechanical Testing Device via Pilot Study in Murine Skin

Chapter three presented a murine skin pilot study for validation, as well as individual system validations, of the planar biaxial device. Before other studies can be conducted, a pilot study needed to be performed to confirm the entire system functions properly. Skin is an excellent choice for a pilot study to verify the planar biaxial device since it is anisotropic and its mechanical properties are well characterized [17, 32]. Therefore, the objective of this chapter was to validate the planar biaxial device via characterization of murine skin mechanical properties.

Individual systems of the planar biaxial device, which are motion control, data acquisition, and image acquisition, were successfully validated through external sources and measurements. Additionally, the integration of all systems of the biaxial device were validated through a murine skin pilot study. Data produced from the planar biaxial device falls within range of data in the literature. Differences in reference configuration and biological variability can account for discrepancies in our data versus literature data. Now that the planar biaxial device is successfully validated, other studies can take place.

APPENDIX

A. Planar Biaxial Device Parts List

A1. Motion Controls Parts List

Company	Part Description	Quantity	Unit Price	Total Price
Advanced Micro Systems	Stepper Motor, High torque, 75ozin, Frame size 17, single shaft	4	\$115.00	\$460.00
	Max 420 Controllers	2	\$1,419.00	\$2,838.00
	USB for Controller SIN-11-USB	1	\$99.00	\$99.00
Thomson BSA	Linear screws X4: M17S4, M17S4-MTS 10x2M-2.0" Stroke	4	\$506.35	\$2,025.40
<i>Total</i>				\$5,422.40

A2. Data Acquisition Parts List

Company	Part Description	Quantity	Unit Price	Total Price
Honeywell	MODEL 31, 50 gm, 60 to 160 deg. F. (15 to 70 deg.C) Temperature Compensation, Non-amplified (mv/v), Overload Stops, Submersible cable, 10 ft (3 meter) Long, Radial Electrical Exit Orientation	2	\$1,212.00	\$2,424.00

	MODEL 34, 5lb, Temperature Compensation 60 to 160 deg. F. (15 to 70 deg.C)Temperature Compensation, Internal Amplifiers, Non-amplified (mv/v) Overload Stops, Electrical 2.00 Termination Teflon cable, 5 ft (1.5 meter) Long Special Calibration 10 point final calibration Cable Exit Port Orientation Radial Electrical Exit Orientation Load Cells Special Load Cell Calibration Calibrate in Tension and Compression	2	\$1,296.00	\$2,592.00
National Instruments	NI 9237 4-Ch 50 kS/s per Channel, 24-Bit Bridge Analog Input Module	1	\$1,214.00	\$1,214.00
	cDAQ-9171, CompactDAQ Chassis (1 slot USB)	1	\$252.00	\$252.00
	RJ50 Cable for 9944, 9945, and 9949, 2m (qty 4)	1	\$27.90	\$27.90
	NI 9949 RJ-50 (female) to Screw Terminal Adaptor (Qty 4)	1	\$172.80	\$172.80
	NI 9942 4-Position Connector Kit	1	\$8.10	\$8.10
			<i>Total</i>	\$4,266.80

A3. Image Acquisition Parts List

Company	Part Description	Quantity	Unit Price	Total Price
Edmund Optics	AVT Manta G-419 1" NIR CMOS Camera	1	\$2,065.50	\$2,065.50
	12V 12-Pin Regulated HIROSE Power Supply	1	\$99.00	\$99.00
	1/4 Mirror 75mmx75mm Enhanced Aluminum	1	\$148.50	\$148.50
	45 degree mounts: 1" Offset, 1" OD Mount, 45 Degree Mounting Adapter	2	\$26.10	\$52.20
	3.0" Medium Mirror Mount	1	\$121.50	\$121.50
	6.5X Zoom Body 1-6232	1	\$917.00	\$917.00
	1X Short Tube Adapter 1-6245	1	\$350.00	\$350.00
Navitar Inc.	C-Mount Coupler: 1-6010	1	\$56.00	\$56.00
	Right Angle Lens Attachment: 1-62866	1	\$491.00	\$491.00
	0.75X Lens Attachment: 1-60111	1	\$170.00	\$170.00
	Universal Mounting Clamp: 1-6270	1	\$137.00	\$137.00
	150W Halogen Light Supply: 8-61172	1	\$520.00	\$520.00
	Fiberoptic Ring Light: 1-61214	1	\$473.00	\$473.00
	1D Linear Stage X3: TSX-1D, Dovetail Linear Stage, 1.0 inch travel, 1/4-20	3	\$149.94	\$449.82
ThorLabs	Rod Clamp: 340-RC	1	\$69.94	\$69.94
	Kinematic Base: 3" x 3" (75mm x 75mm)	1	\$90.40	\$90.40
	Mounting Post Base 2.48x0.4	1	\$23.70	\$23.70
	Mounting Post, 1/4"-20 taps	1	\$38.00	\$38.00
<i>Total</i>				\$6,272.56

A4. Custom Fabrication Parts List

Company	Part Description	Quantity	Unit Price	Total Price
Jameco	Weller WES51 Analog Soldering Station Power Unit Soldering Pencil Stand Sponge	1	\$134.95	\$134.95
	1 Pound Solder Roll Sn60 Pb40 0.031 Inch Diameter	1	\$32.95	\$32.95
	High Vacuum Manual Desolder Pump	1	\$8.95	\$8.95
	Hookup Wire 1 Conductor 26AWG Gray Stranded PVC 300 Volt UL1007/UL1569	1	\$6.75	\$6.75
	Solder Spool Stand	1	\$12.95	\$12.95
McMaster Carr	General Purpose Tap, Through Hole (Plug), 6-32 Thread Size	2	\$4.65	\$9.30
	General Purpose Tap, Through Hole (Plug), 8-32 Thread Size	2	\$4.83	\$9.66
	General Purpose Tap, Through Hole (Plug), 10-32 Thread Size	2	\$4.96	\$9.92
	Sliding Machine-Mount T-Handle Tap Wrench for Number 0 to 1/4" OR 1.6 mm to 6.3mm tap sizes	1	\$17.92	\$17.92
	Type 316 Stainless Steel Flat Head Slotted Machine Screw, 1/4"-20 Thread, 1/2 Length, pack of 25	1	\$10.00	\$10.00
	Zinc Plated Alloy Steel Socket Head Cap Screw, 1/4"-20 Thread, 3/8" Length, pack of 25	1	\$6.47	\$6.47
	Nonmarring Flat Point Socket Set Screw, Type 316 Stainless Steel, 6-32	3	\$4.65	\$13.95

	Thread, 3/8" Long, pack of 10			
McMaster Carr cont.	Type 316 Stainless Steel Head Cap Screw, 8-32 Thread, 1/2" Length, pack of 25	1	\$3.23	\$3.23
	Type 316 Stainless Steel Socket Head Cap Screw, 8-32 Thread, 5/8" Length, packs of 25	1	\$3.55	\$3.55
	Type 18-8 Stainless Steel Hex Nut with Tooth Washer, 8-32 Thread Size, 11/32" Nut Width, 11/64" Overall Height, packs of 100	1	\$8.61	\$8.61
	Slotted Disc Flexible Shaft Coupling, Set Screw Hub, 5/8" Overall Length	4	\$10.54	\$42.16
	Miniature 12L14 Drive Steel Shaft, 3/16" OD, 3" Length	8	\$3.13	25.04
	Pan Head Thread-Forming Screw for Sheet Metal, Zinc-Plated Steel, M3 Thread, 4mm Length	1	\$10.50	\$10.50
			<i>Total</i>	\$896.46

A5. Miscellaneous Parts List

Company	Part Description	Quantity	Unit Price	Total Price
Dell	Optiplex 7020			
Electro Industries	DC power supply 303DM	1	\$329.00	\$329.00
			<i>Total</i>	\$329.00

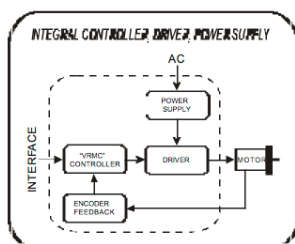
B. Motion Controls Specification Sheets and Drawings

B1. MAX-420 Controller Specification Sheet



Precision Stepper Motor Control and Drive Products
ADVANCED MICRO SYSTEMS, INC.

MAX-410 AND MAX-420 SINGLE AND DUAL AXIS MICROSTEP POSITIONING SYSTEMS



OVERVIEW

The MAX-410 (single axis) and MAX-420 (dual axis) are full function microstep positioning systems with integral driver (4 amps) and power supply (40Vdc). Standard features include 2k bytes of non-volatile memory for program storage, extended user I/O facilities, programmable motor current and independent acceleration/deceleration ramping.

Programming is through high-speed RS-422 serial interface with simple mnemonic commands for plug-and-play operation. Optional encoder circuitry provides stall detection and position feedback for closed-loop operation.

The MAX systems incorporate AMS' proprietary "Variable Resolution Microstep Control" (VRMC®) indexing technology for accurate and repeatable positioning at any shaft speed. Step resolution ranges from 400 to over 50,000 steps per revolution.

Short circuit, over temperature and under voltage protection, combined with special "Watchdog" software, ensure trouble-free operation in any environment. For export, CE certified models are also available.



FEATURES

- Integral controller/driver/power supply
- Rugged, compact design
- Low cost
- Short circuit/over temp. protected
- Output current of 4 amps @ 40Vdc
- 1/256 motor step resolution
- Fixed or variable step resolution
- Programmable run/hold current
- RS-422 "Party Line" operation
- Programmable accel/decel ramps
- Six buffered user I.O. ports
- 2k bytes of non-volatile memory
- Optically isolated home/limits
- Self-contained home routine
- Dual speed jog inputs
- Go and soft stop inputs
- Programmable trip point
- Encoder feedback option
- Watchdog S/W for extra reliability

SERIAL INTERFACE

The MAX systems feature full duplex serial communications. A "Party Line" interface implements a differential transmission and receiver pair that provides reliable communication in industrial environments. This protocol permits simultaneous communication (up to 32 axis) with minimum command processing latency.

PROGRAMMABLE CURRENT

The MAX has a programmable current feature that controls motor winding current to within 1% resolution. Independent settings for "RUN" and "HOLD" currents permit full motor torque when stepping. Automatic power down to the hold current value minimizes motor power dissipation when the system is in an idle mode of operation.

PROGRAMMING

Programs can be stored in non-volatile memory by using a host computer or dumb terminal. For stand-alone use there is a "GO" switch input. Additional input ports can test and branch to multiple motion subroutines. Two programmable outputs are available to drive solid state relays and other devices. A separate "TRIP" function provides automatic program branching when a specified motion is passed. Additional control inputs include soft stop, dual speed jog and step by step monitoring of travel limits.

ENCODER FEEDBACK

All MAX systems are easily upgraded to include encoder feedback for "closed loop" applications that require positional feedback data and stall detection. A built-in "line count" multiplier extends normal encoder resolution by a factor of four, providing greater accuracy at less cost.

COMMANDS

ESC	Abort/Terminate
@	Soft Stop
^C	Reset
A	Port Read/Write
B	Set Jog Speeds
C	Clear and Restore
c	Reset Driver
D	Divide Step Rates
E	Enable Auto Power Down
F	Find Home (SPS)
G	Go
H	Step Resolution
I	Initial Velocity (SPS)
J	Jump to Address N + 1 (X)
K	Ramp Slope
k	Special Trip
L	Loop on Port
l	Invert Limit Polarity
M	Move at Constant Speed
O	Set Origin
P	Program Mode
Q	Query (List) Program
R	Index to Target Position
S	Store Parameters
T	Trip Point Set
V	Slew Velocity (SPS)
W	Wait N Milliseconds
w	Read Error Status
X	Examine Parameters
Y	Hold/Run Currents
y	Control Line Feed
Z	Display Position
+	Index in + Direction
-	Index in - Direction
[Read NV Memory
\	Write to NV Memory
]	Read Limits/Hardware
^	Read Moving Status
	Selective Termination

ENCODER COMMANDS

a	Read Stall Count
d	Deadband Enable
e	Encoder Resolution
f	Find Encoder Mark
g	Hunt On/Off
h	Hunt Resolution
m	Index Move
n	Force Encoder Position
o	Set Origin to Zero
r	Set Stall Retry Count
s	Stall Factor
t	Stall Test Data
v	Hunt Velocity
z	Read Encoder Position

AUXILIARY I.O. SIGNALS

Signal (J5)	Type	Signal (J5)	Type	Signal (J3)	Type
Gnd	Power	Jog Speed	Input	Opto+	Input
Port 1	Input	Jog 1	Input	Limit A	Input*
Port 2	Input	Jog 2	Input	Limit B	Input*
Port 3	Input	Go	Input	Home	Input*
Port 4	Input	Soft Stop	Input	Go	Input
Port 4	Output	VIO	Input	Gnd	Power
Port 5	Output	Gnd	Power		
Port 6	Output	12Vdc	Output		*Optically Isolated

ELECTRICAL

Power Supply.....40Vdc @90VA

Output Current (Peak).....4 Amps

Chopping Frequency.....28kHz

Input Voltage.....100 to 125 VAC, 60 Hz or 200 to 250 VAC, 50Hz

I.O. Board (J5)	Min	Typ	Max	Units
I.O. Supply (VIO)	5		28	Vdc
Inputs (Ports 1,2,3,4):				
Input Voltage	-0.7		VIO	Vdc
Input Current			4	mA
Outputs (Ports 4,5,6):				
Output Voltage			36	Vdc
Output Current			0.5	Amp (cont.)

Control Board (J3)	Min	Typ	Max	Units
I.O. Supply (OPTO+)	5		12	Vdc
OPTO+ Inputs	-0.7		OPTO+	Vdc
Encoder Supply Voltage		5		Vdc
Encoder Supply Current			50	mA
Encoder Inputs	-0.7		5.7	Vdc
Encoder Input Currents		5	10	mA
RS-485 Inputs	-10		+15	Vdc
RS-485 Outputs		5		Vdc

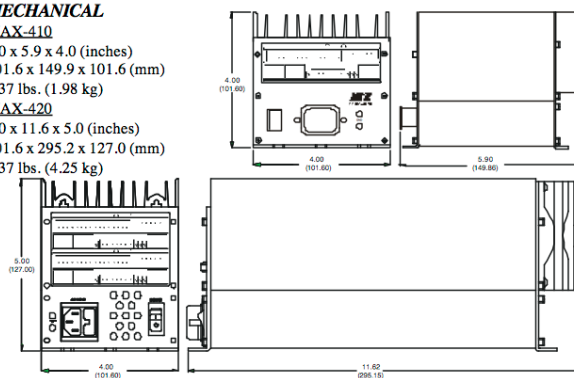
MECHANICAL

MAX-410

4.0 x 5.9 x 4.0 (inches)
 101.6 x 149.9 x 101.6 (mm)
 4.37 lbs. (1.98 kg)

MAX-420

4.0 x 11.6 x 5.0 (inches)
 101.6 x 295.2 x 127.0 (mm)
 9.37 lbs. (4.25 kg)



B2. AM-17-75 Stepper Motor Specification Sheet



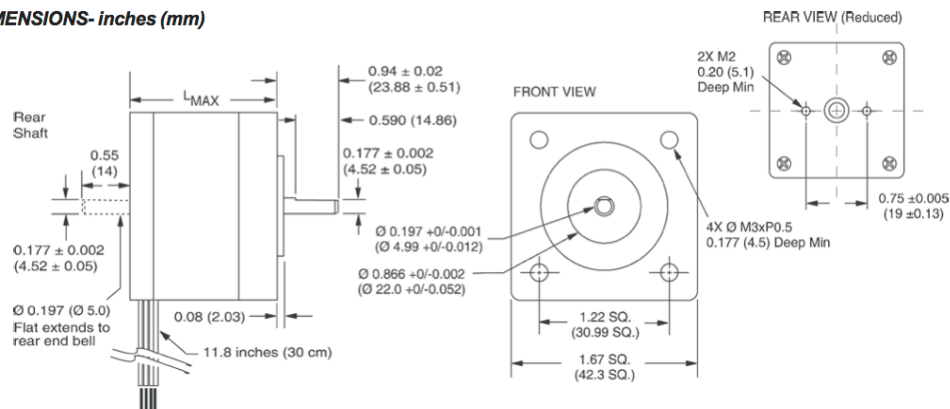
Precision Step Motor Control and Drive Products
ADVANCED MICRO SYSTEMS, INC.

SIZE 17 1.8° HYBRID STEPPING MOTORS

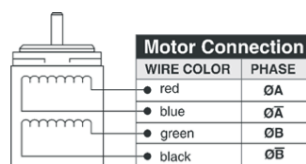
SPECIFICATIONS

Model Number	Holding Torque oz-in (N-cm)	Phase Current Amps	Number of Leads	Phase Resistance Ohms	Phase Inductance mH	Detent Torque oz-in-sec ²	Rotor Inertia oz-in-sec ²	L ^{MAX} Length inches (cm)	Weight oz (gm)
AM17-32-1	32 (23)	1.5	4	1.3	2.1	1.7 (1.2)	0.000538 (0.038)	1.34 (3.4)	7.4 (210)
AM17-60-2	60 (42)	1.5	4	2.1	5.0	2.1 (1.5)	0.0008037 (0.057)	1.57 (4.0)	8.1 (230)
AM17-75-3	75 (53)	1.5	4	2.0	3.85	3.5 (2.5)	0.0011562 (0.082)	1.89 (4.8)	12.7 (360)

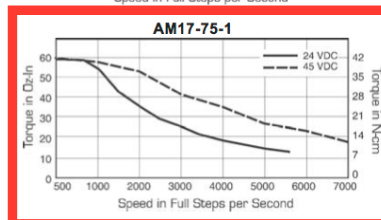
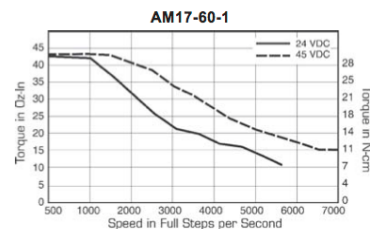
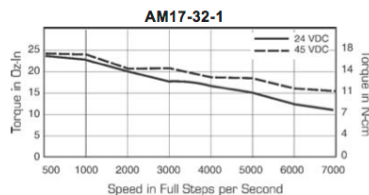
DIMENSIONS- inches (mm)



CONNECTION



TORQUE SPEED CURVES- 1.5 Amps RMS



D. Data Acquisition Specification Sheets

D1. Model 31 Load Cell Specification Sheet

Model 31 Low

PERFORMANCE SPECIFICATIONS

Characteristic	Measure
Load ranges ^a	50 g, 150 g, 250 g, 500 g
Linearity	±0.15 % full scale
Hysteresis	±0.15 % full scale
Non-repeatability	±0.1 % full scale
Tolerance on output 50 g to 150 g	0,1 mV/V max.
Tolerance on output 250 g to 500 g	20 mV/V
Operation	Tension/compression ²
Resolution	Infinite

ENVIRONMENTAL SPECIFICATIONS

Characteristic	Measure
Temperature, operating	-53 °C to 121 °C [-65 °F to 250 °F]
Temperature, compensated	15 °C to 71 °C [60 °F to 160 °F]
Storage temperature	-73 °C to 148 °C [-100 °F to 300 °F]
Temperature effect, zero	0.015 % full scale/°F
Temperature effect, span	0.015 % full scale/°F

ELECTRICAL SPECIFICATIONS

Characteristic	Measure
Strain gage type	Semiconductor
Excitation (calibration)	5 Vdc
Insulation resistance	5000 Mohm @ 50 Vdc
Bridge resistance	500 ohm
Zero balance	1 % max.
Electrical termination (std)	Teflon cable (5 ft)

MECHANICAL SPECIFICATIONS

Characteristic	Measure
Maximum allowable load	5 lb ¹
Weight	90 g
Material	17-4 PH stainless steel
Deflection full scale	0,020 mm [0.0008 in]
Natural frequency	740 Hz

WIRING CODES

Cable	
Red	(+) excitation
Black	(-) excitation
Green	(-) output
White	(+) output

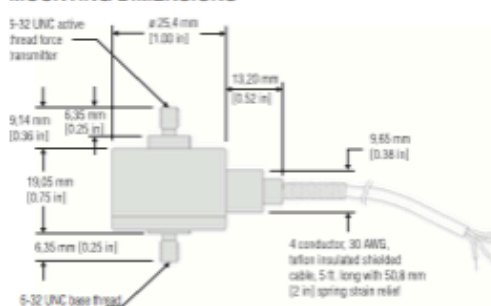
RANGE CODES

Range Codes	Range
AJ	50 g
AL	150 g
AN	250 g
AP	500 g

OPTION CODES

	Many range/option combinations are available in our quick-ship and fast-track manufacture programs. Please see http://sensing.honeywell.com/TMSensor-ship for updated listings.	
Load range	50, 150, 250, 500 g	
Temperature compensation	1a. 60 °F to 160 °F 1b. 30 °F to 130 °F 1c. 0 °F to 185 °F 1d. -20 °F to 130 °F	1e. -20 °F to 200 °F 1j. 0 °F to 50 °C 1k. -20 °C to 85 °C 1m. -25 °C to 110 °C
Internal amplifiers	2u. Unamplified, mV/V output	
Overload stops	4a. Overload stop	
Electrical termination	6d. Microtec DR-4S-4H 4-pin 6e. Integral cable: Teflon 6f. Integral cable: PVC 6h. Integral cable: Silicone	6i. Integral underwater cable (max. 82 °C [180 °F]) 6v. Phoenix connector on end of cable 15d. Connector on end of cable
Special calibration	30a. Compression only calibration, positive in compression 30b. Tension and compression calibration, positive in tension 30c. Compression only calibration, negative in compression	
Shock and vibration	44a. Shock and vibration resistance	
Interfaces ⁴	53e. Signature calibration ³ 53i. TEDS IEEE 1451.4 module	

MOUNTING DIMENSIONS



D2. Model 34 Load Cell Specification Sheet

Model 34

PERFORMANCE SPECIFICATIONS

Characteristic	Measure
Load ranges ⁶	1000 g, 5 lb, 10 lb, 25 lb, 50 lb, 100 lb, 250 lb, 500 lb, 1000 lb
Linearity 1000 g to 250 lb	±0.15 % full scale
Linearity 500 lb to 1000 lb	±0.2 % full scale
Hysteresis 1000 g to 250 lb	±0.15 % full scale
Hysteresis 500 lb to 1000 lb	±0.2 % full scale
Non-repeatability 1000 g	±0.1 % full scale
Non-repeatability 5 lb to 1000 lb	±0.05 % full scale
Tolerance on output 1000 g	1.5 mV/V (nominal)
Tolerance on output 5 lb to 1000 lb	2 mV/V
Operation	Tension/compression ³
Resolution	Infinite

ENVIRONMENTAL SPECIFICATIONS

Characteristic	Measure
Temperature, operating	-53 °C to 121 °C [-65 °F to 250 °F]
Temperature, compensated	15 °C to 71 °C [60 °F to 160 °F]
Storage temperature	-73 °C to 148 °C [-100 °F to 300 °F]
Temperature effect, zero	0.005 % full scale/°F
Temperature effect, span	0.005 % full scale/°F

ELECTRICAL SPECIFICATIONS

Characteristic	Measure
Strain gage type	Bonded foil
Excitation (calibration) 1 kg to 10 lb	5 Vdc
Excitation (calibration) 25 lb to 1000 lb	10 Vdc
Insulation resistance	5000 Mohm @ 50 Vdc
Bridge resistance	350 ohm
Electrical termination (std) 1000 g to 10 lb	Teflon cable (1524 mm [5 ft]) with balance board
Electrical termination (std) 25 lb to 1000 lb	Teflon cable (1524 mm [5 ft])

MECHANICAL SPECIFICATIONS

Characteristic	Measure
Maximum allowable load	150 % FS ¹
Weight	See table
Material	17-4 PH stainless steel
Deflection full scale	See table
Natural frequency	See table

RANGE CODES

Range codes	Range
AR	1000 g
AT	5 lb
AV	10 lb
BL	25 lb
BN	50 lb
BR	100 lb
CN	250 lb
CR	500 lb
CV	1000 lb

WIRING CODES

Cable	Unamplified
Red	(+) excitation
Black	(-) excitation
Green	(-) output
White	(+) output

DEFLECTIONS AND RINGING FREQUENCIES

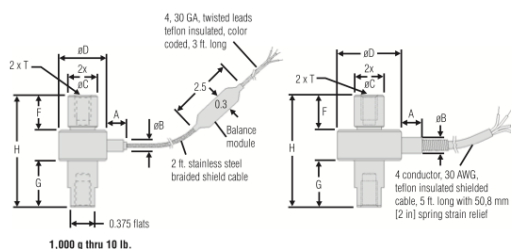
Capacity (lb)	Deflection at full scale (in)	Ringling frequency (Hz)	Weight (g)
1000 g to 10 lb	0,03 mm [0.001 in]	1000 Hz	40 g [0.09 lb]
25 lb to 100 lb	0,03 mm [0.001 in]	3000 Hz	80 g [0.18 lb]
250 lb to 1000 lb	0,05 mm [0.0015 in]	5000 Hz	100 g [0.22 lb]

Honeywell

Precision Miniature Load Cell

MOUNTING DIMENSIONS

Ranges	D mm [in]	H mm [in]	A mm [in]	B mm [in]	C mm [in]	F mm [in]	G mm [in]	T
1000 g, 5 lb, 10 lb	19,05 [0.75]	44,45 [1.75]	7,87 [0.31]	4,83 [0.19]	4,83 [0.46]	15,24 [0.60]	18,29 [0.72]	1/4-28 UNF
25 lb, 50 lb, 100 lb	25,4 [1.00]	44,45 [1.75]	12,7 [0.50]	6,35 [0.25]	4,83 [0.46]	13,21 [0.52]	18,29 [0.72]	1/4-28 UNF
250 lb, 500 lb, 1000 lb	25,4 [1.00]	50,8 [2.00]	12,7 [0.50]	6,35 [0.25]	4,83 [0.46]	19,05 [0.75]	19,05 [0.75]	1/4-28 UNF



OPTION CODES

	Many range/option combinations are available in our quick-ship and fast-track manufacture programs. Please see http://sensing.honeywell.com/TMSensor-ship for updated listings.	
Load range	1000 g, 5 lb, 10 lb, 25 lb, 50 lb, 100 lb, 250 lb, 500 lb, 1000 lb	
Temperature compensation	1a. 60 °F to 160 °F 1b. 30 °F to 130 °F 1c. 0 °F to 185 °F 1d. -20 °F to 130 °F 1e. -20 °F to 200 °F 1j. 0 °C to 50 °C	1k. -20 °C to 85 °C 1m. -25 ° to 110 °C 1f. 70 °F to 250 °F 1g. 70 °F to 325 °F 1h. 70 °F to 400 °F 1i. -65 °F to 250 °F
Internal amplifiers	2u. Unamplified, mV/V output	
Overload stops	4a. Overload stops	
Electrical termination	6a. Bendix PTIH-10-6P - 6 pin (max. 250 °F) ² 6d. Microtec DR-4S-4H 4 pin 6e. Integral cable: Teflon 6f. Integral cable: PVC 6g. Integral cable: Neoprene (max. 180 °F)	6h. Integral cable: Silicone 6i. Integral underwater cable (max. 180 °F) 6v. Phoenix connector on end of cable 15d. Connector on end of cable
Special calibration	9a. 10 point (5 up/5 down) 20 % increments @ 20 °C 9b. 20 point (10 up/10 down) 10 % increments @ 20 °C	
Special calibration	30a. Compression only calibration, positive in compression 30b. Tension and compression calibration, positive in tension 30c. Compression only calibration, negative in compression	
Shock and vibration	44a. Shock and vibration resistance	
Interfaces⁴	53e. Signature calibration ⁷ 53t. TEDS IEEE 1451.4 module	

D3. National Instruments 24-bit Analog Input Module (NI-9237) Specification Sheet



Technical Sales

(866) 531-6285

orders@ni.com


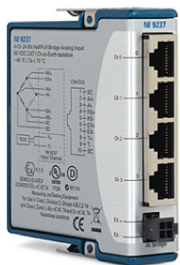
Requirements and Compatibility | Ordering Information | Detailed Specifications | Pinouts/Front Panel Connections

For user manuals and dimensional drawings, visit the product page resources tab on ni.com.

Last Revised: 2014-11-06 07:14:46.0

NI 9237

±25 mV/V, Bridge Analog Input, 50 kS/s/ch, 4 Ch Module



- Built-in full- and half-bridge measurements
- 120 and 350 Ω quarter-bridge completion via NI 9944/45 accessory kits
- 24-bit resolution on four simultaneous inputs sampled at up to 50 kS/s/ch
- Compatible with TEDS sensors

- Up to 10 V programmable excitation
- Connection for external excitation supply for specific levels
- 1,000 Vrms transient isolation for safety
- RJ50 (10P10C) or D-Sub connector options

Overview

The NI 9237 simultaneous bridge module for NI C Series devices contains all the signal conditioning required to power and measure up to four bridge-based sensors simultaneously. It can perform offset/null as well as shunt calibration and remote sense, all of which increase the accuracy of strain and bridge measurements.

For connectivity, you can select from two versions of the module: RJ50 or a 37-pin D-Sub. The RJ50 version, also known as 10P10C, offers quick sensor connection because you can use it for sensor termination. When you need a custom quarter-bridge design, choose the D-Sub version, which does not have an accessory for quarter-bridge completion. You also can use it with standard NI or other D-Sub accessories when you need only full- or half-bridge measurements.

The NI 9944 and NI 9945 accessories with quarter-bridge sensors have a female RJ50 connector on one end and screw terminals on the other end. You can purchase these accessories with a kit of RJ50 cables (quantity 4).

For screw terminals without the quarter-bridge completion, purchase the NI 9949 and a kit of RJ50 cables (quantity 4). This setup exposes all 10 pins for each channel as screw terminals.

[Back to Top](#)

Requirements and Compatibility		
OS Information	Driver Information	Software Compatibility
<ul style="list-style-type: none">• Real-Time OS• Windows	<ul style="list-style-type: none">• NI-DAQmx• NI-RIO	<ul style="list-style-type: none">• ANSI C/C++• LabVIEW• LabWindows/CVI• Measurement Studio• SignalExpress• Visual Basic• Visual Studio• Visual Studio .NET

[Back to Top](#)

Comparison Tables

1/8

www.ni.com

Module	Channels	Max Sample Rate (kS/s/ch)	Resolution (bits)	Quarter-Bridge	Half and Full	Simultaneous
NI 9237	4	50	24	yes (120/350 Ω)	yes	yes
NI 9237 D-Sub	4	50	24	no	yes	yes
NI 9235	8	10	24	120 Ω	no	yes
NI 9236	8	10	24	350 Ω	no	yes

[Back to Top](#)

Application and Technology

High-Speed Simultaneous Sampling

Mechanical test applications that involve impact testing, high-speed machinery, or moving vehicles often require high-speed sample rates to capture the event at full speed. You need to separate analog-to-digital converter (ADC) circuitry to perform a time-synchronous measurement as the strain event propagates through the structure. When you use multiple NI 9237 modules in either an NI CompactDAQ or CompactRIO chassis, all modules and channels are synchronized through a single set of clocked signals in the chassis.

Programmable Excitation

The NI 9237 can output voltage excitation up to 10 V. For more specific excitation requirements, the NI 9237 has inputs for external excitation. See the product manual for more information on excitation.

TEDS Compatibility

IEEE 1451.4, also known as TEDS (transducer electronic data sheet), technology consists of a standardized set of templates for specific sensors that store information such as manufacturer, manufacture date, calibration data, sensor-specific setup data, and more. TEDS is typically implemented on the sensor side via an onboard EEPROM. With this, the sensor has all of the information needed for setup and calibration stored locally, so you no longer have to keep up with paper data sheets. On the instrumentation side, the measurement system must have the capability to read and understand the TEDS data from the sensor. The NI 9237 has the capability to read TEDS information for TEDS-enabled sensors.

C Series Compatibility

The NI C Series hardware family features more than 50 measurement modules and several chassis and carriers for deployment. With this variety of modules, you can mix and match measurements such as temperature, acceleration, flow, pressure, strain, acoustic, voltage, current, digital, and more to create a custom system. Install the modules in one of several carriers to create a single module USB, Ethernet, or Wi-Fi system, or combine them in chassis such as NI CompactDAQ and CompactRIO to create a mixed-measurement system with synchronized measurements. You can install up to eight modules in a simple, complete NI CompactDAQ USB data acquisition system to synchronize all of the analog output, analog input, and digital I/O from the modules. For a system without a PC, CompactRIO holds up to eight modules and features a built-in processor, RAM, and storage for an embedded data logger or control unit. For higher-speed control, CompactRIO chassis incorporate a field-programmable gate array (FPGA) that you can program with NI LabVIEW software to achieve silicon-speed processing on I/O data from C Series modules.

[Back to Top](#)

Ordering Information

For a complete list of accessories, visit the product page on ni.com.

Products	Part Number	Recommended Accessories	Part Number
NI 9237 Module Kits			
NI 9237 (RJ50)	779521-01	No accessories required.	
NI 9237 D-Sub	780264-01	No accessories required.	
RJ50 Cables for Use with NI 9237			
RJ50 to RJ50 cable kit (2 m, qty 4)	194612-02	No accessories required.	
RJ50 to RJ50 cable (10 m, qty 1)	194612-10	No accessories required.	
RJ50 to "pigtail wires" or "flying leads" (2 m, qty 4)	195950-02	No accessories required.	
RJ50 to "pigtail wires" or "flying leads" (10 m, qty 1)	195950-10	No accessories required.	
D-Sub Cables for Use with NI 9237 D-Sub			
37-pin D-Sub (M-F) shielded cable	778621-01	No accessories required.	
NI SH37F-Tajimi 37-pin D-Sub cable to connect to 7-pin male Tajimi connector (1 m, qty. 1)	199254-01	No accessories required.	
NI SH37F-Tajimi 37-pin D-Sub cable to connect to 7-pin male Tajimi connector (10 m, qty.1)	199254-10	No accessories required.	
External Excitation Connector			
Spare/replacement 4-position connector for external excitation on the NI 9237 (RJ50)	194611-01	No accessories required.	
D-Sub Terminal Blocks			
37-pin D-Sub to screw terminal connector block with vertical DIN-rail mount	778672-01	No accessories required.	
37-pin D-Sub to screw terminal connector block with horizontal DIN-rail mount	778673-01	No accessories required.	
NI CB-37F-LP unshielded I/O connector block	779353-01	No accessories required.	
RJ50 Connectivity Accessories			

NI 9945 - Quarter-bridge completion accessory (350 Ohm, qty. 4) purchase with cable kit	194739-01	No accessories required.
NI 9944 - Quarter-bridge completion accessory (120 Ohm, qty. 4) purchase with cable kit	194738-01	No accessories required.
NI 9949 - RJ50 to screw terminal adaptor (qty. 4) purchase with cable kit.	196809-01	No accessories required.
D-Sub Connector Kit		
NI 9933 - creates custom cable for NI 9237 using D-Sub to screw terminal connection	779103-01	No accessories required.

[Back to Top](#)

Software Recommendations

LabVIEW Professional Development System for Windows



- Advanced software tools for large project development
- Automatic code generation using DAQ Assistant and Instrument I/O Assistant
- Tight integration with a wide range of hardware
- Advanced measurement analysis and digital signal processing
- Open connectivity with DLLs, ActiveX, and .NET objects
- Capability to build DLLs, executables, and MSI installers

[Back to Top](#)

Support and Services

System Assurance Programs

NI system assurance programs are designed to make it even easier for you to own an NI system. These programs include configuration and deployment services for your NI PXI, CompactRIO, or Compact FieldPoint system. The NI Basic System Assurance Program provides a simple integration test and ensures that your system is delivered completely assembled in one box. When you configure your system with the NI Standard System Assurance Program, you can select from available NI system driver sets and application development environments to create customized, reorderable software configurations. Your system arrives fully assembled and tested in one box with your software preinstalled. When you order your system with the standard program, you also receive system-specific documentation including a bill of materials, an integration test report, a recommended maintenance plan, and frequently asked question documents. Finally, the standard program reduces the total cost of owning an NI system by providing three years of warranty coverage and calibration service. Use the online product advisors at ni.com/advisor to find a system assurance program to meet your needs.

Calibration

NI measurement hardware is calibrated to ensure measurement accuracy and verify that the device meets its published specifications. To ensure the ongoing accuracy of your measurement hardware, NI offers basic or detailed recalibration service that provides ongoing ISO 9001 audit compliance and confidence in your measurements. To learn more about NI calibration services or to locate a qualified service center near you, contact your local sales office or visit ni.com/calibration.

Technical Support

Get answers to your technical questions using the following National Instruments resources.

- **Support** - Visit ni.com/support to access the NI KnowledgeBase, example programs, and tutorials or to contact our applications engineers who are located in NI sales offices around the world and speak the local language.
- **Discussion Forums** - Visit forums.ni.com for a diverse set of discussion boards on topics you care about.
- **Online Community** - Visit community.ni.com to find, contribute, or collaborate on customer-contributed technical content with users like you.

Repair

While you may never need your hardware repaired, NI understands that unexpected events may lead to necessary repairs. NI offers repair services performed by highly trained technicians who quickly return your device with the guarantee that it will perform to factory specifications. For more information, visit ni.com/repair.

Training and Certifications

The NI training and certification program delivers the fastest, most certain route to increased proficiency and productivity using NI software and hardware. Training builds the skills to more efficiently develop robust, maintainable applications, while certification validates your knowledge and ability.

- **Classroom training in cities worldwide** - the most comprehensive hands-on training taught by engineers.
- **On-site training at your facility** - an excellent option to train multiple employees at the same time.
- **Online instructor-led training** - lower-cost, remote training if classroom or on-site courses are not possible.
- **Course kits** - lowest-cost, self-paced training that you can use as reference guides.
- **Training memberships** and training credits - to buy now and schedule training later.

Visit ni.com/training for more information.

Extended Warranty

NI offers options for extending the standard product warranty to meet the life-cycle requirements of your project. In addition, because NI understands that your requirements may change, the extended warranty is flexible in length and easily renewed. For more information, visit ni.com/warranty.

OEM

NI offers design-in consulting and product integration assistance if you need NI products for OEM applications. For information about special pricing and services for OEM customers, visit ni.com/oem.

Alliance

Our Professional Services Team is comprised of NI applications engineers, NI Consulting Services, and a worldwide National Instruments Alliance Partner program of more than 700 independent consultants and integrators. Services range from start-up assistance to turnkey system integration. Visit ni.com/alliance.

[Back to Top](#)

Detailed Specifications

The following specifications are typical for the range –40 to 70 °C unless otherwise noted.

Input Characteristics	
Number of channels	4 analog input channels
Bridge completion	
Half and Full	Internal
Quarter	External
ADC resolution	24 bits
Type of ADC	Delta-Sigma (with analog prefiltering)
Sampling mode	Simultaneous
Internal master timebase (f_M)	
Frequency	12.8 MHz
Accuracy	±100 ppm max
Data rate range (f_s) using internal master timebase	
Minimum	1.613 kS/s
Maximum	50 kS/s
Data rate range (f_s) using external master timebase	
Minimum	390.625 S/s
Maximum	51.3 kS/s
Data rates ¹	$\frac{f_M + 2^{56}}{n}$, $n = 1, 2, \dots, 31$
Typical input range	± 25 mV/V
Scaling coefficient	2.9802 nV/V per LSB
Overvoltage protection between any two pins	±30 V

Accuracy		
Measurement Conditions ²	Percent of Reading (Gain Error)	Percent of Range ³ (Offset Error)
Calibrated typ (25 °C, ±5 °C)	0.05%	0.05%
Calibrated max (– 40 to 70 °C)	0.20%	0.25%
Uncalibrated typ (25 °C, ±5 °C)	0.20%	0.1%
Uncalibrated max (– 40 to 70 °C)	0.60%	0.35%






Gain drift	10 ppm/°C max
Offset drift	
2.5 V excitation	0.6 μV/V per °C
3.3 V excitation	0.5 μV/V per °C
5 V excitation	0.3 μV/V per °C
10 V excitation	0.2 μV/V per °C

Channel-to-channel matching (calibrated)			
Input Signal Frequency (f_{in})	Gain		Phase
	Typical	Maximum	Maximum
0 to 1 kHz	0.15%	0.3%	$0.125^\circ/\text{kHz} \cdot f_{in}$
1 to 20 kHz	0.4%	1.1%	

Phase nonlinearity	
$f_{in} = 0$ to 1 kHz	$<0.001^\circ$
$f_{in} = 0$ to 20 kHz	$\pm 0.1^\circ$
Input delay	$38.4/f_s + 4.8 \mu\text{s}$
Passband	
Frequency	$0.45 \cdot f_s$
Flatness	0.1 dB max
Stopband	
Frequency	$0.55 \cdot f_s$
Rejection	100 dB
Alias-free bandwidth	$0.45 \cdot f_s$
Oversample rate	$64 \cdot f_s$
Rejection at oversample rate ⁴	
$f_s = 10$ kS/s	60 dB @ 640 kHz
$f_s = 50$ kS/s	90 dB @ 3.2 MHz
Common-mode voltage, all signals to earth ground	± 60 VDC
CMRR	
Relative to earth ground ⁵ ($f_{in} = 0$ to 60 Hz)	140 dB
Relative to EX- ($f_{in} = 0$ to 1 kHz)	85 dB
SFDR (1 kHz, -60 dBFS)	106 dB
Total Harmonic Distortion (THD)	
1 kHz, -20 dBFS	100 dB
8 kHz, -20 dBFS	90 dB

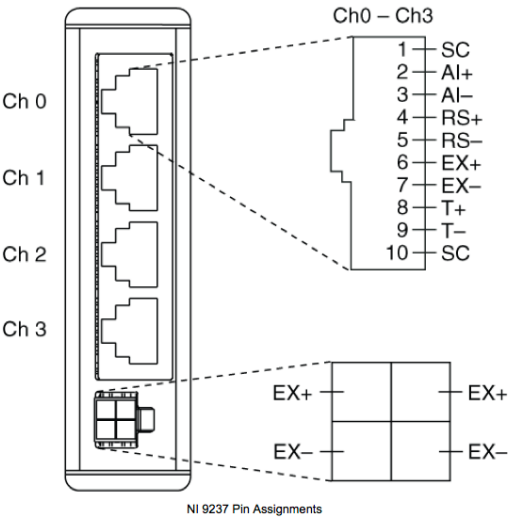
Input noise			
Excitation Voltage	Density (nV/V _{rms} per $\sqrt{1 \text{ Hz}}$)	Total $f_{in} = 0$ to 25 kHz ($\mu\text{V}/V_{\text{rms}}$)	Total $f_{in} = 0$ to 1 kHz (nV/V _{rms})
2.5 V	8	1.3	250
3.3 V	6	1.0	190
5 V	4	0.6	130
10 V	2	0.3	65

Excitation noise	$0.1 \text{ mV}/V_{\text{rms}}$
Crosstalk	
$f_{in} = 1$ kHz	110 dB
$f_{in} = 10$ kHz	100 dB
Excitation	
Internal voltage	2.5 V, 3.3 V, 5.0 V, 10.0 V
Internal power	150 mW max
External voltage	2 V to 10 V

Shunt calibration	
Resistance	100 k Ω
Resistor accuracy	
25 °C	$\pm 110 \Omega$
-40 to 70 °C	$\pm 200 \Omega$
MTBF	603,359 hours at 25 °C; Bellcore Issue 2, Method 1, Case 3, Limited Part Stress Method
	Note Contact NI for Bellcore MTBF specifications at other temperatures or for MIL-HDBK-217F specifications.
Power Requirements	
Power consumption from chassis	
Active mode	740 mW max
Sleep mode	25 μ W max
Thermal dissipation (at 70 °C)	
Active mode	740 mW max
Sleep mode	25 μ W max
Physical Characteristics	
Weight	152 g (5.4 oz)
Safety	
If you need to clean the module, wipe it with a dry towel.	
Safety Voltages	
Connect only voltages that are within the following limits.	
Between any two pins	± 30 V max
Isolation	
Channel-to-channel	None
Channel-to-earth ground	
Continuous	60 VDC, Measurement Category I
Withstand	1,000 V _{rms} , verified by a 5 s dielectric withstand test
Measurement Category I is for measurements performed on circuits not directly connected to the electrical distribution system referred to as MAINS ⁶ voltage. This category is for measurements of voltages from specially protected secondary circuits. Such voltage measurements include signal levels, special equipment, limited-energy parts of equipment, circuits powered by regulated low-voltage sources, and electronics.	
	Caution Do not connect the NI 9237 to signals or use for measurements within Measurement Categories II, III, or IV.
Safety Standards	
This product is designed to meet the requirements of the following standards of safety for electrical equipment for measurement, control, and laboratory use:	
<ul style="list-style-type: none"> • IEC 61010-1, EN 61010-1 • UL 61010-1, CSA 61010-1 	
	Note For UL and other safety certifications, refer to the product label or the <i>Online Product Certification</i> section.
Hazardous Locations	
U.S. (UL)	Class I, Division 2, Groups A, B, C, D, T4; Class I, Zone 2, AEx nC IIC T4
Canada (C-UL)	Class I, Division 2, Groups A, B, C, D, T4; Class I, Zone 2, Ex nC IIC T4
Europe (DEMKO)	EEx nC IIC T4
Electromagnetic Compatibility	
This product meets the requirements of the following EMC standards for electrical equipment for measurement, control, and laboratory use:	
<ul style="list-style-type: none"> • EN 61326 (IEC 61326): Class A emissions; Basic immunity • EN 55011 (CISPR 11): Group 1, Class A emissions • AS/NZS CISPR 11: Group 1, Class A emissions • FCC 47 CFR Part 15B: Class A emissions • ICES-001: Class A emissions 	
	Note For the standards applied to assess the EMC of this product, refer to the <i>Online Product Certification</i> section.
	Note For EMC compliance, operate this device with shielded cables.

CE Compliance	
This product meets the essential requirements of applicable European Directives, as amended for CE marking, as follows:	
<ul style="list-style-type: none">• 2006/95/EC; Low-Voltage Directive (safety)• 2004/108/EC; Electromagnetic Compatibility Directive (EMC)	
	Note For the standards applied to assess the EMC of this product, refer to the <i>Online Product Certification</i> section.
Online Product Certification	
Refer to the product Declaration of Conformity (DoC) for additional regulatory compliance information. To obtain product certifications and the DoC for this product, visit ni.com/certification , search by module number or product line, and click the appropriate link in the Certification column.	
Shock and Vibration	
To meet these specifications, you must panel mount the system.	
Operating vibration	
Random (IEC 60068-2-64)	5 g _{rms} , 10 to 500 Hz
Sinusoidal (IEC 60068-2-6)	5 g, 10 to 500 Hz
Operating shock (IEC 60068-2-27)	30 g, 11 ms half sine, 50 g, 3 ms half sine, 18 shocks at 6 orientations
Environmental	
National Instruments C Series modules are intended for indoor use only but may be used outdoors if installed in a suitable enclosure. Refer to the manual for the chassis you are using for more information about meeting these specifications.	
Operating temperature (IEC 60068-2-1, IEC 60068-2-2)	– 40 to 70 °C
Storage temperature (IEC 60068-2-1, IEC 60068-2-2)	– 40 to 85 °C
Ingress protection	IP 40
Operating humidity (IEC 60068-2-56)	10 to 90% RH, noncondensing
Storage humidity (IEC 60068-2-56)	5 to 95% RH, noncondensing
Maximum altitude	2,000 m
Pollution Degree (IEC 60664)	2
Environmental Management	
National Instruments is committed to designing and manufacturing products in an environmentally responsible manner. NI recognizes that eliminating certain hazardous substances from our products is beneficial not only to the environment but also to NI customers.	
For additional environmental information, refer to the <i>NI and the Environment</i> Web page at ni.com/environment . This page contains the environmental regulations and directives with which NI complies, as well as other environmental information not included in this document.	
Waste Electrical and Electronic Equipment (WEEE)	
	EU Customers At the end of their life cycle, all products <i>must</i> be sent to a WEEE recycling center. For more information about WEEE recycling centers and National Instruments WEEE initiatives, visit ni.com/environment/weee.htm .
	电子信息产品污染控制管理办法（中国 RoHS） 中国客户 National Instruments 符合中国电子信息产品中限制使用某些有害物质指令 (RoHS)。 关于 National Instruments 中国 RoHS 合规性信息, 请登录 ni.com/environment/rohs_china 。 (For information about China RoHS compliance, go to ni.com/environment/rohs_china .)
Calibration	
You can obtain the calibration certificate for this device at ni.com/calibration .	
Calibration interval	1 year
<p>¹ The data rate must remain within the appropriate data rate range. Refer to the <i>Understanding Data Rates</i> section of the <i>NI 9237 Operating Instructions and Specifications</i> for more information.</p> <p>² Before offset null or shunt calibration.</p> <p>³ Range equals 25 mV/V.</p> <p>⁴ Rejection by analog prefilter of signal frequencies at oversample rate.</p> <p>⁵ Measured with a balanced cable. Shielded cables that are not twisted-pair may be significantly unbalanced. To improve the balance of shielded, twisted-pair cables, NI recommends twisting together the AI+/AI– pair, the RS+/RS– pair, and the EX+/EX– pair.</p> <p>⁶ MAINS is defined as the (hazardous live) electrical supply system to which equipment is designed to be connected for the purpose of powering the equipment. Suitably rated measuring circuits may be connected to the MAINS for measuring purposes.</p>	
Back to Top	

Pinouts/Front Panel Connections



[Back to Top](#)

©2009 National Instruments. All rights reserved. CompactRIO, CVI, FieldPoint, LabVIEW, Measurement Studio, National Instruments, National Instruments Alliance Partner, NI, ni.com, NI CompactDAQ, and SignalExpress are trademarks of National Instruments. The mark LabWindows is used under a license from Microsoft Corporation. Windows is a registered trademark of Microsoft Corporation in the United States and other countries. Other product and company names listed are trademarks or trade names of their respective companies. A National Instruments Alliance Partner is a business entity independent from National Instruments and has no agency, partnership, or joint-venture relationship with National Instruments.

[My Profile](#) | [RSS](#) | [Privacy](#) | [Legal](#) | [Contact NI](#) © 2014 National Instruments Corporation. All rights reserved.

E. Image Acquisition Specification Sheets

E1. Manta G-419 A” NIR CMOS Camera Specification Sheet



[1-800-363-1992](tel:1-800-363-1992) | www.edmundoptics.com

Allied Vision Manta G-419 1" NIR CMOS Camera



Stock No. #88-460

\$2425.00

1 or more for \$2425.00.

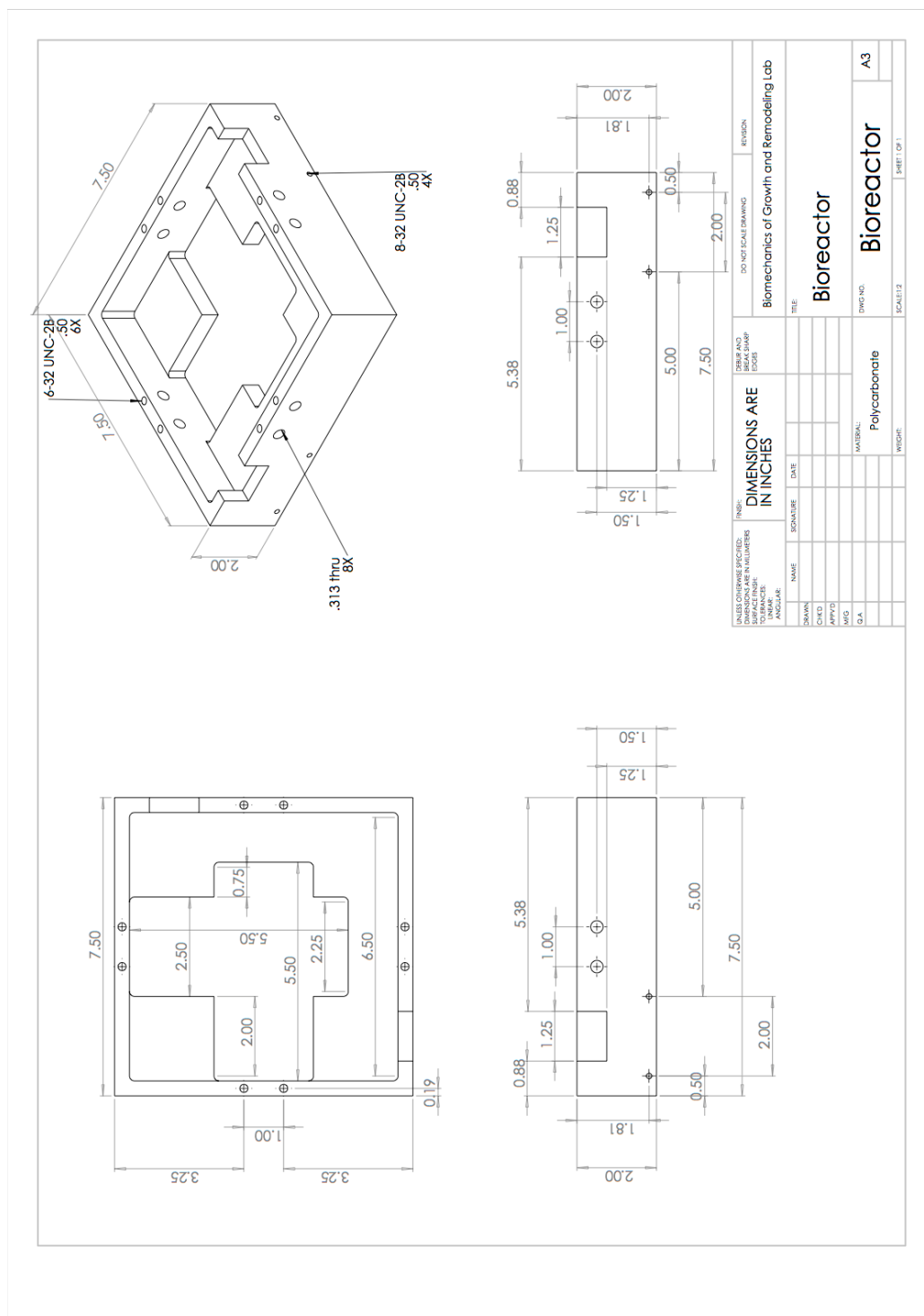
Availability: [CONTACT US](#)

Specifications

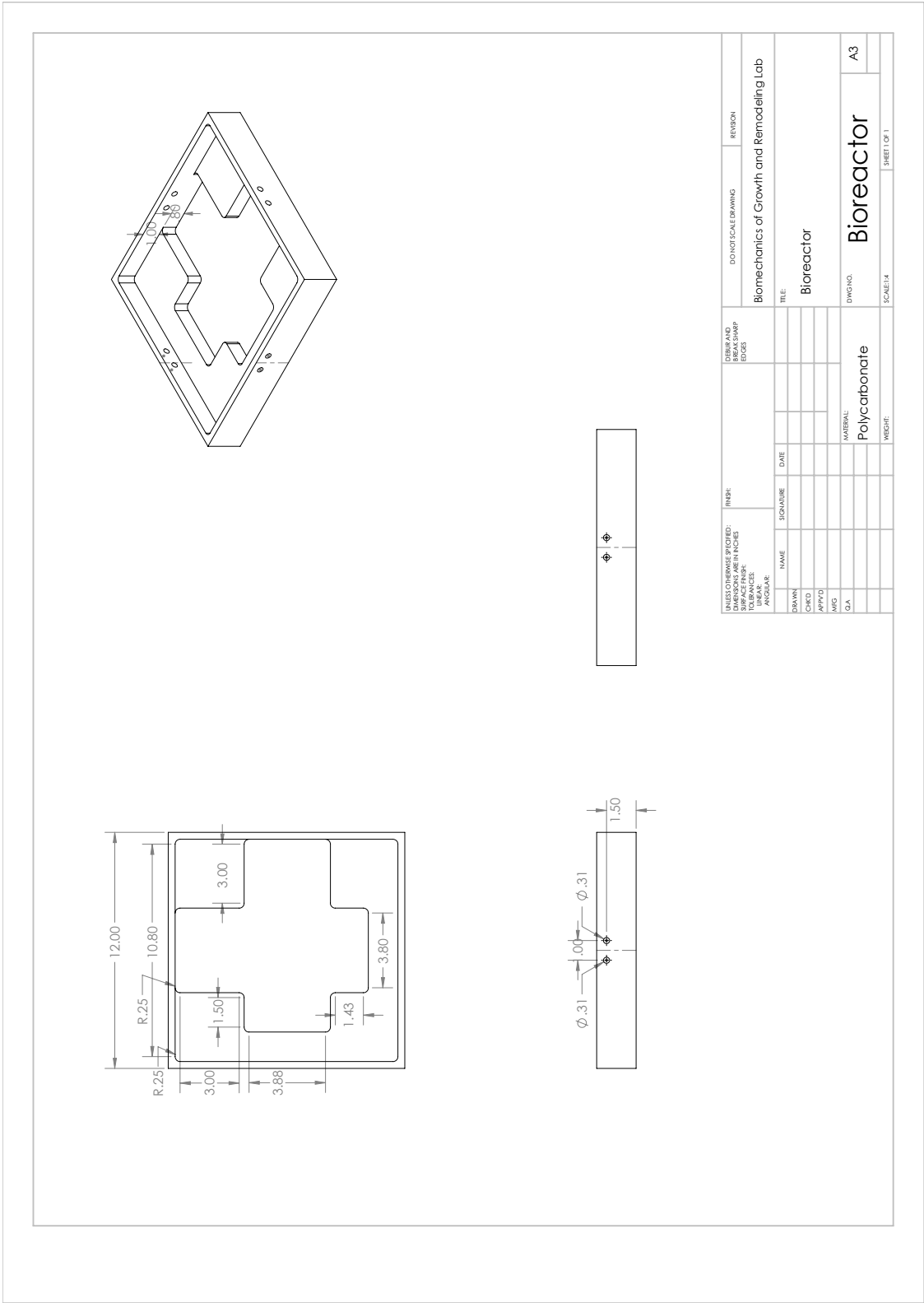
Model Number	Manta G-419 NIR
Imaging Device	CMOSIS CMV4000
Camera Sensor Format	1"
Type of Sensor	Progressive Scan CMOS
Sensing Area, H x V (mm)	11.3 x 11.3
Pixels (H x V)	2048 x 2048
Pixel Size, H x V (µm)	5.5 x 5.5
Pixel Depth	12 bit
Frame Rate (fps)	28.6
Camera Control	GigE Vision
Synchronization	External or Via Software
Exposure Control	Via Software
Video Output	GigE
Memory (MB)	32
Power Supply	via 12-Pin Hirose
Mount	C-Mount
Dimensions (mm)	86.4 x 44 x 29
Weight (g)	150
Resolution (MegaPixels)	4.2
Camera Family	Manta
Manufacturer	Allied Vision
Type	NIR Camera
CE Certified	Yes
RoHS	C

F. Planar Biaxial Device Custom Fabricated Parts Drawings

F1. Bioreactor Tank 7.5" x 7.5" version

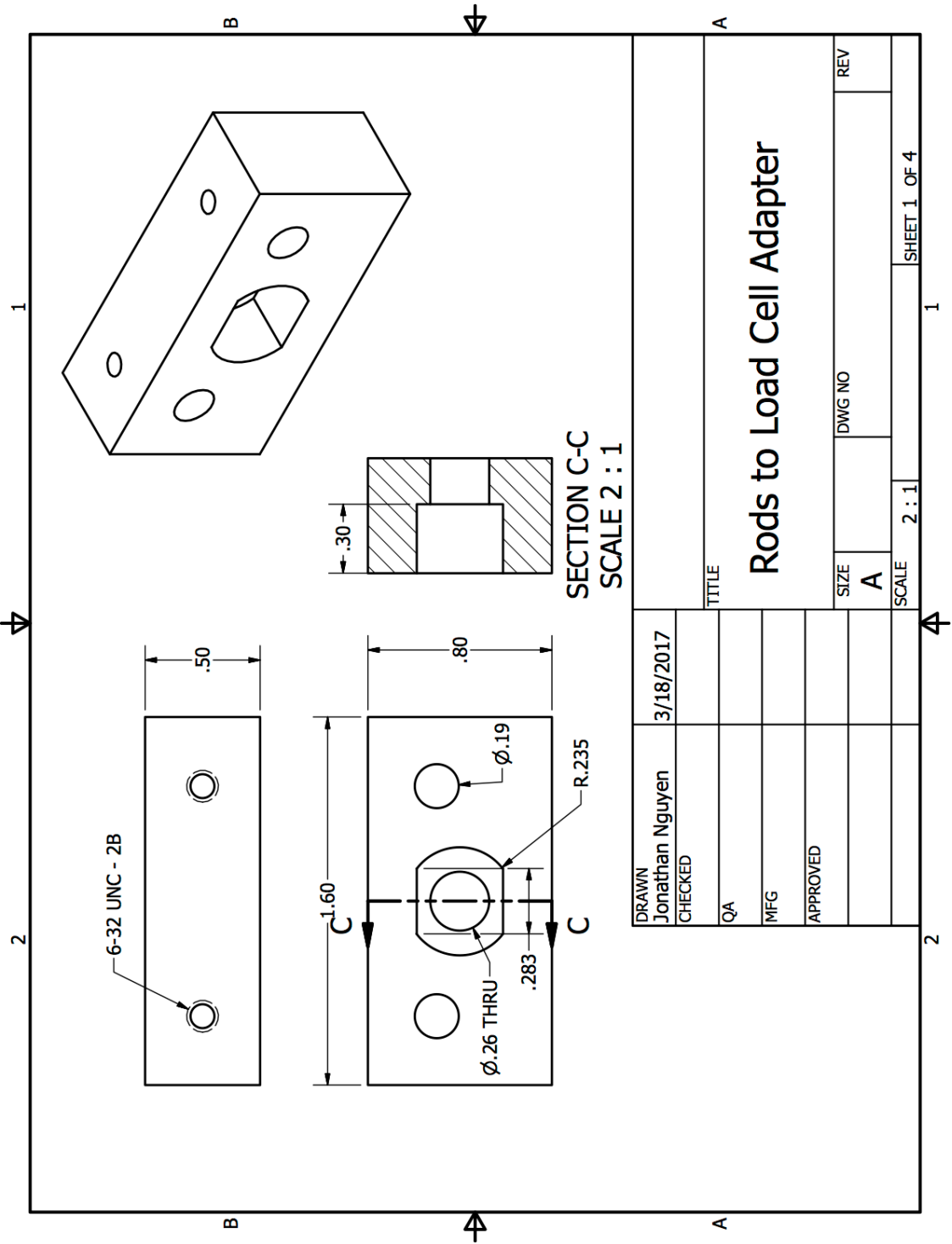


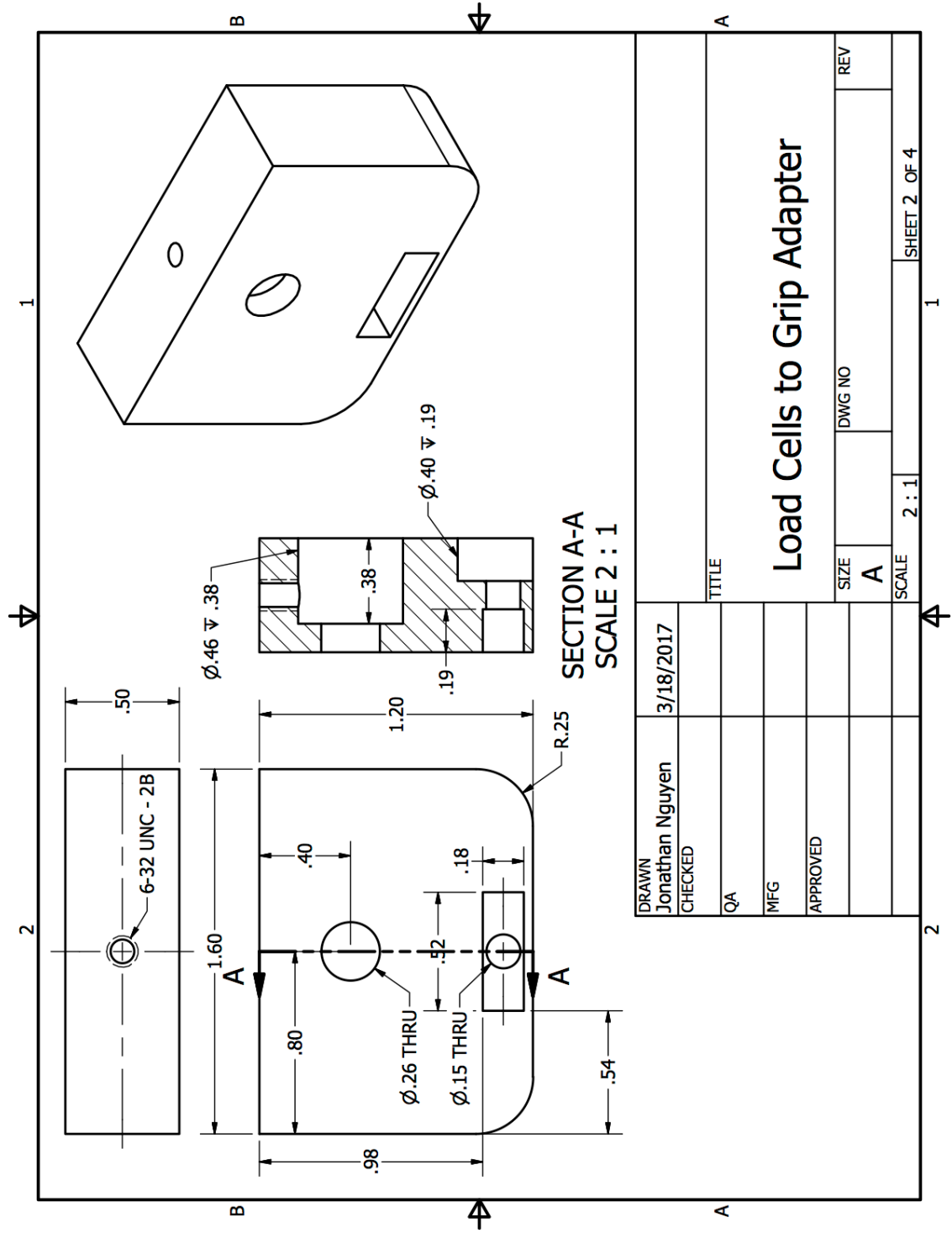
F2. Bioreactor Tank Version 12" x 12" version





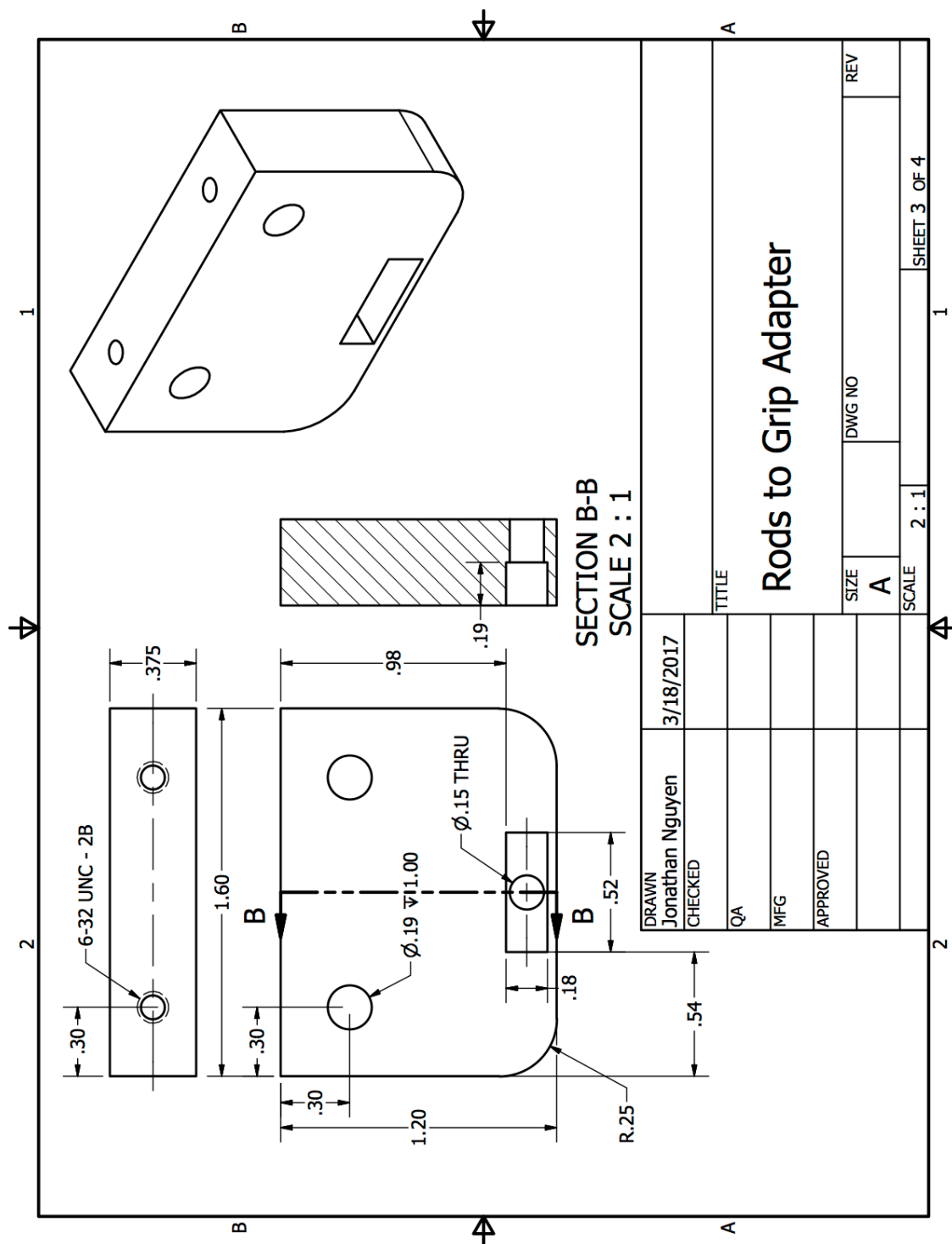
F4. Grip and Load Cell Holder for Model 34 Load Cells



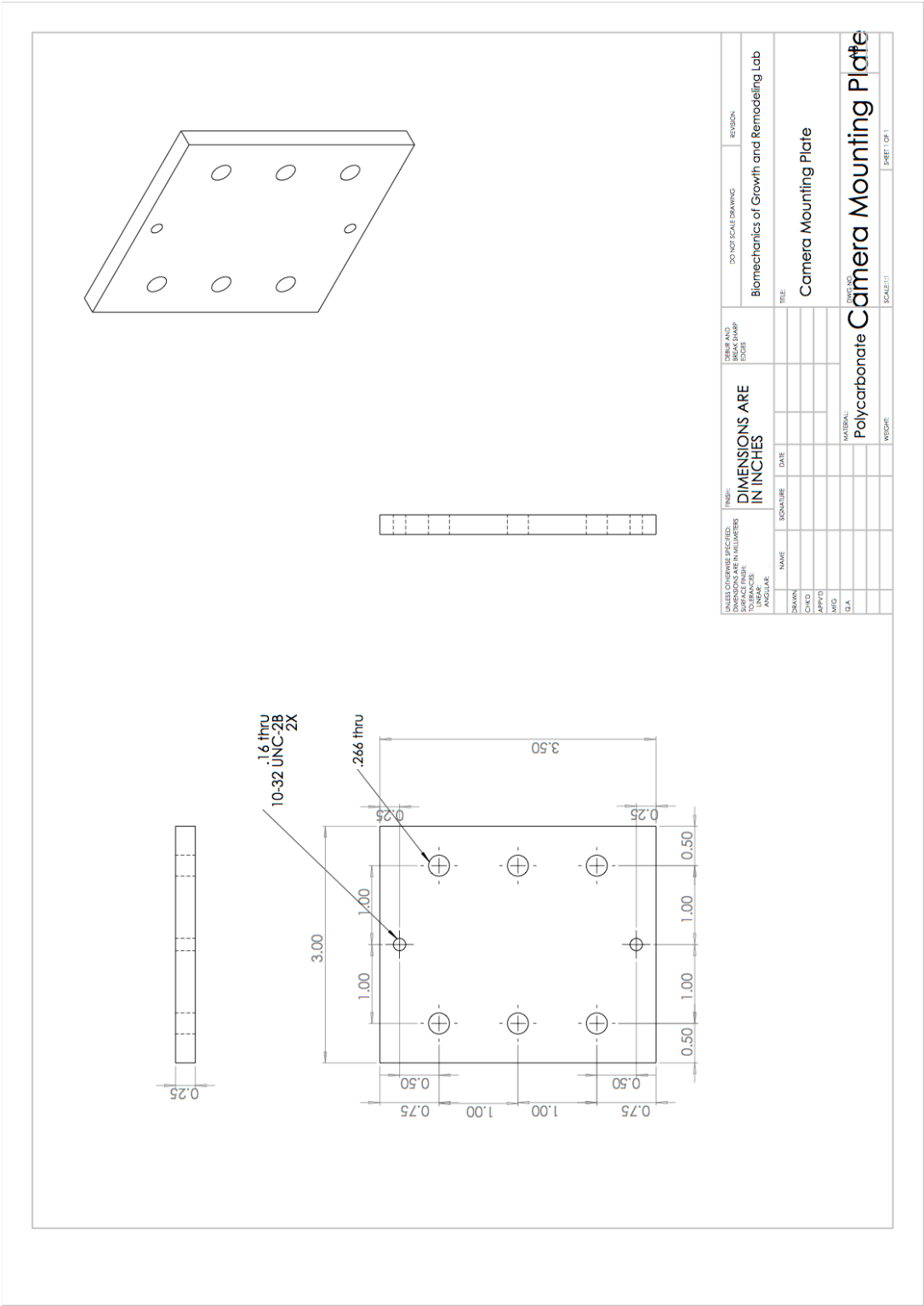


DRAWN	Jonathan Nguyen	3/18/2017	TITLE	
CHECKED				
QA				
MFG				
APPROVED				
			SIZE	DWG NO
			A	
			SCALE	2 : 1
			SHEET 2 OF 4	

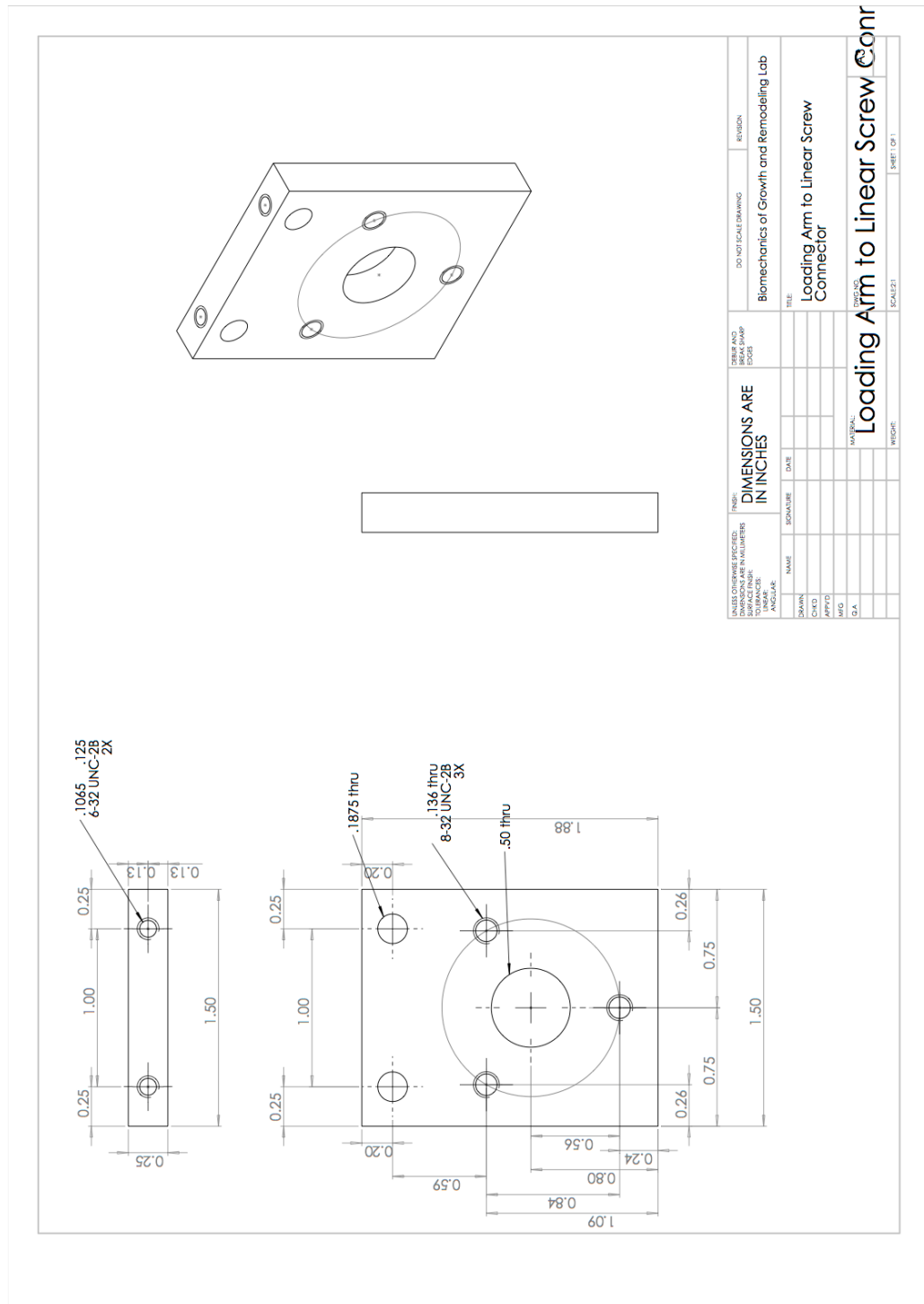
Load Cells to Grip Adapter



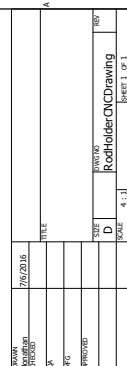
F5. Camera Mounting Plate

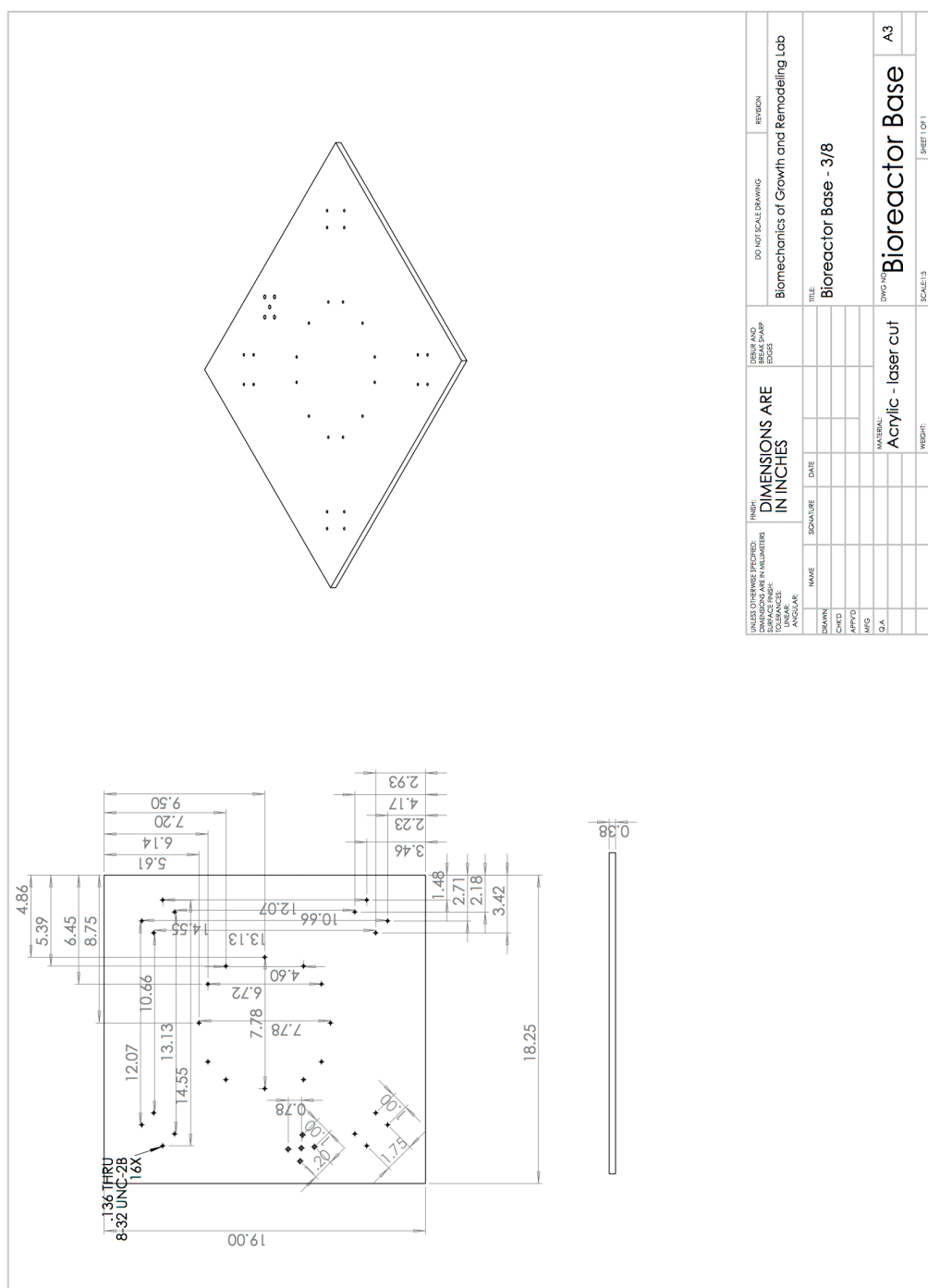


F6. Loading Arm to Linear Screw Connector Version 1

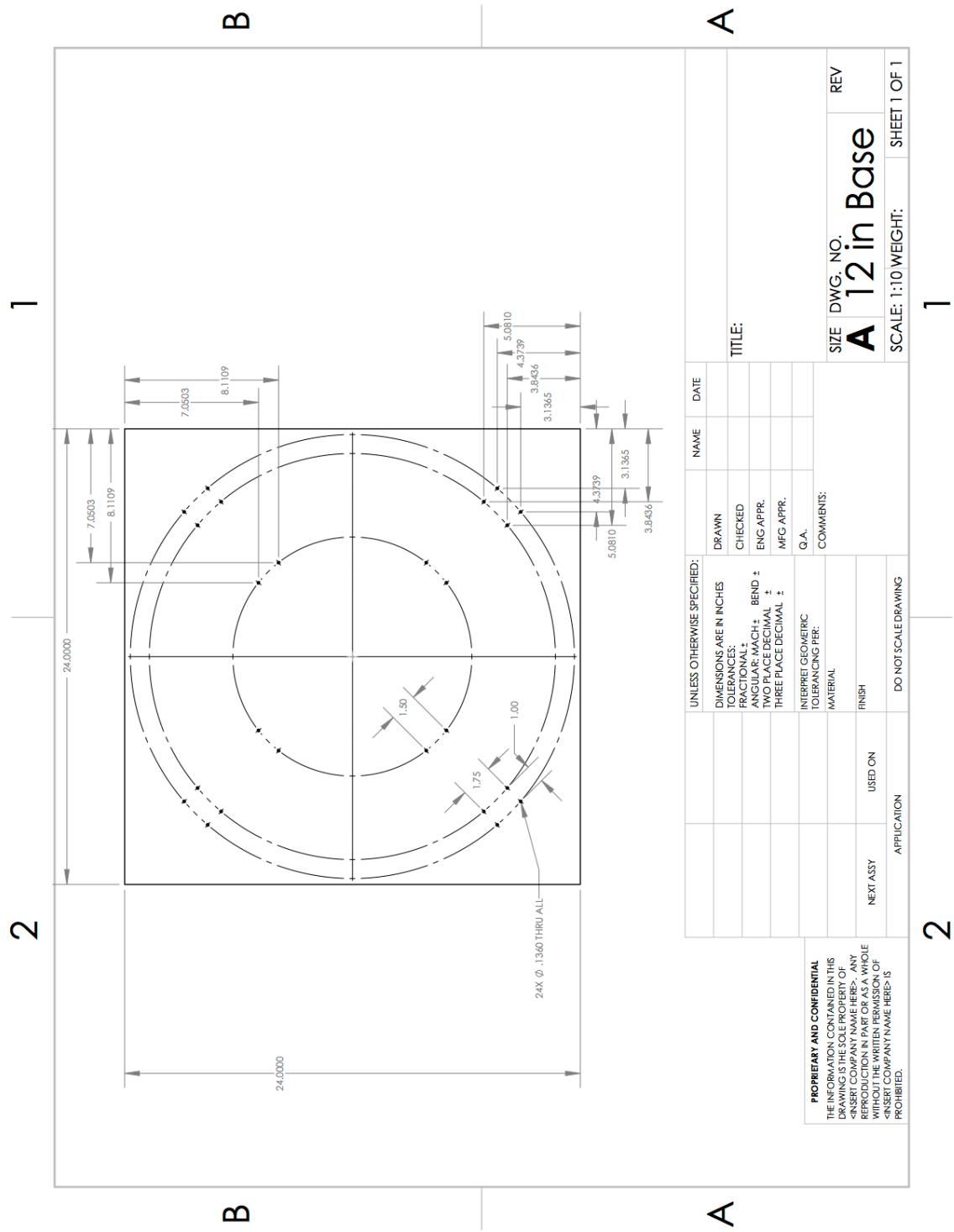


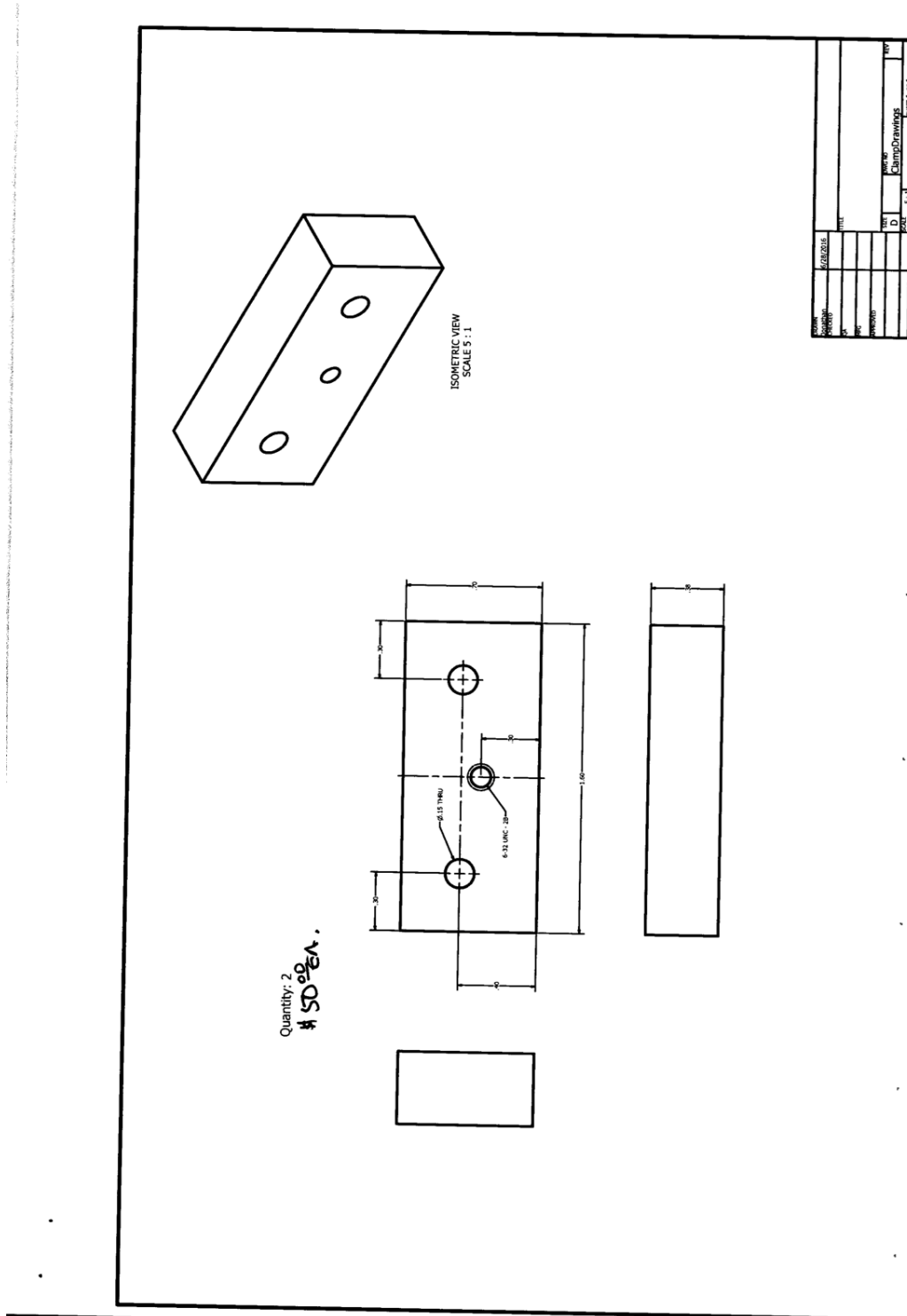
Note: This version makes it difficult to remove it from the device. Version 2 makes this process easier.

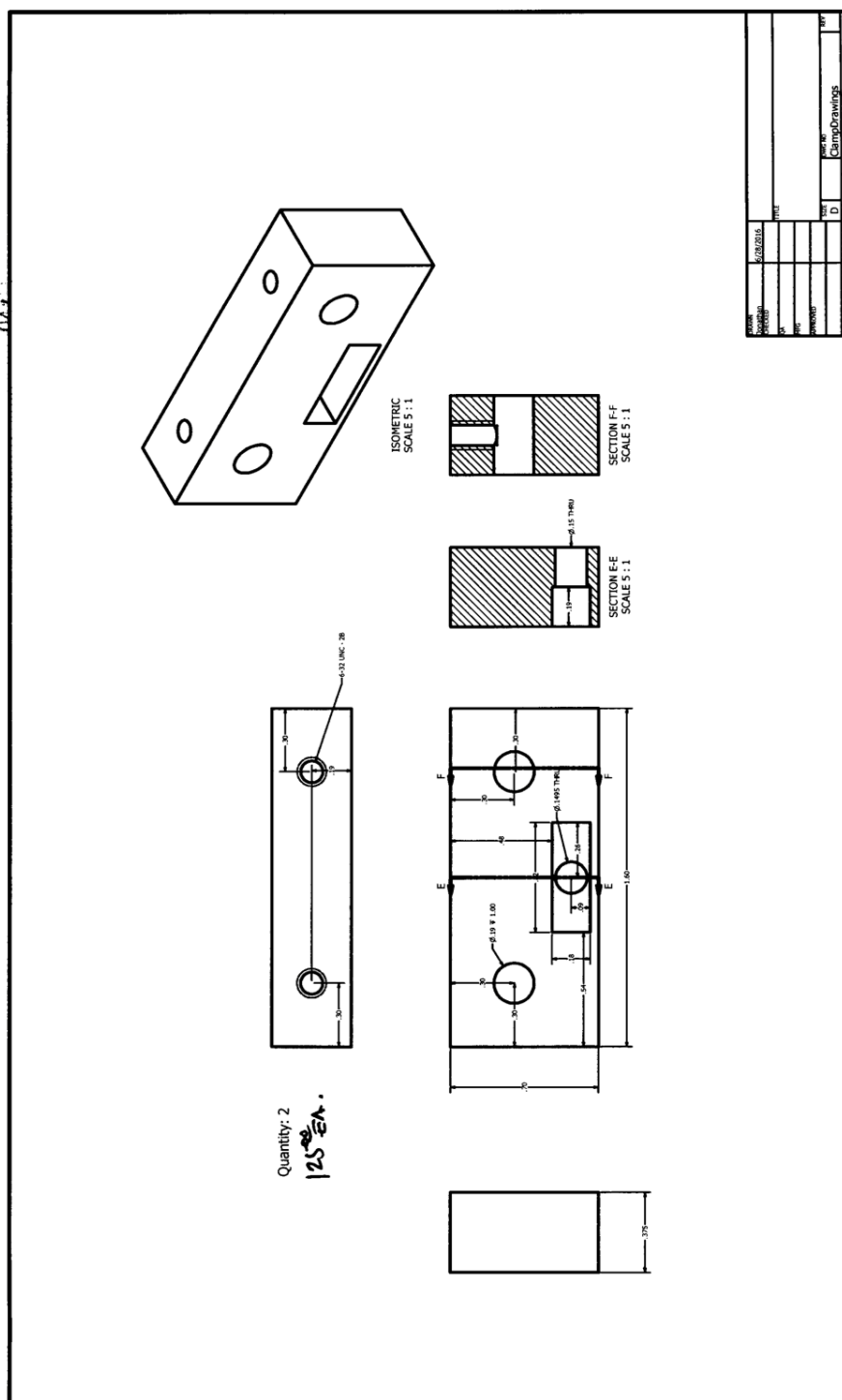




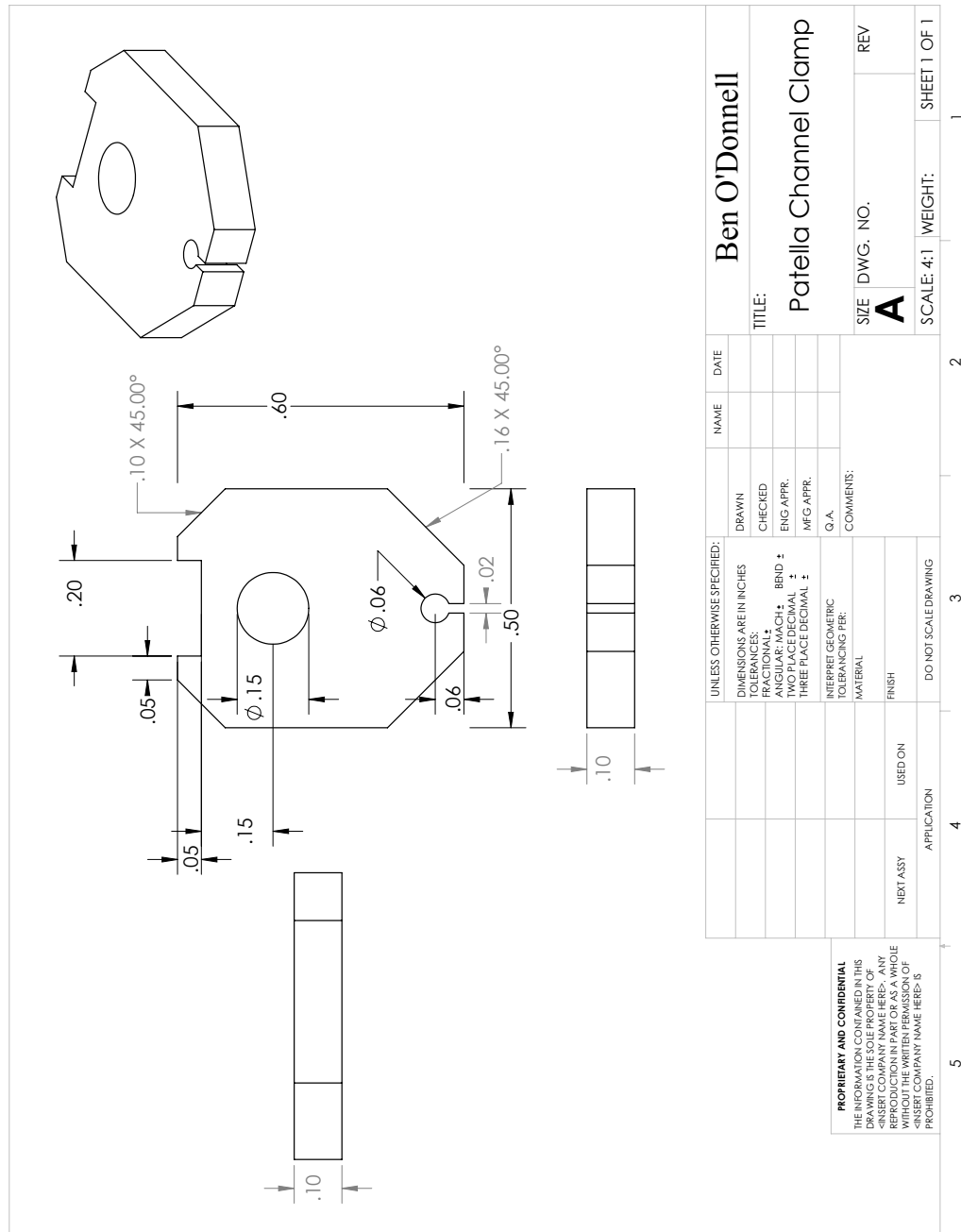
F9. Planar Biaxial Device Base for 12" x 12" tank









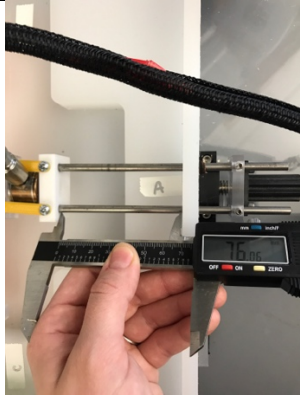
G2. Tendon Grips



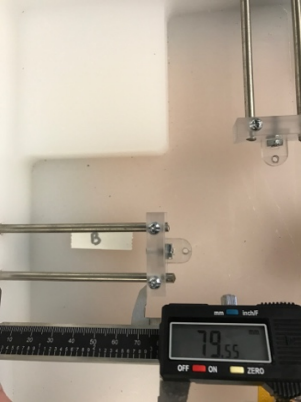


Note: Using three patellas, the average diameter of the mouse patella is between .9 and 1 mm which is approximately equal to .4 inches. Channel width is half the average diameter of the patellar tendons, .02 inches. Patella slot is 1.5 times patella width, .06 inches. Thickness of the entire piece was halved from the original to make it easier to slot the patella into the device.

H. Stepper Motor Validation



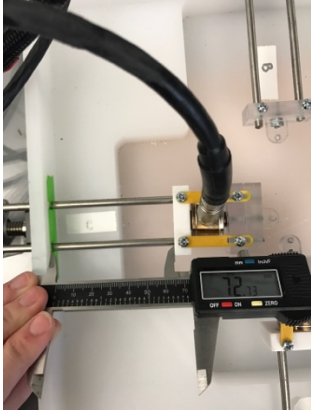
Motor A Validation

Before	After 25.4 mm Tension	After 25.4 mm Compression
 <p><i>76.04 mm</i></p>	 <p><i>50.85 mm</i> <i>0.82% error</i></p>	 <p><i>76.06 mm</i> <i>0.75% error</i></p>




Motor B Validation

Before	After 25.4 mm Tension	After 25.4 mm Compression
 <p><i>79.55 mm</i></p>	 <p><i>54.24 mm</i> <i>0.35% error</i></p>	 <p><i>79.33 mm</i> <i>1.22% error</i></p>



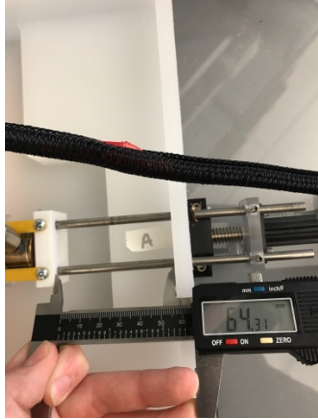



Motor C Validation

Before	After 25.4 mm Tension	After 25.4 mm Compression
 <p><i>72.73 mm</i></p>	 <p><i>47.54 mm</i> <i>0.83% error</i></p>	 <p><i>72.73 mm</i> <i>0.83% error</i></p>







Motor D Validation

Before	After 25.4 mm Tension	After 25.4 mm Compression
 <p><i>79.47 mm</i></p>	 <p><i>54.13 mm</i> <i>0.24% error</i></p>	 <p><i>79.48 mm</i> <i>0.20% error</i></p>







Motor A&B Validation




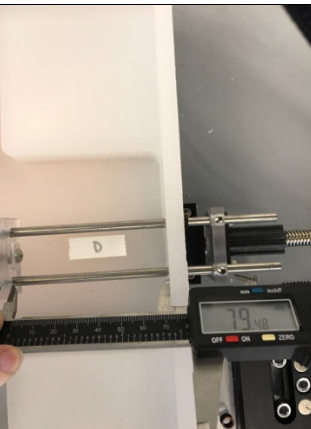
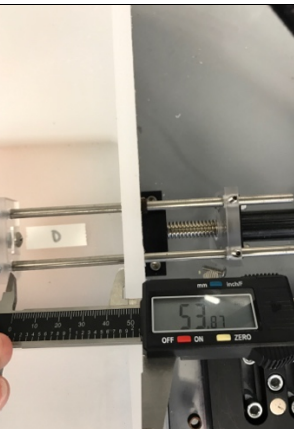

	Before	After 25.4 mm Tension	After 25.4 mm Compression
A	 <p><i>64.26 mm</i></p>	 <p><i>38.90 mm</i> <i>0.16% error</i></p>	 <p><i>64.31 mm</i> <i>0.04% error</i></p>
B	 <p><i>79.57 mm</i></p>	 <p><i>54.21 mm</i> <i>0.16% error</i></p>	 <p><i>79.54 mm</i> <i>0.28% error</i></p>

Motor C&D Validation

	Before	After 25.4 mm Tension	After 25.4 mm Compression
C	 <p><i>72.73 mm</i></p>	 <p><i>47.56 mm 0.91% error</i></p>	 <p><i>72.77 mm 0.75% error</i></p>
D	 <p><i>79.35 mm</i></p>	 <p><i>54.10 mm 0.59% error</i></p>	 <p><i>79.44 mm 0.24% error</i></p>

All Motors Validation

	Before	After 25.4 mm Tension	After 25.4 mm Compression
A	 <p><i>64.19 mm</i></p>	 <p><i>38.93 mm 0.55% error</i></p>	 <p><i>64.22 mm 0.43% error</i></p>
B	 <p><i>79.58 mm</i></p>	 <p><i>54.18 mm 0 % error</i></p>	 <p><i>79.61 mm 0.12% error</i></p>

C	 <p>72.76 mm</p>	 <p>47.53 mm 0.67% error</p>	 <p>72.74 mm 0.75% error</p>
D	 <p>79.48 mm</p>	 <p>53.87 mm 0.83% error</p>	 <p>79.55 mm 1.10% error</p>

I. Load Cell Calibration

II. Load Cell Calibration Protocol

1. Weigh the following objects and record their weights: box & string, 1 200 gram weight and 4 500 gram weights. Determine the exact weights for every step of the calibration process.
 - a. 0 grams ~ 0 pounds
 - b. 200 grams ~ 0.5 pounds
 - c. 500 grams ~ 1 pound
 - d. 700 grams ~ 1.5 pounds
 - e. 1000 grams ~ 2 pounds
 - f. 1200 grams ~ 2.5 pounds
 - g. 1500 grams ~ 3 pounds
 - h. 1700 grams ~ 3.5 pounds
 - i. 2000 grams ~ 4 pounds
 - j. 2200 grams ~ 4.5 pounds

2. Open a blank VI in LabVIEW. In the block diagram, search for “DAQ Assistant” and place it into the block diagram. Follow the prompts that pop up on the screen:
 - i) Acquire Signals
 - ii) Analog Input
 - iii) Bridge (V/V)
 - iv) cDAQmod1 (NI 9237)
 - v) ai0 and ai1 (select both by holding shift and then clicking on ai0 and ai1)

3. Set the following values on the configuration tab of the channel settings for each channel selected in step one (should be ai0 and ai1).
 - i) Signal Input Range
 - *Max: 25*
 - *Min: -25*
 - *Scaled Units: mV/V*
 - ii) Bridge type: *Full*
 - iii) Vex (excitation voltage) source: *Internal*
 - iv) Vex Value: *5 V DC*
 - v) Bridge Resistance: *500 Ω*

4. Under “Bridge (V/V) Setup”, select the calibration tab and click “calibrate.” This will start the channel calibration wizard
 - i) Input your name
 - ii) Expiration date (need to decide how long these calibrations will be good for)
 - iii) After calibration expires, *do not apply the calibration and return an error.*
 - iv) Acquisition Attributes
 - Number of samples to average: *25000*

- Sample rate (Hz): 25000
- v) Additional Information
- Load Cell: *X or Y*
 - Serial No: *X (1572180) or Y (1572181)*
5. Collect calibration measurement values. Tie string to box to place weights we have in lab (make sure to reweigh the weights after they are placed in the box) and box on the end of the load cell. Under the reference value, record the value for the weight of the weight itself and the string. Click “commit calibration value” and move onto the next weight. Allow five minutes between placing the weight at the end of the load cell and clicking “commit calibration value” so the uncalibrated voltage value can stabilize. Begin with no weight at the end of the load cell, and then increase the weight by the list in step 1 until you reach 2200 grams. While unloading the weights after reaching 2200 grams, allow 5 minutes for the load cell to equilibrate. Move back down the list in step one every time until you reach zero weight.
6. Open the excel file titled “Load Cell Calibration Template”. Copy and paste the load cell calibration data from the most recent calibration, and generate its chart and trend line. Input the weights and voltage values calculated and obtained throughout the calibration in the upper section of the sheet (you can fill this out as you go).

I2. Load Cell Calibration Graphs and Data (Model 34)

I2.1 Load Cell X-Axis

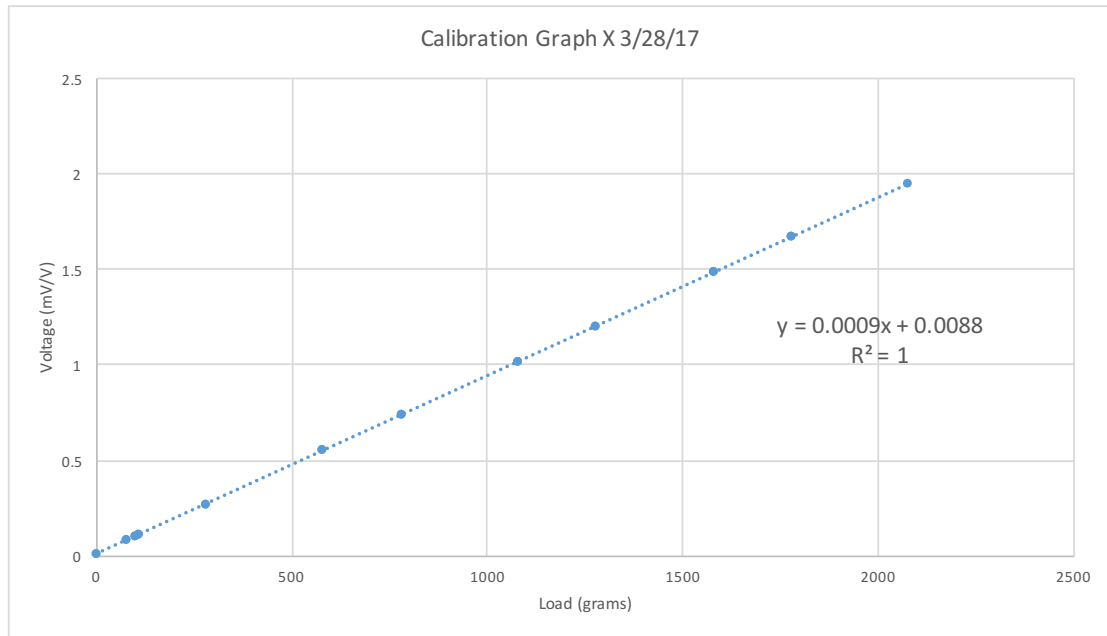


Figure I2.1: Load Cell X Calibration Graph

Load (g)	Voltage (mV/V)
0	0.01
78.97	0.08
98.98	0.10
109.01	0.12
279.04	0.27
579.07	0.55
779.14	0.74
1079.2	1.02
1279.27	1.20
1579.33	1.48
1779.4	1.67
2079.48	1.95
1779.4	1.67
1579.33	1.48
1279.27	1.20
1079.2	1.02
779.14	0.74
578.07	0.55
279.04	0.27
109.01	0.11
98.98	0.10
78.97	0.08
0	0.09

I2.2 Load Cell Y-Axis

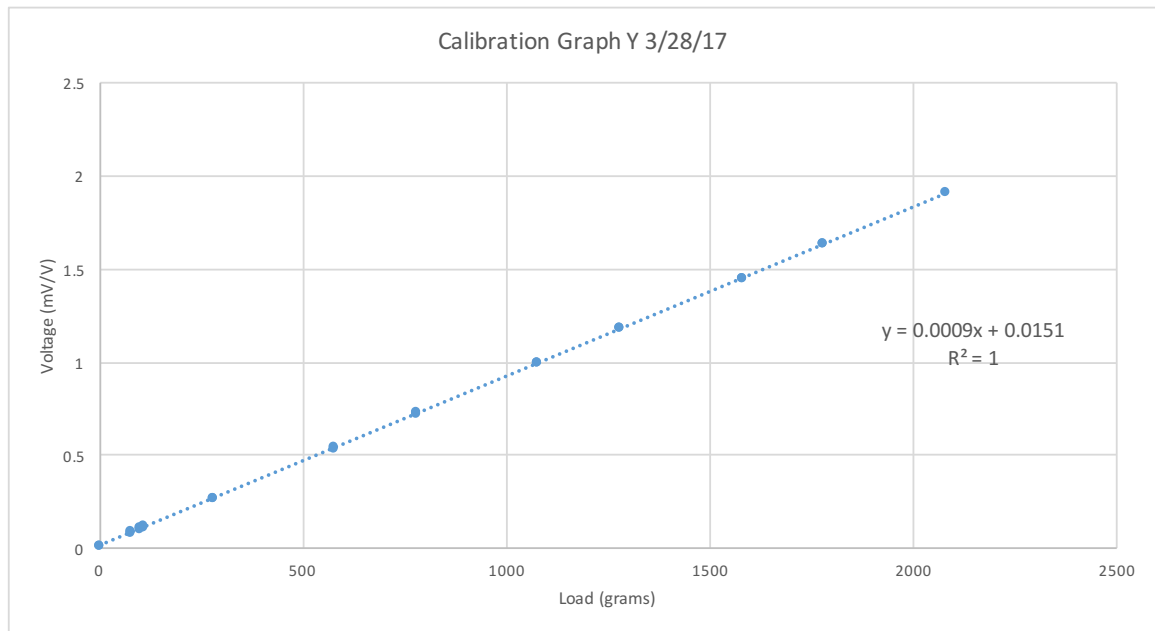


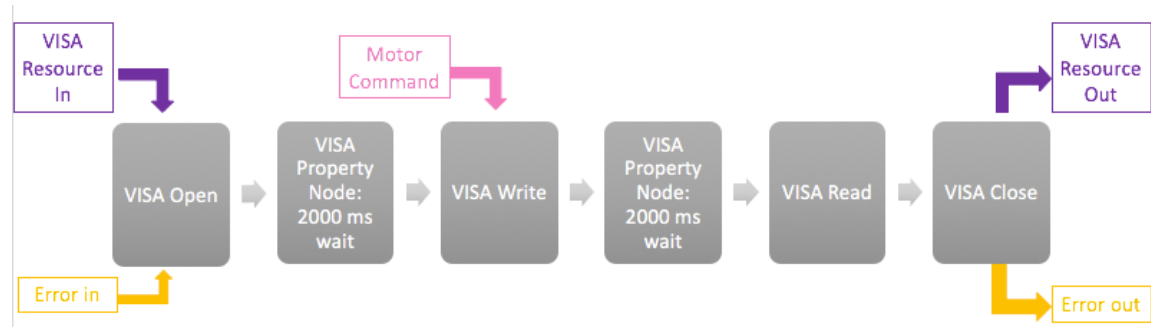
Figure I2.2: Load Cell Y Calibration

Load (g)	Voltage (mV/V)
0	0.02
78.97	0.08
98.98	0.10
109.01	0.11
279.04	0.27
579.07	0.54
779.14	0.72
1079.2	1.00
1279.27	1.18
1579.33	1.45
1779.4	1.63
2079.48	1.90
1779.4	1.63
1579.33	1.45
1279.27	1.18
1079.2	1.00
779.14	0.73
578.07	0.54
279.04	0.27
109.01	0.12
98.98	0.11
78.97	0.09
0	0.02

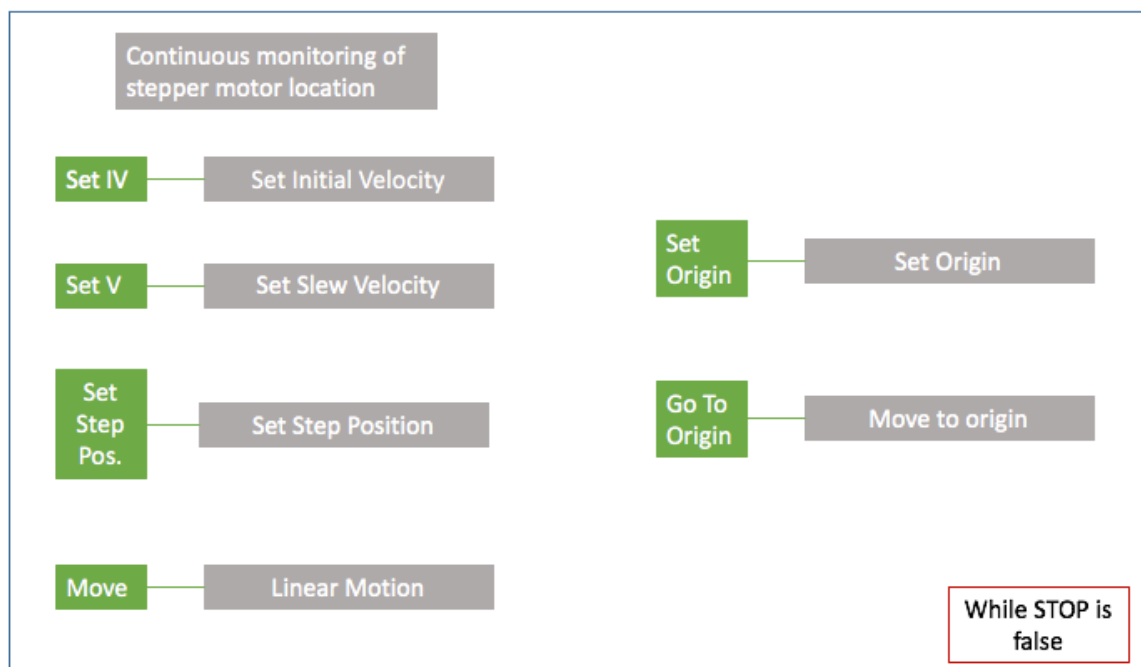
J. LabVIEW Code

J1. Motion Control Code

J1.1 Basic VISA Commands Code Flow Chart

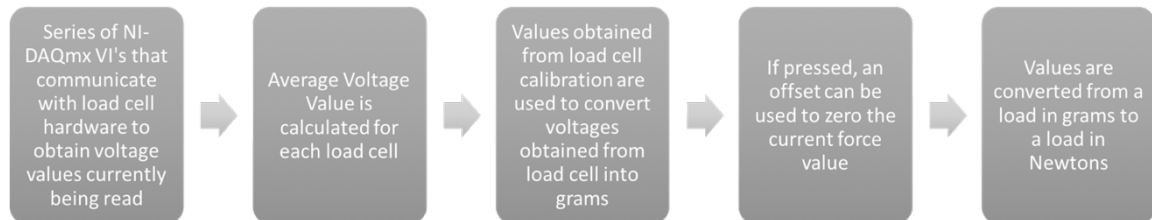


J1.2 Motion Control Panel Code Flow Chart

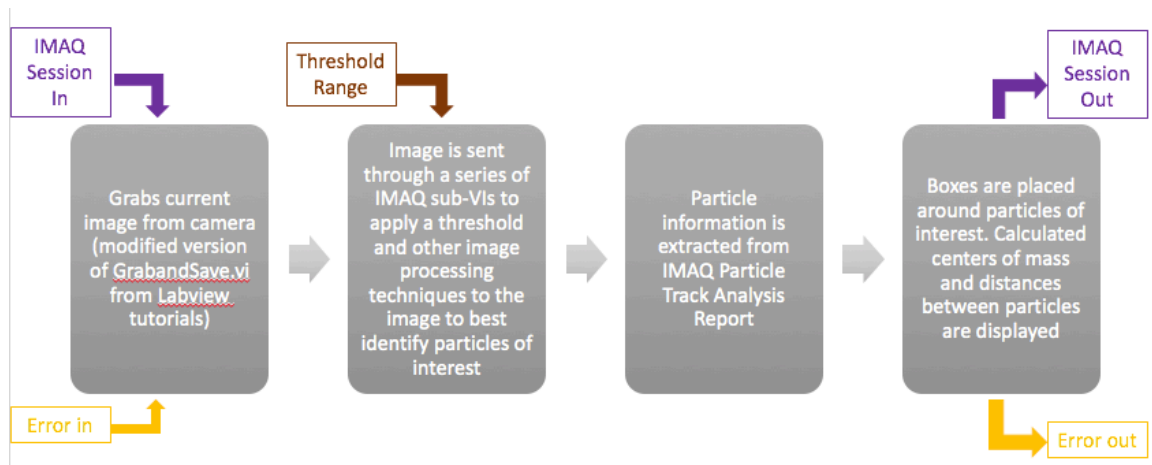


Note: Set Initial Velocity, Set Slew Velocity, Set Step Position, Linear Motion, Set Origin, and Move to Origin are sub-VIs that contain the basic VISA commands code shown in Appendix J1.1

J2. Data Acquisition Code

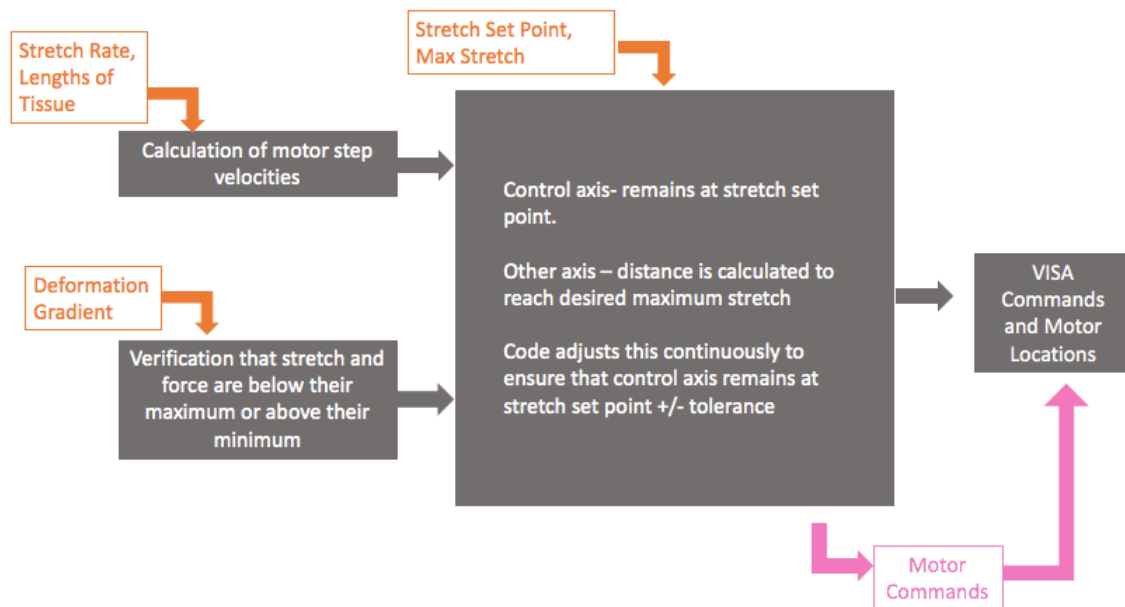


J3. Image Acquisition Code

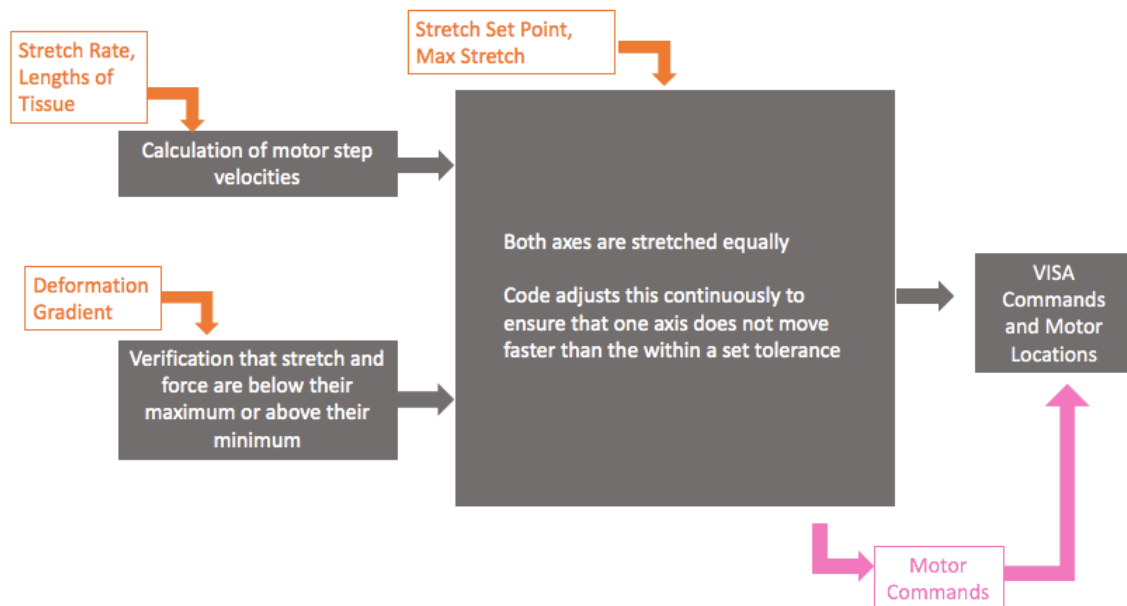


J4. Mechanical Test Code

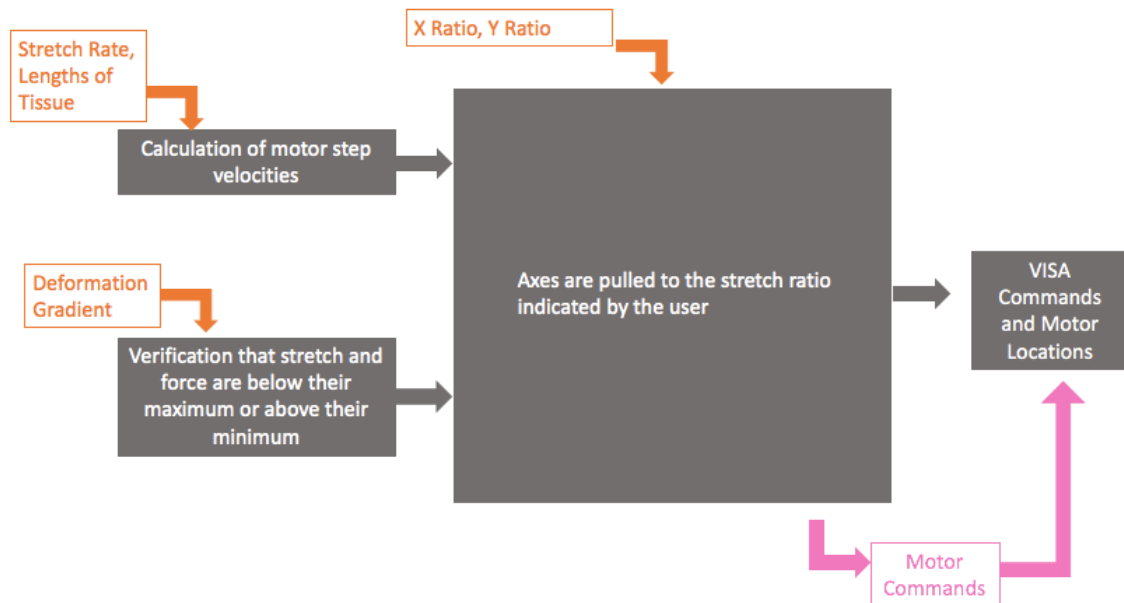
J4.1 Constant Stretch Mechanical Testing Protocol Code Flow Chart



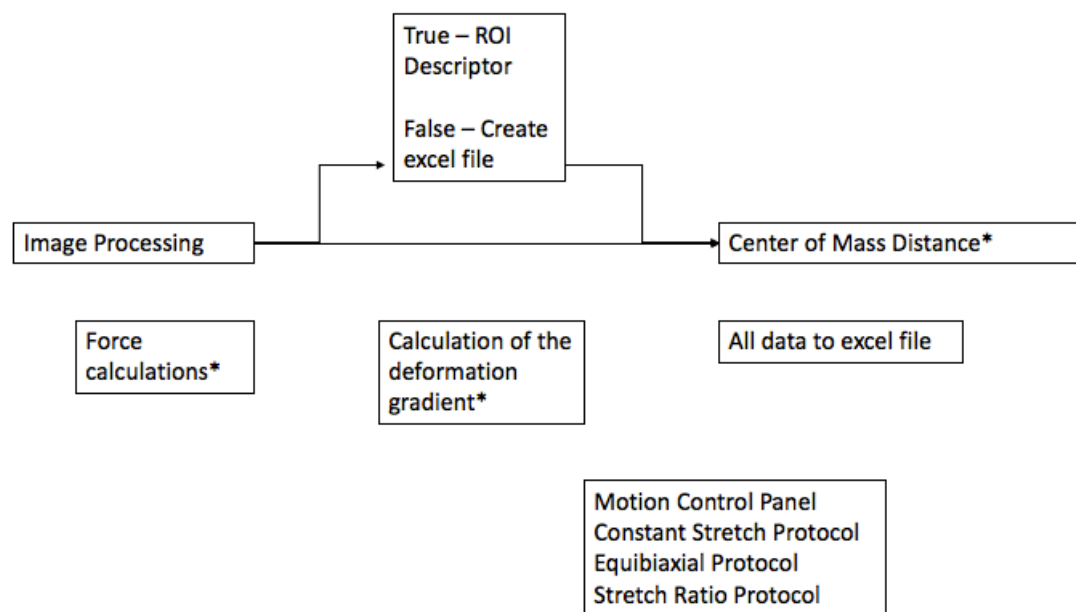
J4.2 Equibiaxial Mechanical Testing Protocol Code Flow Chart



J4.3 Stretch Ratios Mechanical Testing Protocol Code Flow Chart



J4.4 Mechanical Test Code Flow Chart



K. Load Cell Literature Search Tables

Tendons

<i>Paper</i>	<i>Load Cell Range</i>	<i>Load Cell Model (if given)</i>	<i>Misc. Notes</i>
Dunkman, et. al. 2012. Decorin Expression is Important for Age-Related Changed in Tendon Structure and Mechanical Properties	10 N		same as other 3 papers included in Soslowsky PT study
O'Connel, et. al. 2013. "Human Annulus Fibrosis Material Properties from Biaxial Testing and Constitutive Modeling are Altered with Degeneration.	5 lb (?), range varies for this model of load cell.	Model #41 Honeywell	device used by Spence Szczesny in "Biaxial Tensile Testing and Constitutive Modeling of Human Supraspinatus Tendon" paper
Davis and De Vita, 2012. "A Nonlinear Constitutive Model for Stress Relaxation in Ligaments and Tendons"	8.9 N	LSB, 200, Futek	Rat tail tendon fascicles
Connizzo, Brianne K., et al. "Diabetes alters mechanical properties and collagen fiber re-alignment in multiple mouse tendons." <i>Annals of biomedical engineering</i> 42.9 (2014): 1880-1888.	~30 N - failure load		Had to estimate failure load from graphs given in paper
Robinson, Paul S., et al. "Influence of decorin and biglycan on mechanical properties of multiple tendons in knockout mice." <i>Journal of biomechanical engineering</i> 127.1 (2005): 181-185.	~5 N failure load		Had to estimate failure load from graphs given in paper, might be same device used in Dunkman papers?

Uterosacral Ligament

<i>Paper</i>	<i>Load Cell Range</i>	<i>Load Cell Model (if given)</i>	<i>Misc. Notes</i>
Becker and De Vita, 2014. Biaxial mechanical properties of swine uterosacral and cardinal ligaments	20 N		planar biaxial tests
Tan, et. al. 2015 Histomechanical Properties of Swine CL and USL	50 N		uniaxial tests
Tan, et. al. 2016 Micro-structural and Biaxial Creep Properties of the Swine Uterosacral Cardinal Ligament Complex	20 N		planar biaxial tests, follow up to Tan 2015 paper

Uterus

<i>Paper</i>	<i>Load Cell Range</i>	<i>Load Cell Model (if given)</i>	<i>Misc. Notes</i>
Omari, et. al. 2015 Dynamic and Quasi-Static Mechanical Testing for Characterization of the Viscoelastic Properties of Human Uterine Tissue	1000 g	EnduraTEC ELF 3200 Mechanical Testing System	

Vagina

<i>Paper</i>	<i>Load Cell Range</i>	<i>Load Cell Model (if given)</i>	<i>Misc. Notes</i>
Abramowitch data from Jason	115.4 g (max force)		see sheet from Jason in notebook
Cosson, et. al. 2003 A biomechanical study of the strength of vaginal tissues: results on 16 post-menopausal patients presenting with genital prolapse	76.33 N (max tensile force) 44.28 N (average tensile force)		
Rubod, et. al. 2008 Biomechanical Properties of Vaginal Tissue: Preliminary Results	1 kN		we probably don't need that high of a range

Cervix

<i>Paper</i>	<i>Load Cell Range</i>	<i>Load Cell Model (if given)</i>	<i>Misc. Notes</i>
Barone, et. al. 2007 The effect of pregnancy and postpartum recovery on the viscoelastic behavior of the rat cervix	50 lbs		Not sure if we really need this much

L. Patellar Tendon Dissection Protocol

Materials:

Scalpel Handle #3
Scalpel Blades # 15
Micro Scissors
Wagner Scissors
Forceps
Gauze Pad
HBBS: ~50 ml

Procedure:

1. Skin hind leg from ankle to pass the hip
2. Following the quadriceps, cut away the hind leg, removing the femoral head from its socket.
3. Starting at the Achilles tendon, cut away the muscle from the posterior side of the shank and the femur.
4. Being careful to not injure the patellar tendon, cut away the muscle on the sides of the femur, leaving just the quadriceps.
5. Starting at the femoral head, cut the quadriceps away from the femur until the femoral condyles are completely revealed.
6. Cut away the femur.
7. Looking from posterior to anterior, find the Patella. Cut around the Patella; be careful not to cut the patellar tendon, cutting away the quadriceps.
8. Carefully remove tissue around the patellar tendon insert into the tibia.
9. Cut the tibia tuberosity, leaving the patellar tendon still connected to bone
10. Use Micro Scissors to clean connecting tissue
11. Wet the Gauze with HBBS. Wrap the patellar tendon with the gauze.

M. Patellar Tendon Study – Animal Group Composition

Species	Procedures	USDA Pain Category	# of Animals
Mouse, C57/BL/6, Female	Euthanasia (CO ₂ Inhalation), RNA Sequencing and Biochemical Analysis. Since all animals in this group are controls, they will be euthanized 4.5 weeks following the injury time point. This data will evaluate key matrix adaptation mechanisms of patellar tendon aging. <ul style="list-style-type: none"> • Mature, 120 days (n=5) • Aging, 270 days (n=5) • Aged, 540 days (n=5) 	C	15
Mouse, C57/BL/6, Male	Euthanasia (CO ₂ Inhalation), Biomechanical Testing, Histomorphologic and Biochemical Analysis. Since all animals in this group are controls, they will be euthanized 4.5 weeks following the injury time point. This data will establish baseline age-related mechanical characteristics. <ul style="list-style-type: none"> • Mature, 120 days (n=11) <ul style="list-style-type: none"> ○ Biomechanical Testing (n=11), right or left hindlimb from all animals ○ Histomorphologic and Biochemical Analysis (n=5), remaining hindlimb split between assays • Aging, 270 days (n=11) <ul style="list-style-type: none"> ○ Biomechanical Testing (n=11), right or left hindlimb from all animals ○ Histomorphologic and Biochemical Analysis (n=5), remaining hindlimb split between assays • Aged, 540 days (n=11) <ul style="list-style-type: none"> ○ Biomechanical Testing (n=11), right or left hindlimb from all animals ○ Histomorphologic and Biochemical Analysis (n=5), remaining hindlimb split between assays 	C	33
Mouse, C57/BL/6, Male	Euthanasia (CO ₂ Inhalation), Patellar Tendon Biopsy Punch, Biomechanical Testing, Histomorphologic and Biochemical Analysis. Since all animals in this group are in the experimental groups, they will be euthanized at either 3 or 6 weeks following the injury time point. This data will establish baseline age-related mechanical characteristics due to injury. <ul style="list-style-type: none"> • Mature, 120 days (n=22) <ul style="list-style-type: none"> ○ 3 Weeks Post-Injury Euthanasia (n=11) <ul style="list-style-type: none"> ▪ Biomechanical Testing (n=11), right or left hindlimb from all animals ▪ Histomorphologic and Biochemical Analysis (n=5), remaining hindlimb split between assays ○ 6 Weeks Post-Injury Euthanasia (n=11) <ul style="list-style-type: none"> ▪ Biomechanical Testing (n=11), right or left hindlimb from all animals ▪ Histomorphologic and Biochemical Analysis (n=5), remaining hindlimb split between assays • Aging, 270 days (n=22) <ul style="list-style-type: none"> ○ 3 Weeks Post-Injury Euthanasia (n=11) 	D	66

	<ul style="list-style-type: none"> ▪ Biomechanical Testing (n=11), right or left hindlimb from all animals ▪ Histomorphologic and Biochemical Analysis (n=5) , remaining hindlimb split between assays ○ 6 Weeks Post-Injury Euthanasia (n=11) <ul style="list-style-type: none"> ▪ Biomechanical Testing (n=11), right or left hindlimb from all animals ▪ Histomorphologic and Biochemical Analysis (n=5) , remaining hindlimb split between assays • Aged, 540 days (n=22) <ul style="list-style-type: none"> ○ 3 Weeks Post-Injury Euthanasia (n=11) <ul style="list-style-type: none"> ▪ Biomechanical Testing (n=11), right or left hindlimb from all animals ▪ Histomorphologic and Biochemical Analysis (n=5) , remaining hindlimb split between assays ○ 6 Weeks Post-Injury Euthanasia (n=11) <ul style="list-style-type: none"> ▪ Biomechanical Testing (n=11), right or left hindlimb from all animals ▪ Histomorphologic and Biochemical Analysis (n=5) , remaining hindlimb split between assays 		
--	--------------------------------------------------------------------------------------------------------------------------------------------------------------------------------------------------------------------------------------------------------------------------------------------------------------------------------------------------------------------------------------------------------------------------------------------------------------------------------------------------------------------------------------------------------------------------------------------------------------------------------------------------------------------------------------------------------------------------------------------------------------------------------------------------------------------------------------------------------------------------------------------------------------------------------------------------------------------------------------------------------------------------------------------------------------------------------------------------------------------------------------------------------------	--	--

N. Patellar Tendon Biopsy Punch Surgery Protocol

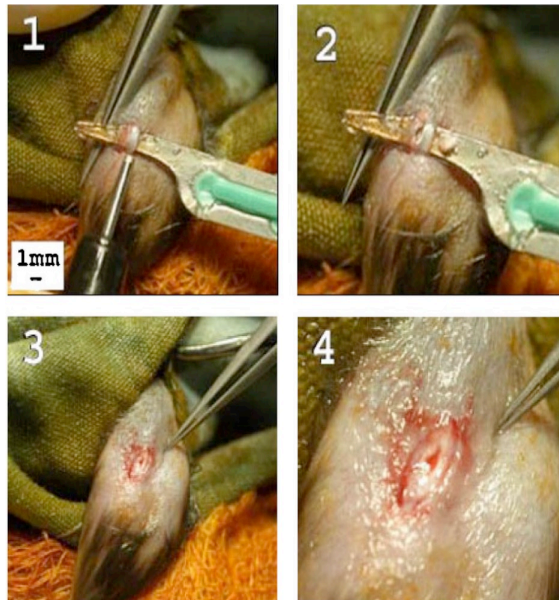


Figure N1: Briefly, following incision in the skin and two incisions along the sides of the patellar tendon, a rubber coated backing will be slipped underneath the tendon (1). A 0.75mm biopsy punch will be used to create a full thickness, partial width defect injury in the center portion of the patellar tendon (2-4). Then, the skin will be sutured, animals returned to normal cage activity, and euthanized 3 or 6 weeks after surgery. Figure from [113].

1. A few days before surgery, two sets (1 for use, 1 for back-up) of surgical instruments will be sterilized using an autoclave. In between animals, surgical instruments will be sterilized using a dry glass bead sterilizer heated to 250°C.
2. Mice will be administered one does of meloxicam as a pre- and post-operative analgesia.
3. In preparation for the surgical procedure, mice will be placed under a heating lamp and initially be anesthetized with isoflurane (4-5%) via induction chamber. Both hind limbs will be shaved, artificial tears ointment will be placed over their eyes, and chlorhexidine or betadine with alcohol will be used to sterilize the skin. Throughout the procedure, mice will be anesthetized with isoflurane inhalant (1-2%) via a fitted nose cone. The appropriate depth of anesthesia will be maintained by regular assessments of respiratory rate and toe pinch reflexes. Sterile gloves and masks will be worn by all personnel throughout the duration of the surgery.
4. The mice will be placed in a supine position in the knee in a flexed position. A skin incision medial to the knee will be made, and the skin pulled aside to expose the patellar tendon.
5. Two cuts parallel to the tendon will be made in the retinaculum on each side, and a plastic coated blade will then be placed underneath the patellar tendon.

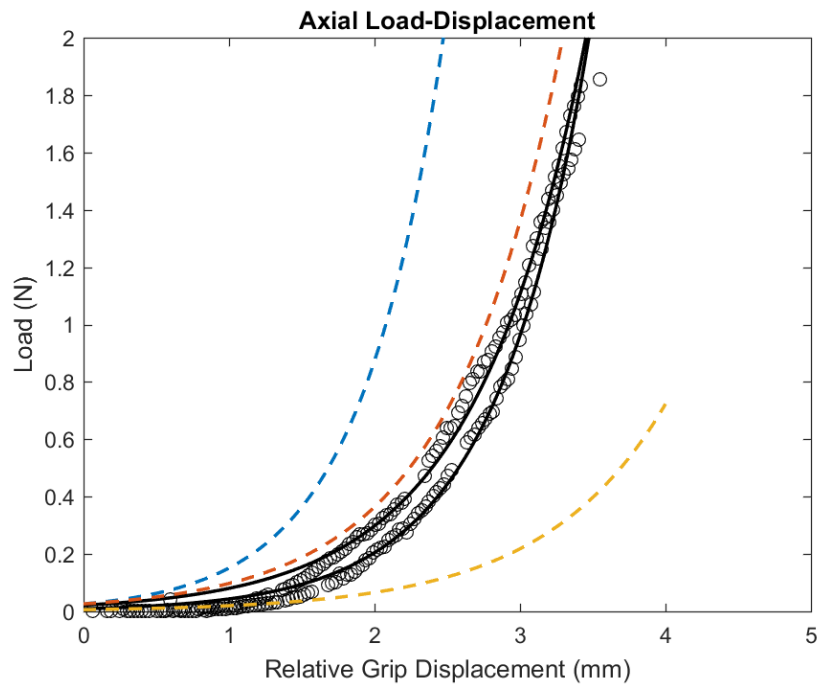
6. With the coated blade serving as support, a 0.75 mm diameter biopsy punch will be used to create a full thickness partial transection in both the left and right patellar tendon. A magnified view will be used to show the marginal fibers on each side of the injury, which circumvent the need for suture repair and also allow for immediate post-operative tendon mobilization.
7. The skin will be closed using a 4-0 prolene suture.
8. Steps 4-7 will be repeated for the adjacent hindlimb.
9. The mice will be allowed to recover from the anesthesia under a heating lamp (~30 minutes). After recovery, the mice will be moved back into their cages to resume normal activity.
10. Sutures will be removed 7-10 days following surgery.
11. Animals will be closely monitored for pain and distress for the remainder of the study.

O. Murine Skin Pilot Study Data

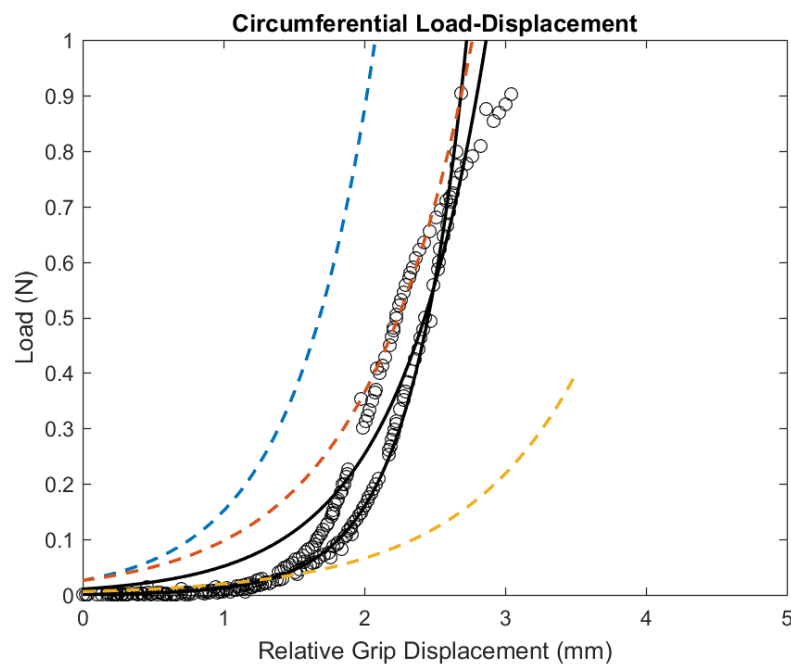
O.1 Load Displacement Curves Against Groves, et. al. Data [34]

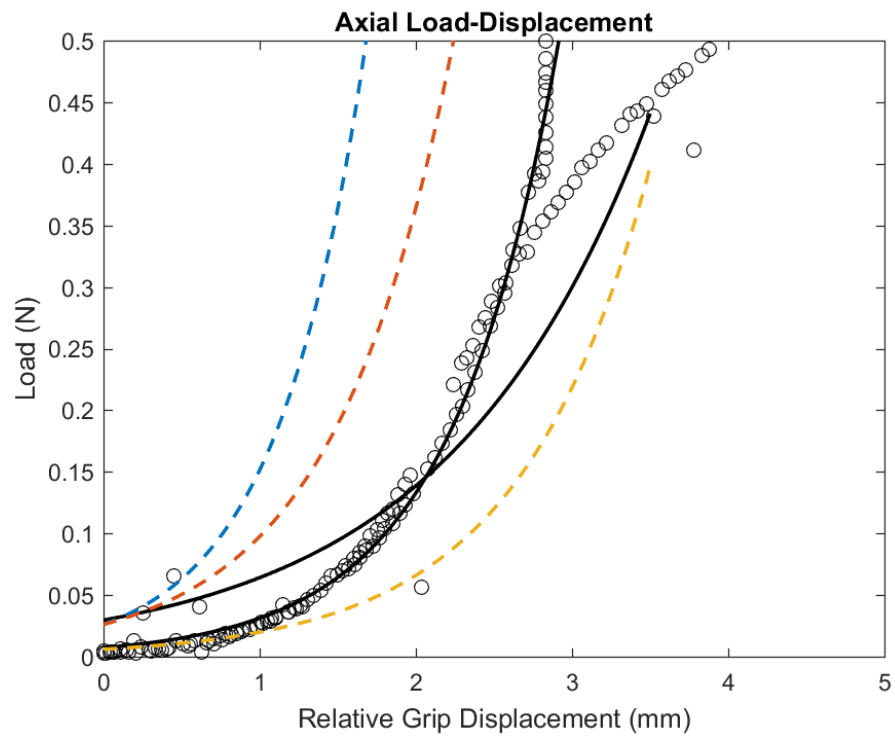
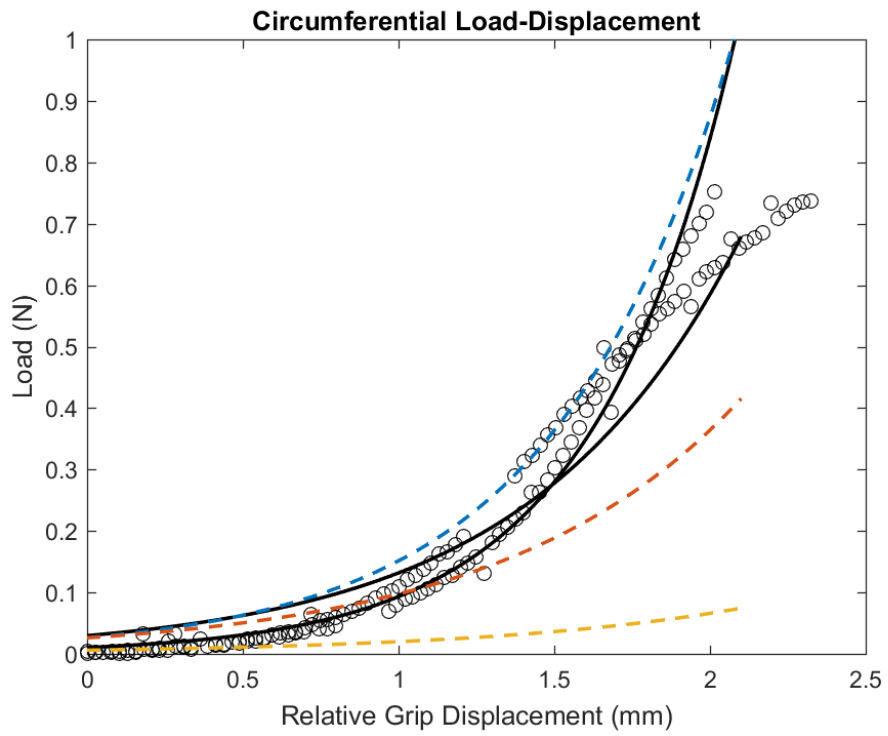
*Black lines with open circles represent experimental data. Blue, yellow, and red lines represent measurements taken at 0, 45, and 90 degrees, respectively by Groves et. al.

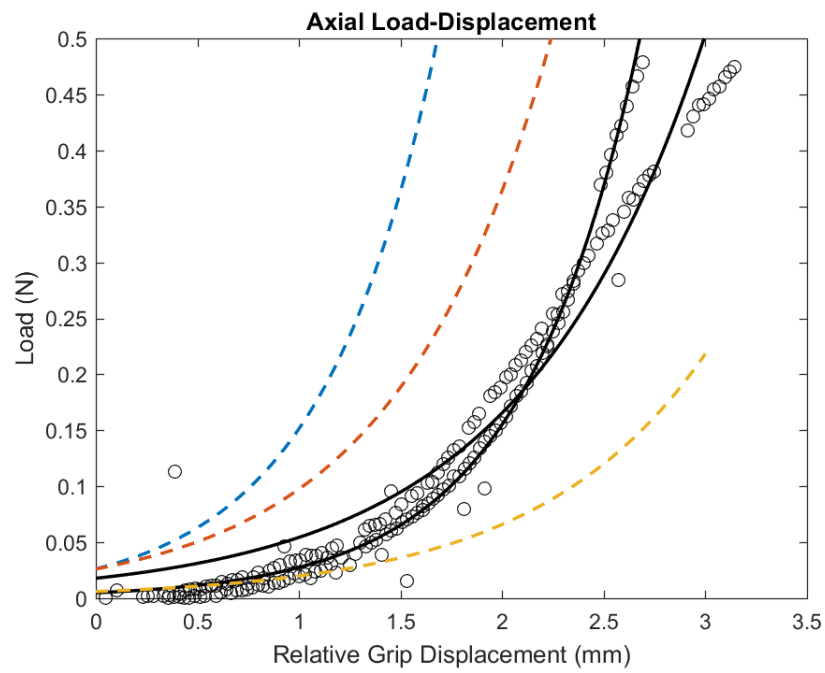
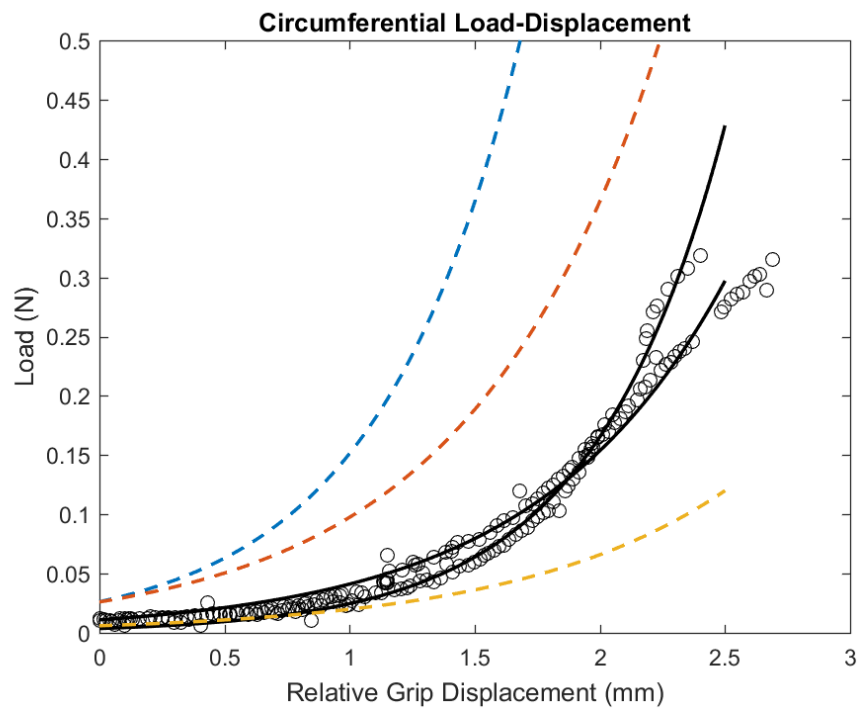
Sample 1 - Axial



Sample 1 – Circumferential



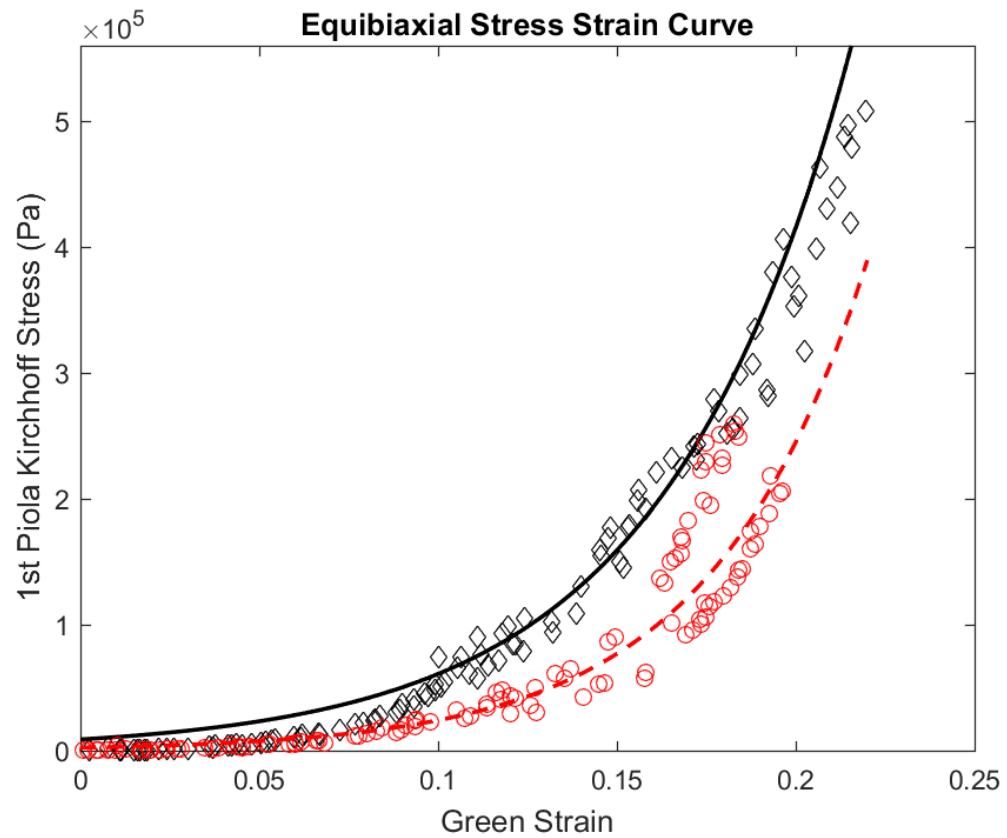
Sample 2 – Axial*Sample 2 – Circumferential*

Sample 3 – Axial*Sample 3 – Circumferential*

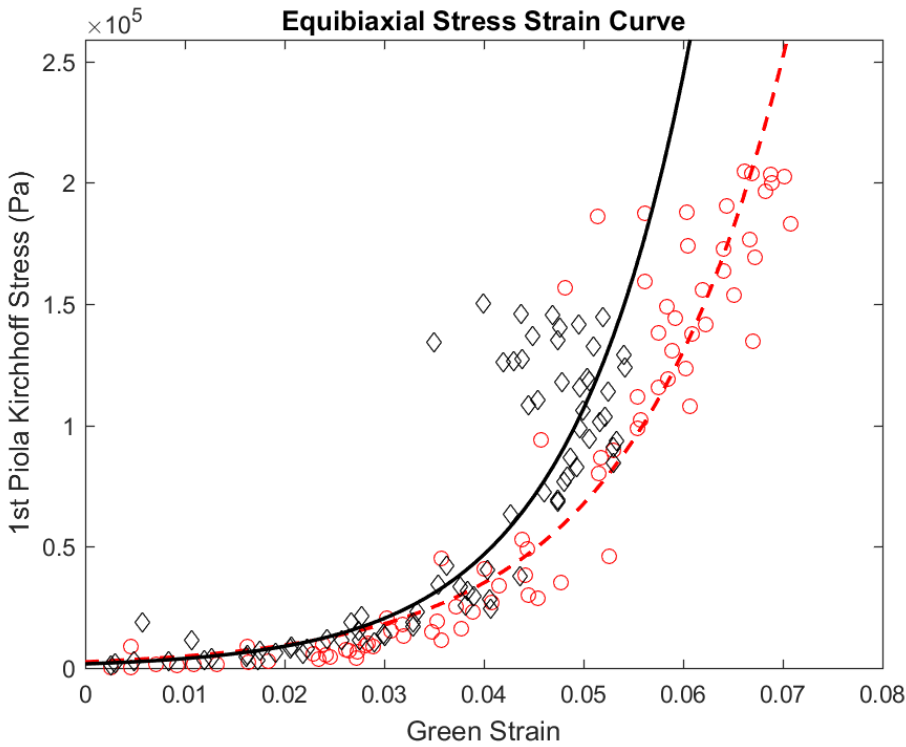
O.2 Stress Strain Curves

* Black line and symbols indicate the axial direction, while red line and symbols indicate the circumferential direction

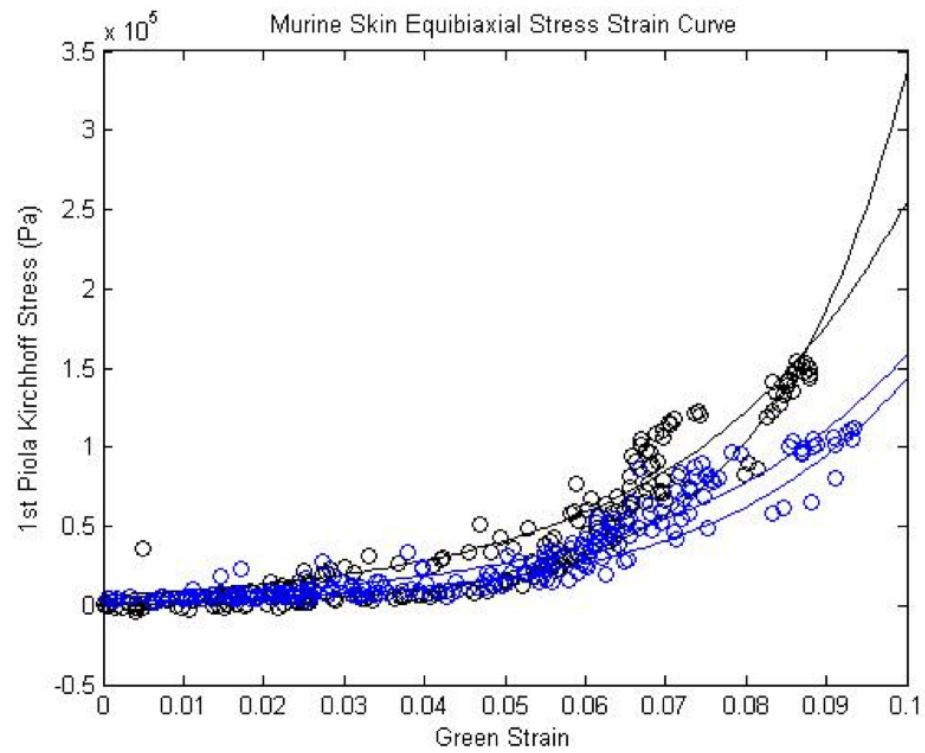
Sample 1



Sample 2



Sample 3 * circumferential direction is blue instead of red.



REFERENCES

1. Humphrey, Jay D. *Cardiovascular Solid Mechanics*. Springer Science & Business Media, 2013. Print.
2. Fung, Yuan-cheng. *Biomechanics: Mechanical Properties of Living Tissues*. Springer Science & Business Media, 2013. Print.
3. Humphrey, Jay D. "Review Paper: Continuum biomechanics of soft biological tissues." *Proceedings of the Royal Society of London A: Mathematical, Physical and Engineering Sciences*. Vol. 459. No. 2029. The Royal Society, 2003.
4. Nordin, Margareta, and Victor Hirsch Frankel, eds. *Basic biomechanics of the musculoskeletal system*. Lippincott Williams & Wilkins, 2001.
5. Humphrey, J. D., and K. R. Rajagopal. "A Constrained Mixture Model for Growth and Remodeling of Soft Tissues." *Mathematical Models and Methods in Applied Sciences* 12.3 (2002): 407–430. Web.
6. Ramachandra, Abhay B et al. "Computational Simulation of the Adaptive Capacity of Vein Grafts in Response to Increased Pressure." *Journal of biomechanical engineering* 137.3 (2015): 31009. Web.
7. Valentin, A., J.D. Humphrey, and G.A. Holzapfel. "A Multi-Layered Computational Model of Coupled Elastin Degradation, Vasoactive Dysfunction, and Collagenous Stiffening in Aortic Aging." *Annals of Biomedical Engineering* (2001): n. page. Web.
8. Wilson, J. S., S. Baek, and J. D. Humphrey. "Importance of Initial Aortic Properties on the Evolving Regional Anisotropy, Stiffness and Wall Thickness of Human Abdominal Aortic Aneurysms." *Journal of The Royal Society Interface* 9.74 (2012): 2047–2058. Web.
9. Beason, David P. et al. "Development and Evaluation of Multiple Tendon Injury Models in the Mouse." *Journal of Biomechanics* 45.8 (2012): 1550–1553. Web.
10. Dunkman, Andrew A. et al. "Decorin Expression Is Important for Age-Related Changes in Tendon Structure and Mechanical Properties." *Matrix Biology* 32.1 (2013): 3–13. Web.
11. Dunkman, Andrew A. et al. "The Injury Response of Aged Tendons in the Absence of Biglycan and Decorin." *Matrix Biology* 35 (2014): 232–238. Web.

12. Dunkman, Andrew A. et al. "The Tendon Injury Response Is Influenced by Decorin and Biglycan." *Annals of Biomedical Engineering* 42.3 (2014): 619–630. Web.
13. Sacks, Michael S. "Biaxial Mechanical Evaluation of Planar Biological Materials." *Journal of Elasticity* 61.1-3 (2000): 199-246. Web.
14. Rivlin, Ronald S., and D.W. Saunders. "Large Elastic Deformations of Isotropic Materials. VII. Experiments on the Deformation of Rubber." *Philosophical Transactions of the Royal Society of London A: Mathematical, Physical, and Engineering Sciences* (1951): 251–288. Print.
15. Treloar, Leslie R. G. "The Physics of Rubber Elasticity." Oxford University Press (1975): n. pag. Print.
16. Lanir, Y, and Y C Fung. "Two-Dimensional Mechanical Properties of Rabbit Skin: I Experimental System." *Journal of Biomechanics* 1974: 171–182. Print.
17. Lanir, Y, and Y C Fung. "Two-Dimensional Mechanical Properties of Rabbit Skin: II - Experimental Results." *Journal of Biomechanics* 1974: 171–182. Print.
18. Tong, Pin, and Yuang-Cheng Fung. "The Stress-Strain Relationship for the Skin." *Journal of Biomechanics* 9.10 (1976): 649-57. Print.
19. Vito, R P. "The Mechanical Properties of Soft Tissues - I: A Mechanical System for Bi-Axial Testing." *Journal of Biomechanics* 1980: 947–950. Print.
20. Khalsa, P S, a H Hoffman, and P Grigg. "Mechanical States Encoded by Stretch Sensitive Neurons in Feline Joint Capsule." *Journal of neurophysiology* 76.1 (1996): 175–87. Web.
21. Sacks, M S, and C J Chuong. "Orthotropic Mechanical Properties of Chemically Treated Bovine Pericardium." *Annals of biomedical engineering* 26.5 (1998): 892–902. Web.
22. Vande Geest, Jonathan P., Michael S. Sacks, and David A. Vorp. "The Effects of Aneurysm on the Biaxial Mechanical Behavior of Human Abdominal Aorta." *Journal of Biomechanics* 39.7 (2006): 1324–1334. Web.
23. Szczesny, Spencer E. et al. "Biaxial Tensile Testing and Constitutive Modeling of Human Supraspinatus Tendon." *Journal of Biomechanical Engineering* 134.2 (2012): 21004. Web.
24. Silverberg, Edwin, and J A Lubera. "Cancer Statistics, 1987." *CA: A Cancer Journal for Clinicians* 37.1 (1987): 2–19. Web.

25. Jelovsek, J., C. Miller, and M. Barber. "Pelvic Organ Prolapse." *Radiologic technology* 77 (2007): 389-400-403. Web.
26. Matthews, T. J. W. "Pathology of the Torn Rotator Cuff Tendon: REDUCTION IN POTENTIAL FOR REPAIR AS TEAR SIZE INCREASES." *Journal of Bone and Joint Surgery - British Volume* 88-B.4 (2006): 489-495. Web.
27. Brett, Allan W. et al. "Quantification of the Transverse Carpal Ligament Elastic Properties by Sex and Region." *Clinical Biomechanics* 29.6 (2014): 601-606. Web.
28. Duenwald, Sarah E., Ray Vanderby, and Roderic S. Lakes. "Stress Relaxation and Recovery in Tendon and Ligament: Experiment and Modeling." *Biorheology* 47.1 (2010): 1-14. Web.
29. Schatzmann, L, P Brunner, and H U Staubli. "Effect of Cyclic Preconditioning on the Tensile Properties of Human Quadriceps Tendons and Patellar Ligaments." *Knee Surg Sports Traumatol Arthrosc* 6 Suppl 1 (1998): S56--S61. Web.
30. Sverdlik, A, and Y Lanir. "Time-Dependent Mechanical Behavior of Sheep Digital Tendons, Including the Effects of Preconditioning." *J Biomech Eng* 124.1 (2002): 78-84. Web.
31. Magnusson, S. P. et al. "The Adaptability of Tendon to Loading Differs in Men and Women." *International Journal of Experimental Pathology* 88.4 (2007): 237-240. Web.
32. Finlay, B. "Dynamic Mechanical Testing of Human Skin 'in Vivo'." *Journal of Biomechanics* 3.May (1970): 557-68. Print.
33. Moore, Keith L., Anne M.R. Agur, and Arthur F. Dalley. *Essential Clinical Anatomy*. Lippincott Williams & Wilkins, 2015. Print.
34. Groves, Rachel B., et al. "An anisotropic, hyperelastic model for skin: experimental measurements, finite element modelling and identification of parameters for human and murine skin." *Journal of the mechanical behavior of biomedical materials* 18 (2013): 167-180.
35. Pereira, J.M., J.M. Mansour, and B.R. Davis. "Dynamic Measurement of the Viscoelastic Properties of Skin." *Journal of Biomechanics* 1991: 157-162. Web.
36. Munoz, M. J., et al. "An experimental study of the mouse skin behaviour: damage and inelastic aspects." *Journal of biomechanics* 41.1 (2008): 93-99.

37. Ma, J., and A. Jemal. "Breast Cancer Statistics." American Cancer Society – Breast Cancer Metastasis and Drug Resistance (2013): 47–64. Web.
38. Pashos, Nicholas C. et al. "Characterization of an Acellular Scaffold for a Tissue Engineering Approach to the Nipple-Areolar Complex Reconstruction." *Cells Tissues Organs* 70112 (2017): n. pag. Web.
39. Nicholson, Brandi T, Jennifer a Harvey, and Michael a Cohen. "Nipple-Areolar Complex: Normal Anatomy and Benign and Malignant Processes." *Radiographics* : a review publication of the Radiological Society of North America, Inc 29.2 (2009): 509–523. Web.
40. Siegel, Rebecca et al. "Cancer Treatment and Survivorship Statistics , 2012." *CA: a cancer journal for clinicians* 62 (2012): 220–241. Web.
41. Halvorson, Eric G. et al. "Three-Dimensional Nipple-Areola Tattooing." *Plastic and Reconstructive Surgery* 133.5 (2014): 1073–1075. Web.
42. Jordan, Sumanas W. et al. "An Algorithmic Approach for Selective Acellular Dermal Matrix Use in Immediate Two-Stage Breast Reconstruction." *Plastic and Reconstructive Surgery* 134.2 (2014): 178–188. Web.
43. Bai, Yuqiang et al. "Sequential Multimodal Microscopic Imaging and Biaxial Mechanical Testing of Living Multicomponent Tissue Constructs." *Annals of Biomedical Engineering* 42.9 (2014): 1791–1805. Web.
44. Abramowitch, Steven D. et al. "Tissue Mechanics, Animal Models, and Pelvic Organ Prolapse: A Review." *European Journal of Obstetrics Gynecology and Reproductive Biology* 144.SUPPL 1 (2009): 146–158. Web.
45. Bump, Richard C et al. "The Standardization of Terminology of Female Pelvic Organ Prolapse and Pelvic Floor Dysfunction." *American journal of obstetrics and gynecology* 175.1 (1996): 10–17. Web.
46. Heit, M et al. "Predicting Treatment Choice for Patients with Pelvic Organ Prolapse." *Obstetrics & Gynecology* 101.6 (2003): 1279–1284. Web.
47. Barber, Matthew D et al. "Sexual Function in Women with Urinary Incontinence and Pelvic Organ Prolapse." *Obstetrics & Gynecology* 99.2 (2002): 281–289. Web.
48. Weber, Anne M. et al. "Sexual Function in Women with Uterovaginal Prolapse and Urinary Incontinence." *Obstetrics and Gynecology* 1995: 483–487. Web.
49. Pizarro-Berdichevsky, Javier, Marisa M. Clifton, and Howard B. Goldman.

- “Evaluation and Management of Pelvic Organ Prolapse in Elderly Women.” *Clinics in Geriatric Medicine* 31.4 (2015): 507–521. Web.
50. Hendrix, Susan L. et al. “Pelvic Organ Prolapse in the Women’s Health Initiative: Gravity and Gravidity.” *American Journal of Obstetrics and Gynecology* 186.6 (2002): 1160–1166. Web.
 51. Olsen, Ambre L. et al. “Epidemiology of Surgically Managed Pelvic Organ Prolapse and Urinary Incontinence.” *Obstetrics and Gynecology* 1997: 501–506. Web.
 52. Kerkhof, Manon H. et al. “Changes in Tissue Composition of the Vaginal Wall of Premenopausal Women with Prolapse.” *American Journal of Obstetrics and Gynecology* 210.2 (2014): 168.e1-168.e9. Web.
 53. Schaffer, Joseph I, Clifford Y Wai, and Muriel K Boreham. “Etiology of Pelvic Organ Prolapse.” *Clinical obstetrics and gynecology* 48.3 (2005): 639–647. Web.
 54. Read, Charles P. et al. “Cervical Remodeling during Pregnancy and Parturition: Molecular Characterization of the Softening Phase in Mice.” *Reproduction* 134.2 (2007): 327–340. Web.
 55. Swift, Steven et al. “Pelvic Organ Support Study (POSST): The Distribution, Clinical Definition, and Epidemiologic Condition of Pelvic Organ Support Defects.” *American Journal of Obstetrics and Gynecology* 192.3 (2005): 795–806. Web.
 56. Moalli, Pamela A et al. “Remodeling of Vaginal Connective Tissue in Patients with Prolapse.” *Current opinion in obstetrics & gynecology* 106.5 (2006): 953–96. Web.
 57. Chen, B. H. et al. “Collagen Metabolism and Turnover in Women with Stress Urinary Incontinence and Pelvic Prolapse.” *International Urogynecology Journal and Pelvic Floor Dysfunction* 13.2 (2002): 80–87. Web.
 58. Phillips, Christian H. et al. “Collagen Metabolism in the Uterosacral Ligaments and Vaginal Skin of Women with Uterine Prolapse.” *BJOG: An International Journal of Obstetrics and Gynecology* 113.1 (2006): 39–46. Web.
 59. Goh, J T W. “Original Article Biomechanical Properties of Prolapsed Vaginal Tissue in Pre- and Postmenopausal Women.” *International Urogynecology Journal* (2002): 76–79. Print.
 60. Cosson, Michel et al. “A Biomechanical Study of the Strength of Vaginal Tissues: Results on 16 Post-Menopausal Patients Presenting with Genital Prolapse.” *European Journal of Obstetrics Gynecology and Reproductive Biology* 112.2

- (2004): 201–205. Web.
61. Lei, Lingling, Yanfeng Song, and RiQi Chen. “Biomechanical Properties of Prolapsed Vaginal Tissue in Pre- and Postmenopausal Women.” *International Urogynecology Journal and Pelvic Floor Dysfunction* 18.6 (2007): 603–607. Web.
 62. Rahn, David D. et al. “Biomechanical Properties of the Vaginal Wall: Effect of Pregnancy, Elastic Fiber Deficiency, and Pelvic Organ Prolapse.” *American Journal of Obstetrics and Gynecology* 198.5 (2008): n. pag. Web.
 63. Feola, Andrew et al. “Impact of Pregnancy and Vaginal Delivery on the Passive and Active Mechanics of the Rat Vagina.” *Annals of Biomedical Engineering* 39.1 (2011): 549–558. Web.
 64. Lowder, J. et al. “Biomechanical Adaptations of the Rat Vagina in Pregnancy to Accommodate Delivery.” *Obstetrics & Gynecology* 109.1 (2007): 128–135. Web.
 65. Alperin, Marianna et al. “Pregnancy-and Delivery-Induced Biomechanical Changes in Rat Vagina Persist Postpartum.” *International Urogynecology Journal and Pelvic Floor Dysfunction* 21.9 (2010): 1169–1174. Web.
 66. Couri, B. M., Lenis, A. T., Borazjani, A., Paraiso, M. F., and Damaser, M. S., 2012, "Animal models of female pelvic organ prolapse: lessons learned," *Expert Rev Obstet Gynecol*, 7(3), pp. 249-260.
 67. Moalli, P. A. et al. “Impact of Menopause on Collagen Subtypes in the Arcus Tendinous Fasciae Pelvis.” *American Journal of Obstetrics and Gynecology* 190.3 (2004): 620–627. Web.
 68. Mizuno, Tomohiro et al. “Overexpression of Elastin Fragments in Infarcted Myocardium Attenuates Scar Expansion and Heart Dysfunction.” *American journal of physiology. Heart and circulatory physiology* 288.6 (2005): H2819-27. Web.
 69. Wen, Y. et al. “Differences in mRNA and Protein Expression of Small Proteoglycans in Vaginal Wall Tissue from Women with and without Stress Urinary Incontinence.” *Human Reproduction* (2007): 1718–1724. Print.
 70. Tan, Ting et al. “Micro-Structural and Biaxial Creep Properties of the Swine Uterosacral–Cardinal Ligament Complex.” *Annals of Biomedical Engineering* 44.11 (2016): 3225–3237. Web.
 71. Tan, Ting et al. “Histo-Mechanical Properties of the Swine Cardinal and Uterosacral

- Ligaments.” *Journal of the Mechanical Behavior of Biomedical Materials* 42 (2015): 129–137. Web.
72. Doillon, C J et al. “Collagen Fiber Formation in Repair Tissue: Development of Strength and Toughness.” *Collagen and related research* 5.6 (1985): 481–492. Web.
 73. Niyibizi, Christopher, and David R. Eyre. “Structural Characteristics of Cross Linking Sites in Type V Collagen of Bone: Chain Specificities and Heterotypic Links to Type I Collagen.” *European Journal of Biochemistry* 224.3 (1994): 943–950. Web.
 74. Subak, L et al. “Cost of Pelvic Organ Prolapse Surgery in the United States.” *Obstet. Gynecol.* 98.4 (2001): 646–651. Web.
 75. Luber, Karl M., Sally Boero, and Jennifer Y. Choe. “The Demographics of Pelvic Floor Disorders: Current Observations and Future Projections.” *American Journal of Obstetrics and Gynecology* 184.7 (2001): 1496–1503. Web.
 76. Weber, Anne M, and Holly E Richter. “Pelvic Organ Prolapse.” *Obstetrics and gynecology* 106.3 (2005): 615–34. Web.
 77. DeLancey, John O L. “The Hidden Epidemic of Pelvic Floor Dysfunction: Achievable Goals for Improved Prevention and Treatment.” *American Journal of Obstetrics and Gynecology* 192.5 SPEC. ISS. (2005): 1488–1495. Web.
 78. Becker, Winston R, and Raffaella De Vita. “Biaxial Mechanical Properties of Swine Uterosacral and Cardinal Ligaments.” *Biomechanics and Modeling in Mechanobiology* (2015): 549–560. Web.
 79. de Landsheere, Laurent et al. “Elastin Density: Link between Histological and Biomechanical Properties of Vaginal Tissue in Women with Pelvic Organ Prolapse?” *International Urogynecology Journal and Pelvic Floor Dysfunction* 27.4 (2016): 629–635. Web.
 80. Peña, Estefania et al. “Experimental Study and Constitutive Modeling of the Viscoelastic Mechanical Properties of the Human Prolapsed Vaginal Tissue.” *Biomechanics and Modeling in Mechanobiology* 9.1 (2010): 35–44. Web.
 81. Peña, E. et al. “Mechanical Characterization of the Softening Behavior of Human Vaginal Tissue.” *Journal of the Mechanical Behavior of Biomedical Materials* 4.3 (2011): 275–283. Web.
 82. Martins, P et al. “Prediction of Nonlinear Elastic Behaviour of Vaginal Tissue:

- Experimental Results and Model Formulation.” *Computer methods in biomechanics and biomedical engineering* 13.3 (2010): 327–337. Web.
83. Budatha, Madhusudhan et al. “Dysregulation of Protease and Protease Inhibitors in a Mouse Model of Human Pelvic Organ Prolapse.” *PLoS ONE* 8.2 (2013): n. pag. Web.
 84. Alperin, Marianna et al. “LOXL1 Deficiency Negatively Impacts the Biomechanical Properties of the Mouse Vagina and Supportive Tissues.” *International Urogynecology Journal and Pelvic Floor Dysfunction* 19.7 (2008): 977–986. Web.
 85. Drewes, Peter G. et al. “Pelvic Organ Prolapse in Fibulin-5 Knockout Mice.” *The American Journal of Pathology* 170.2 (2007): 578–589. Web.
 86. Couri, Bruna M. et al. “Pathophysiologic Changes in Loxl-1 Knockout Mouse With Pelvic Floor Dysfunction Induce a Compensatory and Aberrant Elastin Regenerative Response By Vaginal Smooth Muscle Cells.” *The Journal of Urology* 189.4 (2013): e50. Web.
 87. Morris, V., Conway, C., and Miller, K., 2016, "Determining the Effect of Elastin Digestion on the Regional Biaxial Mechanical Properties of the Murine Cervix," Summer Biomechanics, Bioengineering, and Biotransport Conference (SB3C2016).
 88. Robison, K., Bivona, D., and Miller, K., 2016, "Effect of Elastin Digestion on the Biaxial Mechanical Response of the Murine Vagina.," Summer Biomechanics, Bioengineering and Biotransport Conference (SB3C2016).
 89. Collins, M. J. et al. “Acute Mechanical Effects of Elastase on the Infrarenal Mouse Aorta: Implications for Models of Aneurysms.” *Journal of Biomechanics* 45.4 (2012): 660–665. Web.
 90. Henninger, Heath B. et al. “Effect of Elastin Digestion on the Quasi-Static Tensile Response of Medial Collateral Ligament.” *Journal of Orthopaedic Research* 31.8 (2013): 1226–1233. Web.
 91. Ferruzzi, Jacopo, et al. "Mechanical assessment of elastin integrity in fibrillin-1 deficient carotid arteries: implications for Marfan syndrome." *Cardiovascular research* 92.2 (2011): 287-295.
 92. Udelsman, Brooks V. et al. “Characterization of Evolving Biomechanical Properties of Tissue Engineered Vascular Grafts in the Arterial Circulation.” *Journal of Biomechanics* 47.9 (2014): 2070–2079. Web.

93. Bersi, M. R., et al. "Disparate changes in the mechanical properties of murine carotid arteries and aorta in response to chronic infusion of angiotensin-II." *International journal of advances in engineering sciences and applied mathematics* 4.4 (2012): 228-240.
94. Liu, et al. "GPER activation ameliorates aortic remodeling induced by salt-sensitive hypertension." *American Journal of Physiology-Heart and Circulatory Physiology* 310.8 (2016): H953-H961.
95. Miller, Kristin S., Brianne K. Connizzo, and Louis J. Soslowsky. "Collagen Fiber Re Alignment in a Neonatal Developmental Mouse Supraspinatus Tendon Model." *Annals of Biomedical Engineering* 40.5 (2012): 1102–1110. Web.
96. Miller, Kristin S. et al. "Characterizing Local Collagen Fiber Re-Alignment and Crimp Behavior throughout Mechanical Testing in a Mature Mouse Supraspinatus Tendon Model." *Journal of Biomechanics* 45.12 (2012): 2061–2065. Web.
97. Downing, Keith T. et al. "The Role of Mode of Delivery on Elastic Fiber Architecture and Vaginal Vault Elasticity: A Rodent Model Study." *Journal of the Mechanical Behavior of Biomedical Materials* 29 (2014): 190–198. Web.
98. Moster, Dag, Rolv Terje Lie, and Trond Markestad. "Long-Term Medical and Social Consequences of Preterm Birth." *The New England journal of medicine* 359.3 (2008): 262–73. Web.
99. Petrou, Stavros, Oya Eddama, and Lindsay Mangham. "A Structured Review of the Recent Literature on the Economic Consequences of Preterm Birth." *Archives of disease in childhood. Fetal and neonatal edition* 96.3 (2011): F225-32. Web.
100. Platt, M.J. "Outcomes in Preterm Infants." *Public Health* (2014): 399–403. Print.
101. Rich-Edwards, Janet W. et al. "Pregnancy Characteristics and Women's Future Cardiovascular Health: An Underused Opportunity to Improve Women's Health?" *Epidemiologic Reviews* 36.1 (2014): 57–70. Web.
102. Georgiou, Harry M. et al. "Predicting Preterm Labour: Current Status and Future Prospects." 2015 (2015): n. pag. Web.
103. Romero, Roberto, Sudhansu K Dey, and Susan J Fisher. "Preterm Labor: One Syndrome, Many Causes." 345.6198 (2014): n. pag. Web.
104. Gotsch, F. et al. "The Preterm Parturition Syndrome and Its Implications for Understanding the Biology, Risk Assessment, Diagnosis, Treatment, and Prevention of Preterm Birth." *Journal of Maternal-Fetal and Neonatal Medicine* 22 (2009): 5–23. Print.

105. Alfredson, Håkan. "Chronic Midportion Achilles Tendinopathy: An Update on Research and Treatment." *Clinics in Sports Medicine* 22.4 (2003): 727–741. Web.
106. Fredberg, U., and K. Stengaard-Pedersen. "Chronic Tendinopathy Tissue Pathology, Pain Mechanisms, and Etiology with a Special Focus on Inflammation: Review." *Scandinavian Journal of Medicine and Science in Sports* 18.1 (2008): 3–15. Web.
107. Carroll, C C et al. "Influence of Aging on the in Vivo Properties of Human Patellar Tendon." *Journal of applied physiology* 105.6 (2008): 1907–15. Web.
108. Dressler, M. R., D. L. Butler, and G. P. Boivin. "Age-Related Changes in the Biomechanics of Healing Patellar Tendon." *Journal of Biomechanics* 39.12 (2006): 2205–2212. Web.
109. Netter, Frank Henry, and Sharon Colacino. *Atlas of human anatomy*. Vol. 11. Summit, NJ: Ciba-Geigy, 1989.
110. Hast, M. W., A. Zuskov, and L. J. Soslowsky. "The role of animal models in tendon research." *Bone and Joint Research* 3.6 (2014): 193-202.
111. Pearson, S. J., and S.R. Hussain. "Regional-Specific Tendon Properties and Patellar Tendinopathy: A Wilder Understanding." *Sports Medicine* (2014): 1101–1112. Print.
112. Smith, R. K W et al. "The Influence of Ageing and Exercise on Tendon Growth and Degeneration - Hypotheses for the Initiation and Prevention of Strain-Induced Tendinopathies." *Comparative Biochemistry and Physiology - A Molecular and Integrative Physiology* 133.4 (2002): 1039–1050. Web.
113. Lin, Tony W. et al. "Tendon Healing in Interleukin-4 and Interleukin-6 Knockout Mice." *Journal of Biomechanics* 39.1 (2006): 61–69. Web.
114. Probst, A. Palmes, D., Freise, H. M. "A New Clamping Technique for Biomechanical Testing of Tendons in Small Animals." *Journal of Investigative Surgery* 13.6 (2000): 313–318. Web.
115. Lynch, H. A., W. Johannessen, J. P. Wu, A. Jawa, and D. M. Elliott, "Effect of fiber orientation and strain rate on the nonlinear uniaxial tensile material properties of tendon.(Author Abstract)," *Journal of Biomechanical Engineering*, vol. 125, p. 726, 2003.
116. Mienaltowski, Michael J. et al. "Injury Response of Geriatric Mouse Patellar Tendons: Aging Mouse Tendon Injury Response." *Journal of Orthopaedic Research* July (2016): 1256–1263. Web.

117. Stäubli, H U et al. "Mechanical Tensile Properties of the Quadriceps Tendon and Patellar Ligament in Young Adults." *The American journal of sports medicine* 27.1 (1999): 27–34. Print.
118. Dourte, Leann M et al. "Influence of Decorin on the Mechanical , Compositional , and Structural Properties of the Mouse Patellar Tendon." *Journal of Biomechanical Engineering* 134.March 2012 (2017): 1–8. Web.
119. Lin, Tony W. "Development and Utilization of a Transgenic Mouse Injury Model to Investigate the Role of Interleukin-4 and Interleukin-6 in Tendon Healing." University of Pennsylvania, 2004. Print.
120. McClung, J M et al. "Estrogen Status and Skeletal Muscle Recovery from Disuse Atrophy." *Journal of applied physiology* (Bethesda, Md. : 1985) 100.6 (2006): 2012–23. Web.
121. Miller, Benjamin F et al. "No Effect of Menstrual Cycle on Myofibrillar and Connective Tissue Protein Synthesis in Contracting Skeletal Muscle." *American journal of physiology. Endocrinology and metabolism* 290.1 (2006): E163–E168. Web.
122. Luo, Z P et al. "Mechanical Environment Associated with Rotator Cuff Tears." *Journal of shoulder and elbow surgery / American Shoulder and Elbow Surgeons ... [et al.]* 7.6 (1998): 616–620. Web.
123. Wakabayashi, Ikuko et al. "Mechanical Environment of the Supraspinatus Tendon: A Two-Dimensional Finite Element Model Analysis." *Journal of Shoulder and Elbow Surgery* 12.6 (2003): 612–617. Web.

BIOGRAPHY

Taylor McCrady is from Gilbert, Arizona, and started her studies in biomedical engineering at Tulane University as an undergraduate in August 2012. She completed her MS and BSE degrees concurrently through the biomedical engineering 5th Year Masters program. During her time at Tulane, she was an active member of the Biomechanics of Growth and Remodeling lab, a Maker Ninja in the MakerSpace, and a semi-finalist in Tulane's Inaugural Novel Tech Challenge. In her spare time, she likes to run and make frequent trips to Disneyland.